JETP Letters, Vol. 78, No. 9, 2003, pp. 523–527. Translated from Pis'ma v Zhurnal Éksperimental'noĭ i Teoreticheskoĭ Fiziki, Vol. 78, No. 9, 2003, pp. 1011–1015.

Interparticle Interference of Neutrons in Multiple Small-Angle Scattering by a Close-Packed Polydisperse System

Yu. G. Abov, F. S. Dzheparov*, N. O. Elyutin, D. V. L'vov, Yu. I. Smirnov, and A. N. Tyulyusov

Institute of Theoretical and Experimental Physics, ul. Bol'shaya Cheremushkinskaya 25, Moscow, 117218 Russia

** e-mail: dzheparov@itep.ru*

Received September 11, 2003

Small-angle multiple neutron scattering by a disordered polydisperse system with various concentrations of scattering centers is studied experimentally and theoretically. The experiments show that, for high concentrations (specific volume of scatterers ≥30%), interparticle interference of neutron waves plays a significant role and strongly affects the angular distribution of scattered neutrons. The experimental results are qualitatively explained within the framework of the theory allowing for pair correlations in the spatial distribution of scatterers. © *2003 MAIK "Nauka/Interperiodica".*

PACS numbers: 61.12.-q; 61.43.-j

1. INTRODUCTION

The method of small-angle scattering of penetrating radiation is used for studying superatomic objects such as structural and magnetic inhomogeneities in solids, colloid particles and suspensions, etc. [1, 2]. Large-scale inhomogeneities are actively investigated by the method of ultrasmall-angle neutron scattering [3–6], which is based on the use of a double-crystal spectrometer. The most reliable results are obtained for monodisperse systems. Unfortunately, such systems are found only in some biological objects [7], while solid samples are monodisperse only in exceptional cases.

One usually prefers to use single scattering in experiments on small-angle scattering. However, in the problems of nondestructive testing of modern materials, one has to use thick samples, where the multiple scattering order is high. The first attempts to describe multiple scattering were based on the diffusion approximation [8]. Considerable progress was achieved in [9, 10] by applying the well-known Moliére–Bethe theory [11, 12], which was initially developed for the scattering of charged particles, to materials science problems of neutron physics.

Analysis of results obtained in [13, 14] showed that interference between waves scattered by different grains (interparticle interference effect) must be taken into account in small-angle multiple neutron scattering (MSANS). This phenomenon is well known in single photon scattering after the classical works of Zernike, Prince, and Debye [1].

The grain correlation effect on MSANS has not been studied experimentally as yet. This work aims to fill this gap. In this work, the MSANS differential cross section in polydisperse samples was directly investigated as a function of the average distance between scattering centers. A double-crystal spectrometer was used in conditions where the neutron scattering order was $N_s = l/l_c \lesssim 10$, where l is the sample thickness and l_c is the mean free path. The experiments were carried out on aluminum powder calibrated against the grain size (as in [13]). To change distances between Al grains, the initial powder was mixed in various proportions with a powder of TiZr alloy having zero coherent neutron-scattering length.

Preliminary results of this work were reported in [15, 16]. The main result presented in [15] was that the measured angular distribution $I(\vartheta)$ of scattered neutrons narrows with an increase in the grain density n (number of grains per unit volume) at a constant N_s. This effect is not described by the standard theory [9–12]. It was qualitatively explained in [16], where the general positions of a MSANS theory were developed for moderately dense media with correlated grain distribution and calculations were carried out for monodisperse media. In this work, these investigations are continued and, in particular, the MSANS theory is developed for the polydisperse media.

2. THEORY

As in [16], we use the eikonal approximation, where the scattering amplitude of nonpolarized neutrons on a nonpolarized sample has the form

$$f(\mathbf{q}) = \frac{p_0}{2\pi i}\int d^2\rho[S(\boldsymbol{\rho})-1]\exp(-i\mathbf{q}\boldsymbol{\rho}),$$
$$S(\boldsymbol{\rho}) = \exp\left(-i\int\limits_{-\infty}^{\infty}\frac{dz}{V}U(\mathbf{r})\right), \quad \mathbf{r} = (\boldsymbol{\rho}, z), \tag{1}$$

where, $\mathbf{p}_0 = (0, 0, p_0)$ is the initial neutron momentum, v is the neutron velocity, ρ is the impact parameter, and $\mathbf{q}$ is the scattering momentum such that $\mathbf{qp}_0 = 0$ and $q \ll p_0$. The neutron optical potential $U(\mathbf{r})$ of the medium is set equal to U_0 and 0 inside and outside grain, respectively.

It is convenient to represent the normalized distribution of scattered neutrons in the form [16]

$$D(\mathbf{q}) = \int d^2\xi e^{i\mathbf{q}\xi} D(\boldsymbol{\xi}), \quad D(\boldsymbol{\xi}) = \frac{\Sigma(\boldsymbol{\xi})}{\Sigma_0}, \tag{2}$$

$$\Sigma(\boldsymbol{\xi}) = p_0^2 \int d^2\rho S(\boldsymbol{\rho} - \boldsymbol{\xi}/2) S^+(\boldsymbol{\rho} + \boldsymbol{\xi}/2) \tag{3}$$

$$\approx p_0^2 A_s \langle S(-\boldsymbol{\xi}/2) S^+(\boldsymbol{\xi}/2)\rangle, \tag{4}$$

where $\Sigma_0 = \Sigma(\boldsymbol{\xi} = 0)$, A_s is the geometric cross section of a sample, and averaging in Eq. (4) is carried out over the ensemble of grain configurations. Hereafter, we use the same symbol for function $D(\mathbf{q})$ and its Fourier transform $D(\boldsymbol{\xi})$ and distinguish them by the argument. When going from Eq. (3) to Eq. (4), we assumed that $D(\mathbf{q})$ is a self-averaged quantity and ignored boundary effects (in particular, neutrons scattered by the mean potential of the sample were identified with the nonscattered neutrons; within the same accuracy, the distribution $D(\mathbf{q})$ is equivalent to the distribution $|f(\mathbf{q})|^2$).

The angular distribution measured by a double-crystal spectrometer under typical conditions is represented as [3]

$$I(q) = \int_{-\infty}^{\infty} dk D_0(q-k) I_0(k) = \frac{1}{\pi}\int_0^{\infty} d\xi \cos(q\xi) D_0(\xi) I_0(\xi),$$
$$D_0(q_1) = \int_{-\infty}^{\infty} dq_2 D(q_1, q_2). \tag{5}$$

Here, it is assumed that $D(\mathbf{q}) = D(-\mathbf{q}) = D(q)$, and $I_0(k) = I_0(-k)$ and $I_0(\xi)$ are the normalized instrumental line and its Fourier transform, respectively. As usual, we assume that $D(\mathbf{q})$ and $I_0(k)$ are concentrated at small q and k, respectively, so that the integration limits for q and k are taken to be infinite.

The numerical experiment was divided in two steps: development of a realistic model for the sample used in the experiment and calculation of the angular distribution of MSANS intensity for this model.

At the first step, the distribution of grain parameters was introduced. We restricted ourselves to the hypothesis of spherical particles. Analysis of a histogram determined from a microphotograph showed that the distribution of grain radii in experimental samples can be satisfactorily approximated by the function

$$w(r) = \frac{3r^2}{R^3}\exp\left(-\left(\frac{r}{R}\right)^3\right) \tag{6}$$

with $R = 1.42(6)$. The grain density n is associated with the experimental filling factor

$$\eta = \frac{4\pi}{3}\langle r^3\rangle n = m_s/m_0, \tag{7}$$

which was equal to $\eta_{Al} = 0.61(1)$ for the bulk density of Al powder. Here, m_s is the powder mass, m_0 is the mass of the solid sample of the same volume, and averaging is over radius distribution (6).

In the experimentally important diffraction range $\nu = U_0 r/v \ll 1$, the mean free path l_c is determined as

$$\frac{1}{l_c} = n\langle\sigma_t\rangle = 2\pi n\langle r^2\nu^2\rangle$$
$$= 2\pi n(U_0/v)^2\langle r^4\rangle = \frac{3\eta}{2}\left(\frac{U_0}{\nu}\right)^2\frac{\langle r^4\rangle}{\langle r^3\rangle}. \tag{8}$$

When modeling, one hundred values were taken for r_j ($0.44 < r_j < 5.0$). They were obtained as averages on the $(0.01\,(j - 0.5), 0.01\,(j + 0.5))$ intervals of the y variable uniformly distributed on [0, 1] and defined by the relation $w(r)dr = dy$. Calculation by formula (8) with this set of radii yields the value $N_s = l/l_c = 9$ for the Al sample corresponding to Fig. 1. The volume of the model sample was chosen so as to ensure the required density of scatterers n and the realistic (for the accessible computational speed) number of grains $N_t \gtrsim 1000$. The grain centers $\mathbf{x}_j$ were taken at random uniformly in this volume. To calculate realistic configuration, the formal pair potential

$$\Phi(\mathbf{x}_1, r_1; \cdots; \mathbf{x}_{N_t}, r_{N_t}) = \frac{1}{2}\sum_{ij}\phi_{ij},$$
$$\phi_{ij} = \vartheta(r_{ij} < r_i + r_j)\frac{r_i + r_j}{r_{ij} + r_i + r_j}, \tag{9}$$

was ascribed to the system. Here, r_j is the radius of the jth grain, $r_{ij} = |\mathbf{x}_i - \mathbf{x}_j|$ is the distance between the ith and jth centers, and $\vartheta(s)$ is the Heaviside step function. The periodic continuation was used at the sample boundaries. Then the known iteration method (see, e.g., [17]) was used. In this method, the configuration obtained after random displacement of grains is treated as a new configuration if its potential energy does not exceed the energy of the initial configuration. Every configuration obtained in this process was considered as realistic if $\Phi(\mathbf{x}_1, r_1; \cdots; \mathbf{x}_{N_t}, r_{N_t}) = 0$ for it.

The main calculations were carried out for the diffraction region with the Born parameter $\langle\nu\rangle = 0.3$ and with $D(\xi) = (D_m(\xi))^{N_s/N_s^0}$. Here $D_m(\xi)$ represents $D(\xi)$ for the model sample; it was calculated by formulas (2)–(4), and averaging in Eq. (4) over ρ from Eq. (3) was within one sample and over the samples with different grain configurations but with the same scattering

multiplicity N_s^0. In compliance with the experiment, a Lorentzian line with the width $\omega_0 = 3.1''$ was used as the instrumental line (see below). The width of the calculated MSANS spectrum is shown in Fig. 1 (dark circles) as a function of dilution s related to the filling factor η by Eq. (10).

3. MEASUREMENT PROCEDURE

Experiments were carried out on a universal neutron diffractometer equipped with a double monochromator block [18] based on Ge single crystals cut along the (1, 1, 1) plane. The first crystal served as a mosaic neutron-beam former and the second was a perfect monochromator. The sample under study was placed on the beam path behind the double monochromator block and ahead of a Ge perfect crystal served as an analyzer and arranged parallel to the monochromator. Neutrons reflected from the analyzer were detected by the ^{3}He detector of total absorption.

In this variant, the diffractometer operates as a double-crystal spectrometer with the parallel orientation of perfect crystals. Such spectrometers allow measurements for scattering angles ranging from 10^{-3} to 10^{-6} rad [19].

Neutrons of higher-order reflections were suppressed to less than 1% of the main component by a special 100-mm-thick single-crystal quartz filter. The analyzer crystal was rotated with a step of 0.12″. The FWHM of the instrumental line was $\omega_0 = (3.1 \pm 0.1)''$. Aluminum and TiZr powders obtained by sputtering from a melt into an inert gas, as well as their mixtures, were used as samples. The geometric parameters of the Al and TiZr grain distribution were determined from microphotographs as described in Section 2. The characteristic sizes of TiZr and Al grains were close to each other. The filling factor for TiZr was $\eta_{TiZr} = 0.405(10)$, and TiZr powder consisted of grains partially stuck together.

The powder of TiZr solid solution had composition corresponding to zero amplitude of coherent scattering $b(\mathrm{TiZr}) = 0$ (68 at. % of Ti and 32 at. % of Zr) and was used as a diluent matrix for Al grains.

The powders were put into identical special universal cylindrical cassettes 12 mm in diameter. The thickness of their input and output windows was equal to 0.2 mm, and neutron scattering by the empty cassette was not observed. The axis of the sample was oriented along the neutron beam. To estimate b(TiZr), a search for the refraction contrast [20] at the edges of a cylinder-shaped TiZr sample was carried out. The sample of a diameter 10 mm, was situated between the monochromator and analyzer crystals and moved with 0.1-mm steps in a direction perpendicular to the beam axis with an aperture of 0.1 mm. The absence of jumps in counting rate when a sample crossed the beam showed that $b(\mathrm{TiZr}) = (0 \pm 0.03)b(\mathrm{Ti})$. However, one more control

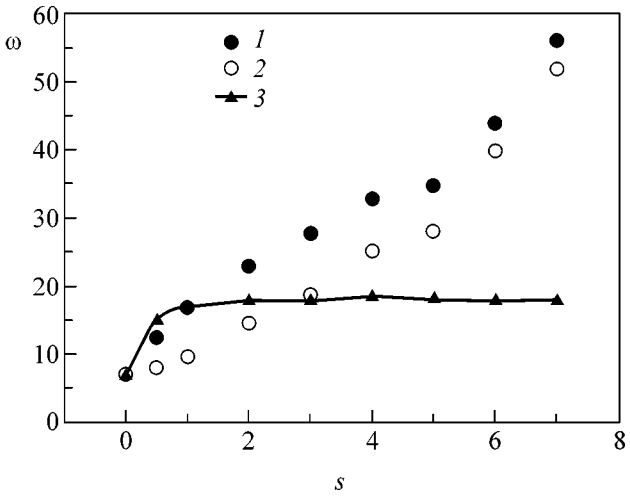

Fig. 1. FWHM ω (in angular seconds) of the MSANS curve vs. the ratio of Al and TiZr masses for $m_{Al} = 625$ mg. Closed and open circles are experimental data for the mixture of powders and layered arrangement, respectively; the line with triangles is calculated for the mixture.

experiment indicated that the spectrum $I(\vartheta)$ for pure TiZr with a mass of about 1000 mg was different from the instrumental line (Fig. 2, line *2*). This was likely caused by the chemical action on the grain surface, e.g., by oxidation, which was responsible for additional small-angle scattering. In particular, our TiZr powder samples were black, while the alloy from which they were produced was a silver-colored metal with a density of $\rho^0_{TiZr} = 5.1$ g/cm^3 natural for this composition. Moreover, with an increase in dilution s, the line wings raised and the peak became narrower, in qualitative agreement with scattering by the grain surfaces. The more complete clarification of the cause for this additional scattering requires separate investigation. In this work, to control the dilution effect, measurements were carried out for Al and TiZr powders both in a mixture and in their layered arrangement with the same mass ratios.

The counting rate (scattering curve) $I(\vartheta)$ for neutrons reflected from the analyzer crystal was measured as a function of the rotation angle ϑ of this analyzer about the axis perpendicular to the reflection plane. Figure 2 shows typical angular distributions. The dependence of line width ω on the bulk concentration of scattering centers was analyzed.

Samples were prepared by careful mixing of TiZr and Al powders in acetone followed by drying at room temperature for a day. A set of samples with varying mass ratio $s = m_{TiZr}/m_{Al} = 1, 2, \ldots, 7$ was prepared and, together with the sample of pure Al ($s = 0$) powder, allowed measurements in a wide dilution range $s = 0$–7 for the same mass of Al powder. The filling factor for diluted Al powder was determined by the expression

$$\eta = \eta_{Al}/(1 + s\rho_{Al}/\rho_{TiZr}) = \eta_{Al}/(1 + 0.792s), \quad (10)$$

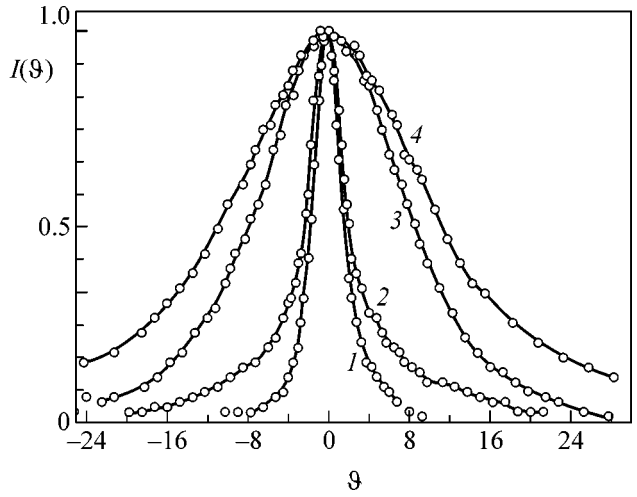

Fig. 2. Angular distributions $I(\vartheta)$ obtained using a double-crystal spectrometer: (*1*) without sample (instrumental line), (*2*) TiZr powder with mass m_{TiZr} = 1250 mg, (*3*) Al powder with mass m_{Al} = 1250 mg, and (*4*) mixture of Al and TiZr powders with masses $m_{Al} = m_{TiZr}$ = 1250 mg. Lines are normalized to unity at maximum.

and the volume fraction varied in the range η = 0.093–0.61.

4. RESULTS AND DISCUSSION

The possible interparticle interference effect on MSANS by Al powders was reported in [13], where the grain sizes obtained from the MSANS data were systematically larger than the sizes observed in microphotographs. It is natural to assume that this discrepancy is caused by the fact that the theoretical model, where scattering events for different grains are considered independent, is inconsistent with a real object, i.e., with grains in the bulk state (without additional compression) with a rather large density ρ_{Al} = 1.65(3) g/cm^3. The density of metallic aluminum is ρ_{Al}^{met} = 2.70 g/cm^3. Since these densities are close to each other, the grain distribution in such a powder should be similar to the distribution in close-packed systems (e.g., liquids and their mixtures), so that neutron scattering by different grains is not independent in this case. Therefore, the interparticle interference can likely manifest itself in the experiment.

For the *s*-fold dilution of Al powder with the TiZr powder, the filling factor decreases according to Eq. (10), and the width of the scattering spectrum increases (Fig. 1). In particular, for s = 1, the relative increase in the mixture volume is ≈0.8, the volume-filling factor for the Al grains decreases from $\eta \approx 0.61$ to $\eta \approx 0.34$, and the average distance between Al grains increases by only 22%. According to the theoretical calculation, the line width ω in this case increases almost threefold and becomes close to $\omega(s = \infty)$, in agreement with the experiment.

Neutron distribution (5) over the scattering momentum can conveniently be represented in the form

$$D_0(q) = F_s\delta(q) + F_r(q), \quad I(q) = F_sI_0(q) + I_r(q),$$
$$I_r(q) = \int_{-\infty}^{\infty} dkF_r(q-k)I_0(k). \tag{11}$$

The weight F_s of singular partion (fraction of unscattered neutrons) and the regular term $F_r(q)$ both depend on the degree of dilution s. In the general case, the function $F_r(q)$ can have several maxima (as, e.g., in single scattering). However, if the width of the instrumental line is comparable with the characteristic size of this structure, convolution (11) considerably smooths it. In this case, the width of the function $I_r(q)$ depends only slightly on s, whereas $F_s(s) = \exp(-\kappa(s)l/l_c)$, where l_c is the mean free path in the absence of correlations and the function $\kappa(s)$ changes by a factor of more than two with respect to $\kappa(s = \infty) = 1$ [16], resulting in a strong (exponential) dependence $F_s(s)$ for large $N_s = l/l_c$. As a result, the spectral width ω depends strongly on s in the region of parameters where $F_s/\omega_0 \sim I_r(q = 0)$. A more detailed investigation of this problem will be reported elsewhere.

5. CONCLUSIONS

The theoretical and experimental investigation of MSANS carried out in this work for filling factors $\eta \geq$ 9% and scattering orders $N \sim$ 5–10 has revealed the interparticle interference effect. It was shown that the interparticle interference has a sizable effect on the MSANS line in the range $\eta \sim$ 30–60% and changes its width by a factor of two to three. Thus, the Moliére–Bethe theory strongly overestimates scatterer sizes and, strictly speaking, does not apply under our conditions.

Theoretical results of this work show that the MSANS spectra for dense polydisperse samples can be simulated numerically. This opens up a way for wide application of microscopic calculations in solving the corresponding problems of materials science.

N.O.E. and Yu.I.S. are grateful to S.V. Maleev and B.P. Toperverg for stimulating discussions and moral support and to A.O. Éĭdlin and S.K. Matveev for assistance in carrying out experiments and processing results. This work was supported by the Ministry of Education of the Russian Federation (project no. T02-07.3-1375), by the Council of the President of the Russian Federation for Support of Young Russian Scientists and Leading Scientific Schools (project nos. NSh-1907.2003.2 and MK-2253-2003-02), and by the Russian Foundation for Basic Research (project nos. 00-02-17837 and 03-02-17126).

REFERENCES

1. D. I. Svergun and L. A. Feĭgin, *X-ray and Neutron Small-Angle Scattering* (Nauka, Moscow, 1986).
2. H. Glattli, Physica B (Amsterdam) **297**, 273 (2001).
3. Yu. G. Abov, D. S. Denisov, F. S. Dzheparov, *et al.*, Zh. Éksp. Teor. Fiz. **114**, 2194 (1998) [JETP **87**, 1195 (1998)].
4. A. P. Radlinski, E. Z. Radlinska, M. Agamalian, *et al.*, Phys. Rev. Lett. **82**, 3078 (1999).
5. H. Takeshita, T. Kanaya, K. Nishida, and K. Kaji, Phys. Rev. E **61**, 2125 (2000).
6. M. Hainbuchner, M. Baron, F. Lo Celso, *et al.*, Physica A (Amsterdam) **304**, 220 (2002).
7. Yu. M. Ostanevich and I. N. Serdyuk, Usp. Fiz. Nauk **137**, 85 (1982) [Sov. Phys. Usp. **25**, 323 (1982)].
8. D. L. Dexter and W. W. Beeman, Phys. Rev. **76**, 1782 (1949).
9. S. V. Maleev and B. P. Toperverg, Zh. Éksp. Teor. Fiz. **78**, 315 (1980) [Sov. Phys. JETP **51**, 158 (1980)].
10. J. Schelten and W. Schmatz, J. Appl. Crystallogr. **13**, 385 (1980).
11. G. Moliere, Z. Naturforsch. A **3**, 78 (1948).
12. G. Bethe, Phys. Rev. **89**, 1256 (1953).
13. Yu. I. Smirnov, A. O. Pekshev, A. O. Éĭdlin, *et al.*, Fiz. Tverd. Tela (Leningrad) **33**, 2273 (1991) [Sov. Phys. Solid State **33**, 1281 (1991)].
14. Yu. G. Abov, Yu. I. Smirnov, D. S. Denisov, *et al.*, Fiz. Tverd. Tela (St. Petersburg) **34**, 1408 (1992) [Sov. Phys. Solid State **34**, 748 (1992)].
15. Yu. G. Abov, Yu. I. Smirnov, D. S. Denisov, *et al.*, in *Proceedings of National Conference on the Use of X-rays, Synchrotron Radiation, Neutrons and Electrons to Study Materials* (JINR, Dubna, 1997), Vol. 2, p. 115.
16. F. S. Dzheparov and D. V. L'vov, Pis'ma Zh. Éksp. Teor. Fiz. **72**, 518 (2000) [JETP Lett. **72**, 360 (2000)].
17. R. Balescu, *Equilibrium and Non-Equilibrium Statistical Mechanics* (Wiley, New York, 1975; Mir, Moscow, 1978).
18. Yu. G. Abov, N. O. Elyutin, D. S. Denisov, *et al.*, Prib. Tekh. Éksp., No. 6, 67 (1994).
19. Yu. G. Abov, N. O. Elyutin, and A. N. Tyulyusov, Yad. Fiz. **65**, 1989 (2002) [Phys. At. Nucl. **65**, 1933 (2002)].
20. K. M. Podurets, V. A. Somenkov, and S. Sh. Shil'shteĭn, Zh. Tekh. Fiz. **59** (6), 115 (1989) [Sov. Phys. Tech. Phys. **34**, 654 (1989)].

Translated by R. Tyapaev

JETP Letters, Vol. 78, No. 9, 2003, pp. 528–532. From Pis'ma v Zhurnal Éksperimental'noĭ i Teoreticheskoĭ Fiziki, Vol. 78, No. 9, 2003, pp. 1016–1020.

New Method of Studying Slow Strange Meson Properties in Nuclear Matter¶

Yu. T. Kiselev* and V. A. Sheinkman

Institute of Theoretical and Experimental Physics, Moscow, 117218 Russia

**e-mail: yurikis@itep.ru*

Received September 16, 2003

We suggest a new experimental method to explore the properties of slow strange mesons at normal nuclear matter density. We show that the K^+ and K^- mesons with extremely small momenta relative to the surrounding medium rest frame can be produced in nucleus–nucleon collisions, and their production cross-sections are experimentally measurable. Experiments on the study of the momentum dependence of meson–nuclear potentials are discussed. © *2003 MAIK "Nauka/Interperiodica".*

PACS numbers: 21.65.+f; 14.40.Aq; 25.40.-h

The question about the properties of mesons in baryon matter has attracted much attention during recent years [1]. In particular, the investigation of strange mesons is of special interest as it is related to a partial restoration of chiral symmetry [2] and the possible existence of an antikaon condensed phase in the dense interior of neutron stars [3]. According to theoretical studies based on various approaches such as effective chiral Lagrangians [4] and mean-field models [5], the in-medium antikaon mass should be substantially reduced while the kaon mass is expected to be slightly enhanced. This has triggered a considerable interest in the study of K^- meson production in heavy-ion collisions. The dropping of the K^- mass in nuclear matter has a strong impact on the antikaon yield, especially in the subthreshold reactions due to the in-medium shift of the elementary production threshold to lower energies. An enhanced antikaon to kaon ratio in Ni + Ni collisions in the subthreshold energy regime has been observed at GSI [6, 7] and was attributed to the attractive antikaon potential of –(100–120) MeV at nuclear saturation density [8]. A strong attractive optical potential of about –(180–200) MeV at normal nuclear density for the K^- has been extracted from experimental data on kaonic atoms [9]. The substantial difference between the antikaon potentials mentioned above, i.e., their change in the mass, can be understood if the potential is momentum dependent. Indeed, the experiments with kaonic atoms deal with the K^- mesons of zero momentum relative to the nuclear matter rest frame while heavy-ion collisions at GSI probe the antikaons at momenta of more than 300 MeV/c (c is the velocity of light) with respect to the baryonic fireball [6]. The results of the calculations performed in the frame of different models [10–14] show that the influence of an antikaon potential on the subthreshold production of K^- mesons increases with a lowering of their momenta relative to the surrounding medium. It is therefore desirable to obtain information about the K^- and K^+ potentials at a momentum less than 300 MeV/c. In-medium modification effects are expected to be the most pronounced in nucleus–nucleus interactions in which high density and/or temperature are accessible. However, due to a complex dynamic involved the interpretation of heavy-ion experiments are, at present, far from unambiguous. Therefore, it is certainly useful to explore such effects under less extreme but much better controlled conditions at the normal nuclear density in proton–nucleus collisions. However, slow kaons and especially antikaons are hard to investigate experimentally in pA reactions mostly due to their strong decay and small production cross sections vanishing at zero meson momentum.

We discuss an alternative method of such research. The properties of mesons with extremely small momenta with respect to the nuclear matter rest frame can be explored in the inverse kinematics, i.e., in nucleus–nucleon collisions. As follows from the Lorentz transformation, slow particles in a projectile nucleus system appear to be fast in the laboratory, i.e., in the target-nucleon frame of reference. The meson, which is at rest inside the incident nucleus, has the same laboratory velocity as surrounding nucleons. Using inverse kinematics makes it possible to investigate particle production in new kinematic range, including zero momentum relative to the nuclear matter rest frame, which is not accessible in pA reactions. In contrast to heavy-ion collisions, the determination of the meson momenta relative to the nuclear environment in Ap reactions is model-independent.

The suggested method provides important advantages for experimental measurements in the low-

¶ This article was submitted by the authors in English.

momentum range. Large Lorentz boost with respect to the laboratory results in upward shifts of the K^+ and K^- momenta. As a consequence, their decay losses significantly decrease and the mesons become convenient for detection. Since the invariant cross sections are the same in both systems, experimentally observed differential cross sections in inverse and direct kinematics are related as

$$(d^2\sigma/dpd\Omega)^{Ap} = (p^2/E)^{Ap}(E/p^2)^{pA}(d^2\sigma/dpd\Omega)^{pA}, \quad (1)$$

where p and E stand for kaon (antikaon) momentum and energy while upper indices denote the type of reaction. For the production of mesons with low momentum relative to the nuclear matter rest frame, the cross section $(d^2\sigma/dpd\Omega)^{Ap}$ considerably exceeds $(d^2\sigma/dpd\Omega)^{pA}$ because the factor $(E/p^2)^{pA}$ grows rapidly with a lowering of meson momentum, while the factor $(p^2/E)^{Ap}$ changes rather smoothly.

In the present letter, we shall consider several applications of the suggested method.

1. Study of the in-medium kaon potential. Let us consider K^+ meson production in the inverse kinematics by an ion beam on a hydrogen target. Our estimate of the cross section for kaon production in Ap collisions is based on data from pA reactions as well as the calculations performed in the framework of the simple folding model [15], disregarding any potentials. Within this approach, inclusive K^+ production in proton–nucleus collisions at near-threshold and subthreshold energies is analyzed with respect to the one-step ($pN \longrightarrow K^+YN$, $Y = \Lambda, \Sigma$) and two-step ($pN_1 \longrightarrow \pi NN$, $\pi N_2 \longrightarrow K^+Y$) incoherent processes. The invariant cross sections for both forward and backward kaon production in pA collisions at initial proton energies 2 GeV were found, taking into account both reaction channels, and then transformed into noninvariant double differential form. In Fig. 1, the calculated double differential cross section for forward K^+ meson production on a carbon target (dashed curve) is compared to that measured in the angular range 0°–10° at the same initial proton energy [16]. Experimental data are seen to be reasonably well reproduced. Simple kinematical calculation shows that, at the beam energy 2 AGeV (A is the atomic mass number), the kaons produced inside a projectile nucleus with momenta from zero to 0.3 GeV/c in the backward hemisphere relative to the beam direction appear in the laboratory within the longitudinal and transverse momentum ranges $0.78 \le P_l \le 1.47$ GeV/c and $0 \le P_t \le 0.3$ GeV/c, respectively. The K^+ mesons emitted in the forward hemisphere with momenta up to 0.3 GeV/c will be observed in the laboratory momentum range $1.47 \le P_l \le 2.66$ GeV/c and in the same interval of P_t. Laboratory momenta (in GeV/c) of the K^+ mesons from carbon–proton collisions corresponding to the momenta of kaons produced in forward and backward directions in p^{12}C reaction are plotted on the upper axis. The solid curve in the figure depicts the double differential cross section for K^+ production in the inverse kinematics obtained from the calculated cross section (dashed curve) by using Eq. (1). The left-hand part of the figure is related to an experimentally unexplored range of backward kaon production in proton–nucleus collisions. A comparison of the data [16] presented in Fig. 1 with the predicted cross section shows that it is definitely acceptable for measurements, and significantly exceeds that of traditional kinematics in the most interesting range of low K^+ momenta relative to surrounding nuclear matter. Furthermore, an upward shift of a kaon momentum in Ap collisions results in a sizable decrease of K^+ decay losses. In contrast to pA reactions, large values of the cross section and its smooth behavior provide favorable experimental conditions for the investigation of in-medium effects in the inverse kinematics, in spite of the fact that the intensity of the ion beams is usually smaller than that of the proton ones. The influence of kaon nuclear and Coulomb potentials should lead to a deviation of the cross section from the solid curve calculated without the above potentials. The signature of the effect will be an A-dependent dip in the cross sections at laboratory kaon momentum around 1.47 GeV/c corresponding to zero K^+ meson momentum relative to the projectile nucleus system.

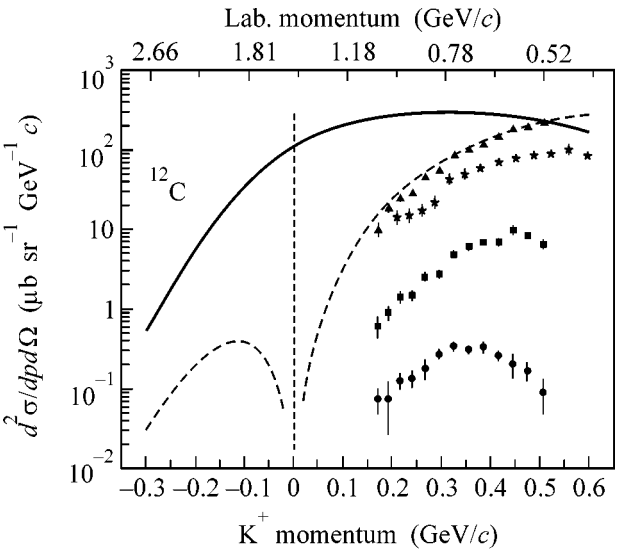

Fig. 1. Double differential K^+ production cross sections. Circles denote the cross sections measured in proton–carbon collisions at T_p = 1.0 GeV; squares, at T_p = 1.2 GeV; stars, at T_p = 1.5 GeV; and triangles, at T_p = 2.0 GeV [16]. Dashed line is our calculation for T_p= 2.0 GeV in the direct kinematics. Solid curve represents the corresponding cross section for K^+ production in carbon–proton collisions at the ion beam energy 2 AGeV.

The evidence for the action of Coulomb and nuclear potentials on soft kaon production was obtained in [17], where the ratio of forward K^+ meson yield from copper, silver and gold targets to that on carbon has been mea-

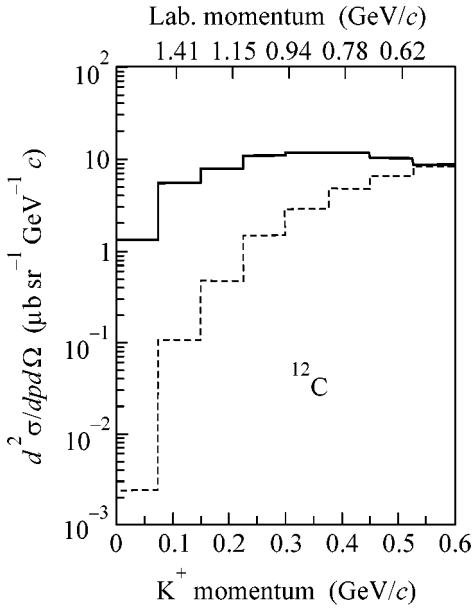

Fig. 2. Double differential K^- production cross sections in the direct (dashed histogram) and inverse (solid histogram) kinematics.

sured at proton beam energies between 1.5 and 2.3 GeV. It was found that, in the momentum range from 170 to 600 MeV/*c*, the ratios exhibit similar shape rising with decreasing kaon momentum, passing a maximum and falling down at momenta less than 250 MeV/*c*. The magnitude of the K^+–nucleus repulsive potential was found to be 20 MeV at normal nuclear density. The authors plan to extend the measurements of the ratios that are not trivial experimental tasks down to a kaon momentum of about 100 MeV/*c*. In the inverse kinematics, both forward and backward production ranges in the nucleus rest frame can be studied simultaneously because all produced kaons are peaked forward in the laboratory. As a result, the momentum dependence of the ratio of K^+ production cross section measured with heavy projectile ions to that measured with light ones should exhibit distinct two peak structure.

2. Study of the in-medium antikaon potential. Let us consider K^- meson production by an ion beam of energy 2.5 *A*GeV on a hydrogen target. The K^- mesons produced in the backward hemisphere (relative to the beam direction) with momenta up to 0.3 GeV/*c* in the projectile nucleus rest frame were observed in the laboratory momentum ranges $0.94 \le P_l \le 1.74$ GeV/*c* and $0 \le P_t \le 0.3$ GeV/*c*. This process corresponds to low-momentum K^- production by protons on the nuclear target in the forward hemisphere. The available experimental information about subthreshold antikaons from proton–nucleus collisions is very scarce [11, 18]. Data on the production of K^- mesons with small momenta are currently completely nonexistent. Under these circumstances, we have to rely upon the model calculations to evaluate the respective cross section. The forward K^- mesons production in the $p + A \longrightarrow K^- + X$ reaction at the proton beam energy 2.5 GeV was studied in [10] within a coupled channel transport approach. The dashed histogram in Fig. 2 shows the K^- momentum spectrum for the ^{12}C target calculated in [10] with zero potentials but taking into account the antikaon absorption in its way out through the nucleus. The solid histogram in the figure depicts the double differential cross section for the K^- meson production in $^{12}C + p$ collisions obtained from the dashed histogram by using Eq. (1). The upper scale represents the corresponding laboratory momenta (in GeV/*c*) of the K^- mesons from carbon–proton collisions. Taking into account the values of the antikaon production cross sections and the sizable decrease of their decay losses, we conclude that the expected event rate in low K^- momentum range is acceptable for measurements in the *Ap* kinematics.

Impact of the surrounding medium on slow K^- production should differ from that on K^+ due to an attractive nature of both Coulomb and nuclear potentials. Action of the Coulomb potential will populate the low-momentum range while the influence of the nuclear potential depends sensitively on its strength. One can expect that, in the case of weak potential, the yield of the K^- mesons will be suppressed due to their strong absorption via the $K^- + N \longrightarrow \Sigma + \pi$ reaction which has a very large cross section at small antikaon momentum. On the contrary, in the case of strong potential exceeding 100 MeV, the K^- mesons absorption plays a minor role because the above process is energetically almost closed [19]. This will lead to an enhanced low-momentum K^- meson yield even from heavy nuclei. The calculations [10] with an attractive antikaon potential of 120 MeV give an enhancement by a factor of about 10 in the cross sections for low momentum K^-. It is therefore necessary to explore this question experimentally by measuring the K^- spectra in the inverse kinematics as a function of the projectile nucleus mass.

If an attractive antikaon–nucleus potential turns out to be large, it will be a strong argument for the existence of narrow discrete nuclear antikaon bound states (see [19] and references therein). The use of inverse kinematics could be a promising way to produce such states.

It should be noticed that slow pions inside nuclei can also be explored in inverse kinematics. Such measurements may help to disentangle the effects of the Coulomb and nuclear potentials on kaon and antikaon production.

3. Study of the subthreshold reaction mechanism. As was mentioned above, the kaon and antikaon production in proton–nucleus interactions below the free *NN* threshold is reduced to one-step and two-step processes due to the lack of collision energy. It is commonly believed that the reaction mechanism can be

identified from the target atomic mass dependence of the cross sections. The *A*-dependence for the one-step process is determined by the total inelastic cross section and scales, as $\approx A^{2/3}$ provided weak final state absorption of the produced mesons. The stronger dependence $\approx A^1$ is expected for the two-step kaon creation process, since the correlating cross section includes the additional probability of the second collision of an intermediate pion with another target nucleon which is proportional to $\approx A^{1/3}$. The total K^+ production cross section on different nuclei has been measured in [20] at the proton energy 1 GeV, which is far below the free *NN* threshold (T_{NN} = 1.58 GeV). Note that low-momentum kaons give the main contribution to the total cross section. By fitting to the cross sections with an A^α function, the exponent α was found to be 1.04 ± 0.03. The strong *A*-dependence has been interpreted in [20, 21] as an evidence for the dominance of the two-step reaction mechanism. Recently, the ANKE Collaboration obtained the data on double differential cross sections for low-momentum K^+ production on nuclear targets from carbon to gold at the same proton energy 1 GeV [22]. The extracted value of α = 0.74 ± 0.05 is in reasonable agreement with the *A*-dependence expected for the one-step mechanism. This discrepancy does not allow one to draw an unambiguous conclusion about the underlying reaction mechanism of slow K^+ production in *pA* collisions [23].

Investigation of low momentum kaon in the inverse kinematics seems the most promising way to clarify the situation. Use of different ion beams provides the possibility of exploring the atomic mass dependence. At projectile energy 1 *A*GeV, the K^+ meson emission in the backward hemisphere (relative to the ion beam direction) within the momentum range 0–0.3 GeV/*c* in the projectile nucleus rest frame looks like forward kaon production in the laboratory momentum intervals $0.43 \le P_l \le 0.89$ GeV/*c* and $0 \le P_t \le 0.3$ GeV/*c*. This makes the measurements in the inverse kinematics more favorable than those in the direct kinematics. For instance, since the K^+ meson momentum 0.1 GeV/*c* relative to the projectile nucleus corresponds to the laboratory momentum 0.7 GeV/*c*, the differential cross section in *Ap* collisions is enhanced by a factor of 30 (Eq. (1)). Furthermore, at a distance between the production target and the detectors of about 2.5 m (corresponding to the actual experimental situation), the loss of the kaons due to their decay in flight is decreased by more than an order of magnitude. Therefore, the K^+ event rate would exceed that in traditional kinematics by about a factor of 400. The corresponding enhancement in the event rate of the K^- mesons with the same momentum is equal to 800 at ion beam energy 2 *A*GeV which is far enough below the free *NN* threshold (T_{NN} = 2.50 GeV). Due to the Lorentz boost, all kaons and antikaons produced in full solid angle with momenta <300 MeV/*c* relative to the projectile nucleus rest frame will be concentrated in the laboratory inside a rather narrow cone of 10°–20° that corresponds to the solid angle of 1–3% of 4π. Note that the multiple scattering effect on the detected particles is significantly decreased in the *Ap* kinematics due to upward shift of both kaon momentum and velocity. Thus, the inverse kinematics is well suited for the experimental study of the mechanisms of deep subthreshold low-momentum strange meson production.

The feasibility of the experiments discussed above depends on backgrounds. Subthreshold K^+ and K^- meson production is accompanied by the background of secondary pions and protons which is much more intense. Note that the modern magnetic spectrometers provide reliable K/π and K/p separation up to values of these ratios 10^{-6}–10^{-7} [15, 22]. Another source of background is the particle production from an envelope of the hydrogen target. Usually, "target full–target empty" measurements have to be carried out to obtain cross sections on hydrogen. However, this background can be totally removed by using the windowless target consisting of frozen hydrogen pellets [24].

It is worth noting that the method discussed opens a way to explore the properties of low-momentum η, η', ω, ρ, and ϕ mesons in nuclear matter, which is a topic extensively discussed over recent years [25]. Experiments in the inverse kinematics may be carried out at GSI-SIS using ion beams in the region of 1–2 *A*GeV and at an ITEP where ion beams of energy up to 4.3 *A*GeV are expected to be available in the near future.

We are grateful to E.Ya. Paryev for useful discussions.

REFERENCES

1. W. Cassing and E. L. Bratkovskaya, Phys. Rep. **308**, 65 (1999).
2. W. Weise, Nucl. Phys. A **610**, 35 (1996).
3. D. B. Kaplan and A. E. Nelson, Phys. Lett. B **175**, 57 (1986).
4. G. E. Brown, C.-H. Lee, M. Rho, and V. Thorsson, Nucl. Phys. **567**, 937 (1994).
5. T. Maruyama, H. Fujii, T. Muto, and T. Tatsumi, Phys. Lett. B **337**, 19 (1994).
6. N. Herrmann (FOPI Collab.), Nucl. Phys. A **610**, 49 (1996).
7. R. Barth, P. Senger, W. Ahner, *et al.*, Phys. Rev. Lett. **78**, 4007 (1997).
8. W. Cassing, E. L. Bratkovskaya, U. Mosel, *et al.*, Nucl. Phys. A **614**, 415 (1997).
9. C. J. Batty, E. Friedman, and A. Gal, Phys. Rep. **287**, 385 (1997).
10. A. Sibirtsev and W. Cassing, Nucl. Phys. A **641**, 476 (1998).
11. Yu. T. Kiselev (for the FHS Collab.), J. Phys. G **25**, 381 (1999).
12. E. Y. Paryev, Eur. Phys. J. A **9**, 521 (2000).

13. J. Schaffner-Bielich, V. Koch, and M. Effenberger, Nucl. Phys. A **669**, 153 (2000).
14. L. Tolos, A. Ramos, A. Polls, and T. T. S. Kuo, Nucl. Phys. A **690**, 547 (2001).
15. A. V. Akindinov, M. M. Chumakov, Yu. T. Kiselev, *et al.*, JETP Lett. **72**, 100 (2000).
16. M. Nekipelov and V. Koptev, in *Proceedings of 5th International Conference on Nuclear Physics at Storage Rings, Uppsala, Sweden, 2002* (in press).
17. M. Nekipelov, M. Busher, W. Cassing, *et al.*, Phys. Lett. B **540**, 207 (2002).
18. W. Scheinast (for the KaoS Collab.), Acta Phys. Pol. B **31**, 2305 (2000).
19. T. Yamazaki and Y. Akaishi, Phys. Lett. B **535**, 70 (2002).
20. N. K. Abrosimov, V. Koptev, S. Mikirtychiants, *et al.*, Sov. Phys. JETP **67**, 2177 (1988).
21. W. Cassing, G. Batko, G. Mosel, *et al.*, Phys. Lett. B **238**, 25 (1990).
22. V. Koptev, M. Busher, H. Junghans, *et al.*, Phys. Rev. Lett. **87**, 022301 (2001).
23. M. Buesher, B. L. Ioffe, V. Koptev, *et al.*, Phys. Rev. C **65**, 014603 (2002).
24. B. Trostell, Nucl. Instrum. Methods Phys. Res. A **362**, 41 (1995).
25. K. Tsushima, A. Sibirtsev, K. Saito, *et al.*, Nucl. Phys. A **680**, 280 (2001); R. S. Hayano, Nucl. Phys. A **680**, 125 (2001); F. Klingl, T. Waas, and W. Weise, Nucl. Phys. A **650**, 299 (1999); L. A. Kondratyuk, A. Sibzirtsev, W. Cassing, *et al.*, Phys. Rev. C **58**, 1078 (1998); H. Gao, T.-S. Lee, and V. Marinov, Phys. Rev. C **63**, 022201(R) (2001).

JETP Letters, Vol. 78, No. 9, 2003, pp. 533–537. From Pis'ma v Zhurnal Éksperimental'noĭ i Teoreticheskoĭ Fiziki, Vol. 78, No. 9, 2003, pp. 1021–1025.

Classical and Quantum Regimes of Superfluid Turbulence¶

G. E. Volovik

Low Temperature Laboratory, Helsinki University of Technology, FIN-02015 HUT, Finland
Landau Institute for Theoretical Physics, Russian Academy of Sciences, Moscow, 117940 Russia
e-mail: volovik@boojum.hut.fi

Received October 6, 2003

We argue that turbulence in superfluids is governed by two dimensionless parameters. One of them is the intrinsic parameter q which characterizes the friction forces acting on a vortex moving with respect to the heat bath, with q^{-1} playing the same role as the Reynolds number $\mathrm{Re} = UR/\nu$ in classical hydrodynamics. It marks the transition between the "laminar" and turbulent regimes of vortex dynamics. The developed turbulence described by Kolmogorov cascade occurs when $\mathrm{Re} \gg 1$ in classical hydrodynamics, and $q \ll 1$ in superfluid hydrodynamics. Another parameter of superfluid turbulence is the superfluid Reynolds number $\mathrm{Re}_s = UR/\kappa$, which contains the circulation quantum κ characterizing quantized vorticity in superfluids. This parameter may regulate the crossover or transition between two classes of superfluid turbulence: (i) the classical regime of Kolmogorov cascade where vortices are locally polarized and the quantization of vorticity is not important; (ii) the quantum Vinen turbulence whose properties are determined by the quantization of vorticity. A phase diagram of the dynamical vortex states is suggested. © *2003 MAIK "Nauka/Interperiodica".*

PACS numbers: 47.37.+q; 47.32.Cc; 67.40.Vs; 67.57.Fg

1. INTRODUCTION

The hydrodynamics of superfluid liquid exhibits new features with respect to conventional classical hydrodynamics, which are important when the turbulence in superfluids is considered [1].

(i) The superfluid liquid consists of two mutually penetrating components: the frictionless superfluid component and the viscous normal component. That is why different types of turbulent motion are possible, depending on whether the normal and superfluid components move together or separately. Here, we are interested in the simplest case, when the dynamics of the normal component can be neglected. This occurs, for example, in superfluid phases of ^{3}He where the normal component is so viscous that it is practically clamped by the container walls. Its role is to provide the preferred reference frame, where the normal component and, thus, the heat bath are at rest. The turbulence in the superfluid component with the normal component at rest is referred to as the superfluid turbulence.

(ii) An important feature of the superfluid turbulence is that the vorticity of the superfluid component is quantized in terms of the elementary circulation quantum κ. So, the superfluid turbulence is the chaotic motion of well-determined and well-separated vortex filaments [1]. Using this, we can simulate the main ingredient of the classical turbulence, the chaotic dynamics of the vortex degrees of freedom of the liquid.

(iii) Further simplification comes from the fact that the dissipation of the vortex motion is not due to the viscosity term in the Navier–Stokes equation which is proportional to the velocity gradients $\nabla^2\mathbf{v}$ in classical liquid, but due to the friction force acting on the vortex when it moves with respect to the heat bath (the normal component). This force is proportional to velocity of the vortex, and thus the complications that result from the $\nabla^2\mathbf{v}$ term are avoided.

Here, we discuss how these new features could influence the superfluid turbulence.

2. COARSE-GRAINED HYDRODYNAMIC EQUATION

The coarse-grained hydrodynamic equation for the superfluid vorticity is obtained from the Euler equation for the superfluid velocity $\mathbf{v} \equiv \mathbf{v}_s$ after averaging over the vortex lines (see the review paper [2]). Instead of the Navier–Stokes equation with $\nabla^2\mathbf{v}$ term, one has

$$\frac{\partial \mathbf{v}}{\partial t} + \nabla\mu = \mathbf{v}\times\boldsymbol{\omega} \qquad (1)$$

$$-\alpha'(\mathbf{v}-\mathbf{v}_n)\times\boldsymbol{\omega} + \alpha\hat{\boldsymbol{\omega}}\times(\boldsymbol{\omega}\times(\mathbf{v}-\mathbf{v}_n)). \qquad (2)$$

Here, $\mathbf{v}_n$ is the velocity of the normal component; $\boldsymbol{\omega} = \nabla\times\mathbf{v}$ is the superfluid vorticity; $\hat{\boldsymbol{\omega}} = \boldsymbol{\omega}/\omega$; and dimensionless parameters α' and α come from the reactive and dissipative forces acting on a vortex when it moves with respect to the normal component. These parameters are very similar to the Hall resistivity ρ_{xy} and ρ_{xx} in

¶ This article was submitted by the author in English.

the Hall effect. For vortices in fermionic systems (superfluid ^{3}He and superconductors), they were calculated by Kopnin [3] and measured in ^{3}He–B in the broad temperature range by Bevan *et al.* [4] (see also [5], where these parameters are discussed in terms of the chiral anomaly).

The terms in Eq. (1) are invariant with respect to the transformation $\mathbf{v} \longrightarrow \mathbf{v}(\mathbf{r} - \mathbf{u}t) + \mathbf{u}$, as in classical hydrodynamics. However, the terms in Eq. (2) are not invariant under this transformation since there is a preferred reference frame in which the normal component is at rest. They are invariant under the full Galilean transformation when the normal component is also involved: $\mathbf{v} \longrightarrow \mathbf{v}(\mathbf{r} - \mathbf{u}t) + \mathbf{u}$ and $\mathbf{v}_n \longrightarrow \mathbf{v}_n + \mathbf{u}$.

Further, we shall work in the frame where $\mathbf{v}_n = 0$, but we must remember that this frame is unique. In this frame, the equation for superfluid hydrodynamics is simplified:

$$\frac{\partial \mathbf{v}}{\partial t} + \nabla\mu = (1 - \alpha')\mathbf{v} \times \boldsymbol{\omega} + \alpha\hat{\boldsymbol{\omega}} \times (\boldsymbol{\omega} \times \mathbf{v}). \quad (3)$$

After rescaling the time such that $\tilde{t} = (1 - \alpha')t$, one obtains an equation which depends on a single parameter $q = \alpha/(1 - \alpha')$:

$$\frac{\partial \mathbf{v}}{\partial \tilde{t}} + \nabla\tilde{\mu} = \mathbf{v} \times \boldsymbol{\omega} + q\hat{\boldsymbol{\omega}} \times (\boldsymbol{\omega} + \mathbf{v}). \quad (4)$$

Now, the first three terms together are the same as inertial terms in classical hydrodynamics. They satisfy the modified Galilean invariance (in fact, the transformation below changes the chemical potential, but this does not influence the vortex degrees of freedom which are important for the phenomenon of turbulence):

$$\mathbf{v}(\tilde{t}, \mathbf{r}) \longrightarrow \mathbf{v}(\tilde{t}, \mathbf{r} - \mathbf{u}\tilde{t}) + \mathbf{u}. \quad (5)$$

On the contrary, the dissipative last term with the factor q in Eq. (4) is not invariant under this transformation. This is in contrast to conventional liquid, where the whole Navier–Stokes equation which contains viscosity

$$\frac{\partial \mathbf{v}}{\partial t} + \nabla\mu = \mathbf{v} \times \boldsymbol{\omega} + \nu\nabla^2\mathbf{v}, \quad (6)$$

is Galilean invariant, and where there is no preferred reference frame.

Such a difference between the dissipative last terms in Eqs. (6) and (4) is very important:

(1) The role of the Reynolds number, which characterizes the ratio of inertial and dissipative terms in hydrodynamic equations, in superfluid turbulence is played by the intrinsic parameter $1/q$. This parameter does not depend on the characteristic velocity U and size R of the large-scale flow as it is distinct from the conventional Reynolds number $\mathrm{Re} = RU/\nu$ in classical viscous hydrodynamics. That is why the turbulent regime occurs only at $1/q > 1$ even if vortices are injected to the superfluid which moves with large velocity U. This rather unexpected result was obtained in recent experiments with the superfluid ^{3}He–B [6].

(2) In conventional turbulence, the large-scale velocity U is always understood as the largest characteristic velocity difference in the inhomogeneous flow of classical liquid [7]. In the two-fluid system, the velocity U is the large-scale velocity of the superfluid component with respect to the normal component, and this velocity (the so-called counterflow velocity) can be completely homogeneous.

(3) As a result, as distinct from classical hydrodynamics, the energy dissipation, which is produced by the last term in Eq. (4), depends explicitly on U:

$$\epsilon = -\dot{E} = -\left\langle \mathbf{v} \cdot \frac{\partial \mathbf{v}}{\partial \tilde{t}} \right\rangle = -q\left\langle \mathbf{v} \cdot (\hat{\boldsymbol{\omega}} \times (\boldsymbol{\omega} \times \mathbf{v})) \right\rangle \sim q\omega U^2. \quad (7)$$

(4) The onset of the superfluid turbulence was studied in [8], where a model was developed which demonstrated that the initial avalanche-like multiplication of vortices leading to turbulence occurs when $q \lesssim 1$ is in agreement with experiment [6]. The existence of two regimes in the initial development of vorticity is also supported by earlier simulations by Schwarz who noted that, when α (or q) is decreased, the crossover from a regime of isolated phase slips to a phase-slip cascade and then to fully developed vortex turbulence occurs [9]. One can expect that well-developed turbulence occurs when $q \ll 1$, and here we shall discuss this extreme limit. In ^{3}He–B, the condition $q \ll 1$ can be realized at temperatures well below $0.6T_c$ [6]. However, we do not consider a very low T where, instead of the mutual friction, the other mechanisms of dissipation take place such as excitation of Kelvin waves [10] and vortex reconnection [11]. The latter leads to the formation of cusps and kinks on the vortex filaments whose fast dynamics creates a burst of different types of excitations in quantum liquids: phonons, rotons, Kelvin waves, and fermionic quasiparticles. The burst of gravitational waves from cusps and kinks of cosmic strings was theoretically investigated by the cosmological community (see, e.g., [12]), and the obtained results are very important for superfluid turbulence at a very low temperature.

(5) We expect that, even at $q \ll 1$, two different states of turbulence are possible, with the crossover (or transition) between them being determined by q and by another dimensionless parameter $\mathrm{Re}_s = UR/\kappa$, where κ is the circulation around the quantum vortex. The coarse-grained hydrodynamic equation (4) is, in fact, valid only in the limit $\mathrm{Re}_s \gg 1$, since the latter means that the characteristic circulation of velocity $\Gamma = UR$ of the large-scale flow substantially exceeds the circulation quantum κ, and thus there are many vortices in the turbulent flow. When Re_s decreases, the quantum nature of vortices becomes more pronounced, and we proceed from the type of the classical turbulence, which is prob-

ably described by the Kolmogorov cascade, to the quantum regime, which is probably described by the Vinen equations for the average vortex dynamics [13].

Let us consider the possibility of the Kolmogorov state of the superfluid turbulence.

3. KOLMOGOROV CASCADE

In classical turbulence, the large Reynolds number $\mathrm{Re} = UR/\nu \gg 1$ leads to well-separated length scales or wave numbers. As a result, a Kolmogorov–Richardson cascade takes place, in which the energy flows from small wave numbers $k_{\min} \sim 1/R$ (large rings of size R of the container) to high wave number $k_0 = 1/r_0$ where the dissipation occurs. In the same manner, in our case of superfluid turbulence, the necessary condition for the Kolmogorov cascade is the big ratio of the inertial and dissipative terms in Eq. (4), i.e., $1/q \gg 1$.

In the Kolmogorov–Richardson cascade, at arbitrary length scale r, the energy transfer rate to the smaller scale, say $r/2$, is $\epsilon = E_r/t_r$, where $E_r = v_r^2$ is the kinetic energy at this scale, and $t_r = r/v_r$ is the characteristic time. The energy transfer from scale to scale must be the same for all scales; as a result, one has

$$\epsilon = \frac{E_r}{t_r} = \frac{v_r^3}{r} = \text{constant} = \frac{U^3}{R}. \tag{8}$$

From this equation, it follows that

$$v_r = \epsilon^{1/3} r^{1/3}. \tag{9}$$

This must be valid both in classical and superfluid liquids [14]. What is different is the parameter ϵ: it is determined by the dissipation mechanism, which is different in two liquids.

From Eq. (7) with $\omega_r = v_r/r$, it follows that, as in the classical turbulence, major dissipation occurs at the smallest possible scales, but the structure of ϵ is now different. Instead of $\epsilon = \nu v_{r0}/r_0^2$ in classical liquids, we now have

$$\epsilon \sim q\omega_{r0}U^2 \sim qU^2\frac{v_{r0}}{r_0} = qU^2\epsilon^{1/3}r_0^{-2/3}. \tag{10}$$

Since $\epsilon = U^3/R$, from Eq. (10) one obtains that the scale r_0 at which the main dissipation occurs and the characteristic velocity v_{r_0} at this scale are

$$r_0 \sim q^{3/2}R, \quad v_{r0} \sim q^{1/2}U. \tag{11}$$

This consideration is valid when $r_0 \ll R$ and $v_{r0} \ll U$, which means that $1/q \gg 1$ is the condition for the Kolmogorov cascade. In classical liquids, the corresponding condition for well-developed turbulence is $\mathrm{Re} \gg 1$. In both cases, these conditions ensure that the kinetic terms in the hydrodynamic equations are much larger than the dissipative terms. In the same manner, as in classical liquids, the condition for the stability of the turbulent flow is $\mathrm{Re} > 1$, such that one may suggest that the condition for the stability of the discussed turbulent flow is $1/q > 1$. This is supported by observations in ^{3}He–B where it was demonstrated that, at high velocity U but at $q > 1$, the turbulence does not develop even after vortices were introduced into the flow [6].

As in the Kolmogorov cascade for the classical liquid, in the Kolmogorov cascade of superfluid turbulence the dissipation is concentrated at small scales,

$$\epsilon \sim qU^2\int_{r_0}^{R}\frac{dr}{r}\frac{v_r}{r} \sim qU^2\frac{v_{r0}}{r_0}, \tag{12}$$

while the kinetic energy is concentrated at large scale of container size:

$$E = \int_{r_0}^{R}\frac{dr}{r}v_r^2 = \int_{r_0}^{R}\frac{dr}{r}(\epsilon r)^{2/3} = (\epsilon R)^{2/3} = U^2. \tag{13}$$

The dispersion of the turbulent energy in the momentum space is the same as in classical liquid

$$E = \int_{r_0}^{R}\frac{dr}{r}(\epsilon r)^{2/3} = \int_{k_0}^{1/R}\frac{dk}{k}\frac{\epsilon^{2/3}}{k^{2/3}} = \int_{k_0}^{1/R}dkE(k),$$
$$E(k) = \epsilon^{2/3}k^{-5/3}. \tag{14}$$

As distinct from the classical liquid, where k_0 is determined by viscosity, in the superfluid turbulence the cutoff k_0 is determined by mutual friction parameter q: $k_0 = 1/r_0 = R^{-1}q^{-3/2}$.

4. CROSSOVER TO VINEN QUANTUM TURBULENCE

At a very small q, the quantization of circulation becomes important. The condition of the above consideration is that the relevant circulation can be considered continuous, i.e., the circulation at the scale r_0 is larger than the circulation quantum: $v_{r0}r_0 > \kappa$. This gives

$$v_{r0}r_0 = q^2UR = q^2\kappa\mathrm{Re}_s > \kappa, \quad \mathrm{Re}_s = \frac{UR}{\kappa}, \tag{15}$$

i.e., the constraint for the application of the Kolmogorov cascade is

$$\mathrm{Re}_s > \frac{1}{q^2} \gg 1. \tag{16}$$

Another requirement is that the characteristic scale r_0 must be much larger than the intervortex distance l. The latter is obtained from the vortex density in the Kolmogorov state $n_K = l^{-2} = \omega_{r0}/\kappa = v_{r0}/(r_0\kappa)$. The condition $l \ll r_0$ again leads to the equation $v_{r0}r_0 > \kappa$ and, thus, to the criterion (16).

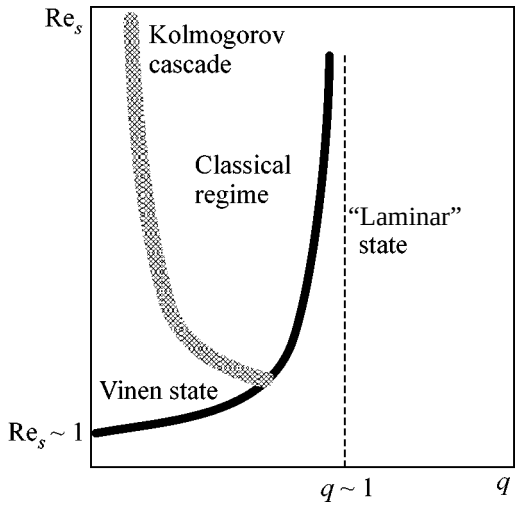

Possible phase diagram of dynamical vortex states in Re_s, q plane. At large flow velocity $\mathrm{Re}_s \gg 1$, the boundary between the turbulent and "laminar" vortex flow approaches the vertical axis at $q = q_0 \sim 1$ as suggested by experiment [6]. The thick line separates the developed turbulence of the classical type, which is characterized by the Kolmogorov cascade at small q, and the quantum turbulence of the Vinen type.

Note that here, for the first time, the "superfluid Reynolds number" Re_s appears, which contains the circulation quantum. Thus, the superfluid Reynolds number is responsible for the crossover or transition from the classical superfluid turbulence, where the quantized vortices are locally aligned (polarized), and thus the quantization is not important, to the quantum turbulence developed by Vinen.

We can now consider the approach to the crossover from the quantum regime—the Vinen state which probably occurs when $\mathrm{Re}_s q^2 < 1$. According to Vinen [13], the characteristic microscopic length scale, the distance between the vortices or the size of the characteristic vortex loops, is determined by the circulation quantum and the counterflow velocity, $l = \lambda\kappa/U$, where λ is the dimensionless intrinsic parameter, which probably contains α' and α. The vortex density in the Vinen state is

$$n_{\mathrm{V}} = l^{-2} \sim \lambda^2 \frac{U^2}{\kappa^2} = \frac{\lambda^2}{R^2}\mathrm{Re}_s^2. \qquad (17)$$

It differs from the vortex density in the Kolmogorov state

$$n_{\mathrm{K}} = \frac{v_{r0}}{\kappa r_0} \sim \frac{U}{q\kappa R} = \frac{1}{R^2}\frac{\mathrm{Re}_s}{q}, \qquad (18)$$

which depends not only on the counterflow velocity U but also on the container size R.

If the crossover between the classical and quantum regimes of the turbulent states occurs at $\mathrm{Re}_s q^2 = 1$, the two equations (17) and (18) must match each other in the crossover region. But this occurs only if $\lambda^2 = q$. If $\lambda^2 \neq q$, there is a mismatch, and one may expect that either the two states are separated by a first-order phase transition, or there is an intermediate region where the superfluid turbulence is described by two different microscopic scales such as r_0 and l. Based on the above consideration, one may suggest the following phase diagram of different regimes of collective vortex dynamics in the figure.

5. DISCUSSION

Superfluid turbulence is the collective many-vortex phenomenon which can exist in different states. Each of the vortex states can be characterized by its own correlation functions. For example, the states can be characterized by the loop function

$$g(C) = \left\langle \exp\left\{ i(2\pi/\kappa)\oint_C \mathbf{v}\cdot d\mathbf{r} \right\} \right\rangle. \qquad (19)$$

In the limit when the length L of the loop C is much larger than the intervortex distance l, one may expect the general behavior $g(L) \sim \exp(-(L/l)^\gamma)$ where the exponent γ is different for different vortex states.

One can expect the phase transitions between different states of collective vortex dynamics. One of such transitions, which appeared to be rather sharp, has been observed between the "laminar" and "turbulent" dynamics of vortices in superfluid ^{3}He–B [6]. It was found this type of transition was regulated by intrinsic velocity-independent dimensionless parameter $q = \alpha/(1 - \alpha')$. However, it is not excluded that both dimensionless parameters α and α' are important, and also it is possible that only the initial stage of the formation of the turbulent state is governed by these parameters [8]. Another transition (or possibly crossover) is suggested here between the quantum and classical regimes of the developed superfluid turbulence, though there are arguments that the classical regime can never be reached because the vortex stretching is missing in the superfluid turbulence [15].

In principle, the parameters α and α' may depend on the type of the dynamical state, since they are obtained by averaging the forces acting on individual vortices. The renormalization of these parameters $\alpha(L)$ and $\alpha'(L)$ when the length scale L is increasing may also play an important role in the identification of the turbulent states, as in the case of the renormalization-group flow of similar parameters in the quantum Hall effect (see, e.g., [16]).

I thank V.B. Eltsov, D. Kivotides, N.B. Kopnin, and M. Krusius for discussions. This work was supported by the ESF COSLAB Programme and the Russian Foundation for Basic Research.

REFERENCES

1. W. F. Vinen and J. J. Niemela, J. Low Temp. Phys. **128**, 167 (2002).
2. E. B. Sonin, Rev. Mod. Phys. **59**, 87 (1987).
3. N. B. Kopnin, *Theory of Nonequilibrium Superconductivity* (Clarendon Press, Oxford, 2001).
4. T. D. C. Bevan, A. J. Manninen, J. B. Cook, *et al.*, Nature **386**, 689 (1997); J. Low Temp. Phys. **109**, 423 (1997).
5. G. E. Volovik, *The Universe in a Helium Droplet* (Clarendon Press, Oxford, 2003).
6. A. P. Finne, T. Araki, R. Blaauwgeers, *et al.*, Nature **424**, 1022 (2003).
7. W. D. McComb, *The Physics of Fluid Turbulence* (Clarendon Press, Oxford, 1990).
8. N. B. Kopnin, cond-mat/0309708.
9. K. W. Schwarz, Physica B (Amsterdam) **197**, 324 (1994); *Numerical Experiments on Single Quantized Vortices*, Preprint.
10. W. F. Vinen, Makoto Tsubota, and Akira Mitani, Phys. Rev. Lett. **91**, 135301 (2003).
11. Makoto Tsubota, Tsunehiko Araki, and S. K. Nemirovskii, Phys. Rev. B **62**, 11751 (2000).
12. T. Damour and A. Vilenkin, Phys. Rev. D **64**, 064008 (2001).
13. W. F. Vinen, Proc. R. Soc. London, Ser. A **242**, 493 (1957).
14. Makoto Tsubota, Kenichi Kasamatsu, and Tsunehiko Araki, cond-mat/0309364.
15. D. Kivotides, talk on "why superfluid turbulence is not classical" at Seminar of Low Temperature Laboratory (Helsinki Univ. of Technology, October 17, 2003); D. Kivotides and A. Leonard, Phys. Rev. Lett. **90**, 234503 (2003).
16. D. E. Khmelnitskii, Pis'ma Zh. Éksp. Teor. Fiz. **38**, 454 (1983) [JETP Lett. **38**, 552 (1983)].

JETP Letters, Vol. 78, No. 9, 2003, pp. 538–541. Translated from Pis'ma v Zhurnal Éksperimental'noĭ i Teoreticheskoĭ Fiziki, Vol. 78, No. 9, 2003, pp. 1026–1029.

Parametric Transformation of the Amplitude and Frequency of a Whistler Wave in a Magnetoactive Plasma

A. V. Kostrov*, M. E. Gushchin, S. V. Korobkov, and A. V. Strikovskiĭ

Institute of Applied Physics, Russian Academy of Sciences, Nizhni Novgorod, 603950 Russia

**e-mail: kstr@appl.sci-nnov.ru*

Received September 22, 2003

The results of experiments studying the propagation of a high-frequency whistler wave in a magnetized plasma duct in the presence of an intense low-frequency wave also related to the whistler frequency range are reported. Amplitude–frequency modulation of the high-frequency whistler wave trapped in the duct was observed. A deep amplitude modulation of the signal that can lead to its splitting into separate wave packets is observed. It is shown that an increase in the wave propagation path leads to a broadening of the wave frequency spectrum and to a shift of the signal spectrum predominantly toward the red side. The transformation of the frequency of the high-frequency wave is related with the time-dependent perturbation of the external magnetic field by the field of the low-frequency whistler wave (the relative perturbation of the magnetic field $\delta B/B \le 5 \times 10^{-2}$). © *2003 MAIK "Nauka/Interperiodica".*

PACS numbers: 52.25.Xz; 52.35.Hr; 52.72.+v

1. The modulation of waves of the ultralow-frequency range in the Earth's ionosphere and magnetosphere is a phenomenon that has long been known from satellite and ground-based observations [1]. The amplitude and frequency of signals propagating in the circumterrestrial plasma as electron whistlers are transformed both at their resonance interaction with electrons of radiation belts [2] and when the wave passes through regions with a hydrodynamic perturbation of plasma parameters and the geomagnetic field [3]. Variations of these parameters lead to modulation of the frequency and the signal envelope, broadening of their frequency spectrum, and generation of satellites [3–5]. In spite of the fact that parametric and nonlinear effects have long been observed in natural experiments, laboratory modeling of such phenomena has not been performed previously. This paper presents the results of laboratory experiments in which the amplitude–frequency characteristics of a whistler wave propagating in a magnetoactive plasma were studied upon intense time-dependent perturbation of the external field. The experiments were carried out on a unique Krot plasma test bench specially designed for modeling phenomena in the space and circumterrestrial plasmas.

2. The setup represents a vacuum chamber 10 m in length and 3 m in diameter. The magnetic field of a mirror configuration (the mirror ratio $R \simeq 2.4$, Fig. 1b) is created with the use of a solenoid installed inside the vacuum volume. A cylindrical plasma column (1.5 m in diameter and 4 m in length) is formed as a result of a pulsed induction high-frequency (HF) discharge (f = 5 MHz, P_{gen} = 250 kW, t_{pulse} = 1 ms) in argon at a pressure of 7×10^{-4} Torr. The highest plasma density at the discharge moment reaches ~10^{13} cm^{-3}, the temperature of electrons T_e = 10 eV, and the temperature of ions T_i ~ 0.5 eV. The experiments were performed in the decaying plasma mode once the plasma-creating generators were turned off at a moment when the plasma concentration reached $N \simeq 1.2 \times 10^{12}$ cm^{-3}. The decay of plasma was determined by the process of ambipolar diffusion along the magnetic field; the characteristic time of plasma decay was on the order of 10 ms. Under

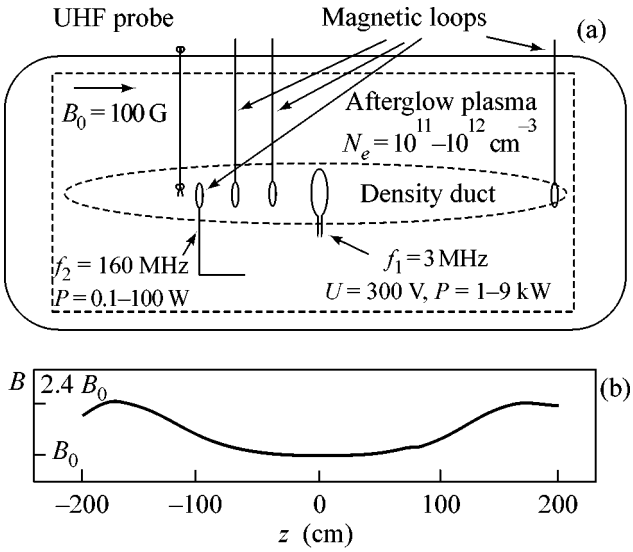

Fig. 1. (a) Schematic diagram of the Krot experimental setup and (b) the distribution of the external magnetic field along the axis of the vacuum chamber.

0021-3640/03/7809-0538$24.00

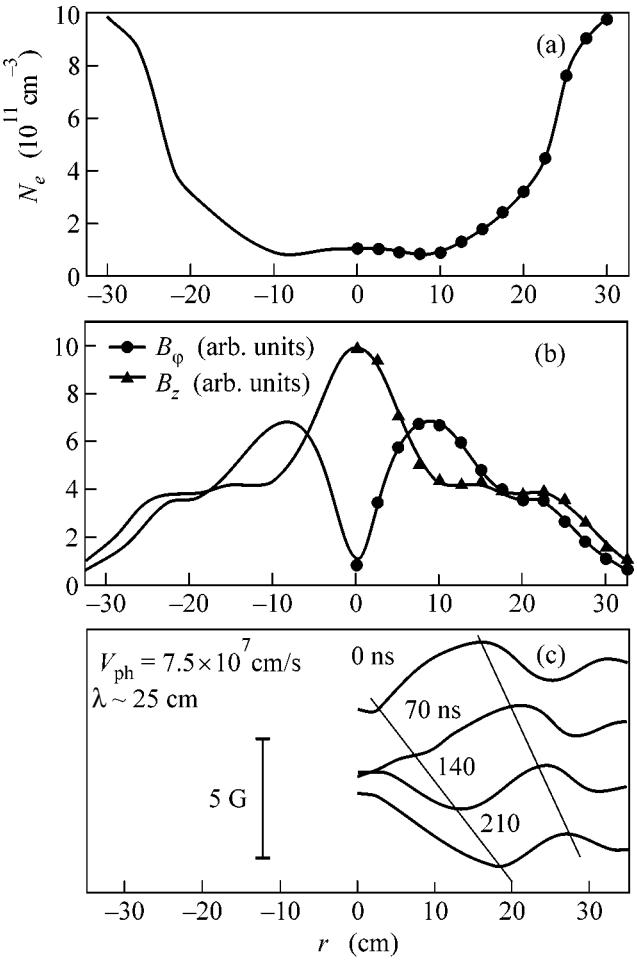

Fig. 2. (a) Radial distributions of the plasma concentration, (b) amplitudes of the B_z and B_φ components of the low-frequency magnetic field (frequency f_1 = 3 MHz), and (c) snapshots of the B_z component of the alternating magnetic field (frequency f_1 = 3 MHz) at different instants of time.

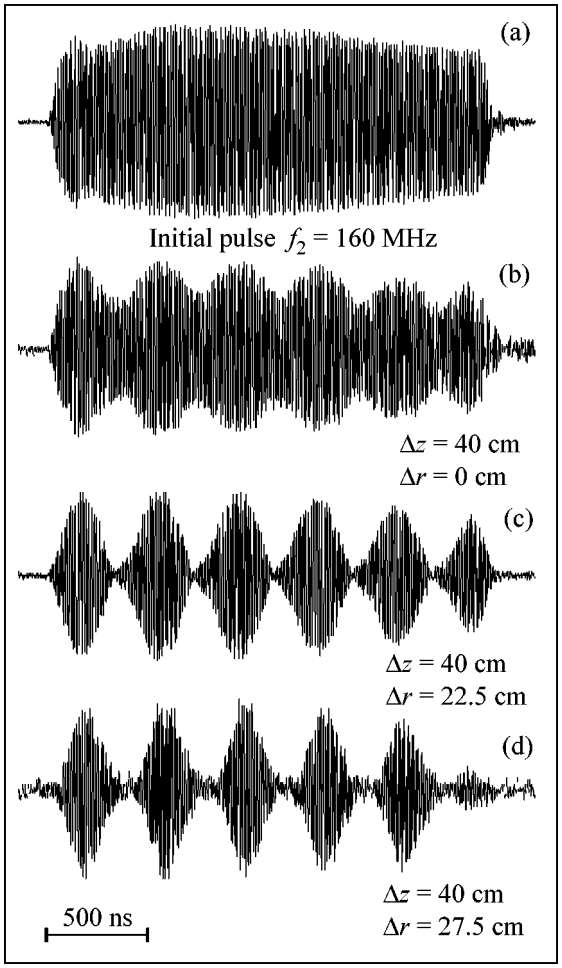

Fig. 3. Oscillograms of a high-frequency pulse (a) radiated into the plasma (f_2 = 160 MHz) and (b), (c), and (d) received from the plasma at different radial positions of the receiving antenna (during a low-frequency perturbation of the plasma at the frequency f_1 = 3 MHz).

the conditions of this experiment, the external magnetic field at a minimum was B_0 = 100 G. Single-turn, screened magnetic antennas 2–3 cm in diameter installed at various sections of the plasma column were used for the radiation and reception of high-frequency whistler waves. The antennas were covered with a thin dielectric layer to decrease the plasma effect on their impedance characteristics. The plasma concentration was measured with the use of a miniature probe with a microwave oscillator made on a section of a twin-wire line.

The excitation of an HF whistler wave was performed by one of the antennas 2 cm in diameter to which a pulse was supplied at a frequency f_2 = 160 MHz with the duration τ = 1–3 μs. A duct with a lowered plasma density extended along the external magnetic field was created in order to channel the radiated wave [6]. The duct was formed with the use of a two-turn loop antenna 20 cm in diameter located at the center of the chamber. A HF voltage pulse was applied across the antenna (f_1 = 3 MHz, U_{HF} = 300 V, P = 9 kW, and Δt = 1 ms). As a result of local heating of electrons, thermodiffusion plasma redistribution occurred in the near field with the formation of a channel with a decreased concentration extended along the system axis in a time on the order of t = 500 μs [6, 7], Fig. 2a. Intense low-frequency (LF) whistler waves ($f_1 \ll f_H$ = 260 MHz) were excited in the duct simultaneously with the heating of electrons. Interferometric measurements showed that the perturbation of the plasma by the LF field is of the wave character; it represents a whistler wave with the wave vector directed almost perpendicular to the direction of the external magnetic field, a so-called conical refraction wave [6] with the transverse wave number $k_\perp \sim \omega_p/c$, Fig. 2c. The amplitude of the alternating magnetic field (the B_z and B_φ components, f_1 = 3 MHz) near the loop antenna was $\delta B \le 5$ G (Figs. 2b, 2c).

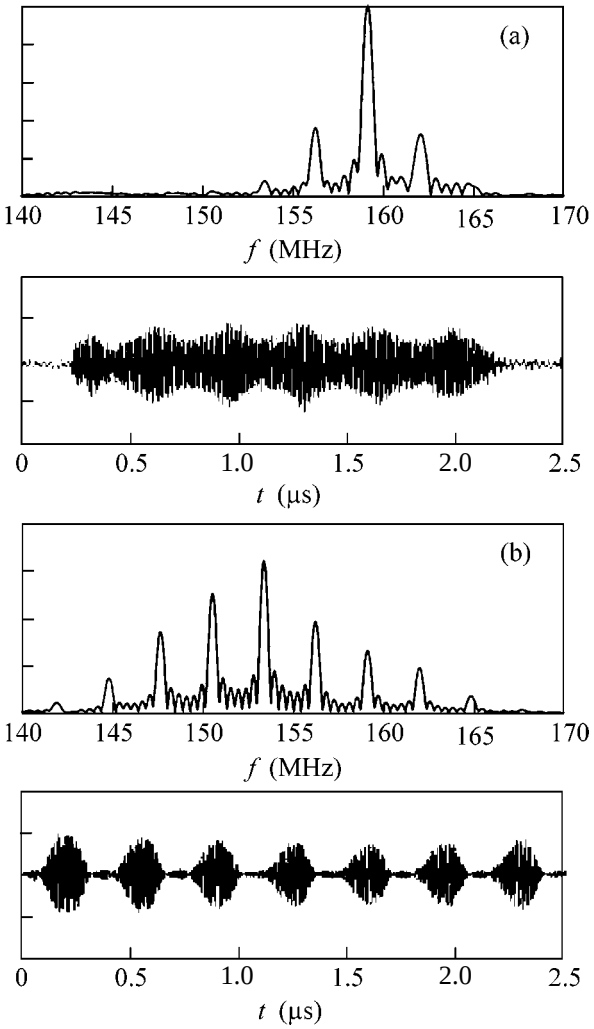

Fig. 4. Typical oscillograms of an HF pulse received from the plasma and spectra of the signals obtained with the use of the Fourier transform (receiving and radiating loops are located at the channel axis): (a) the pulse duration is 2 μs, the receiving and radiating antennas are separated by the distance Δz = 40 cm; and (b) the pulse duration is 3 μs, the receiving and radiating antennas are separated by the distance Δz = 260 cm.

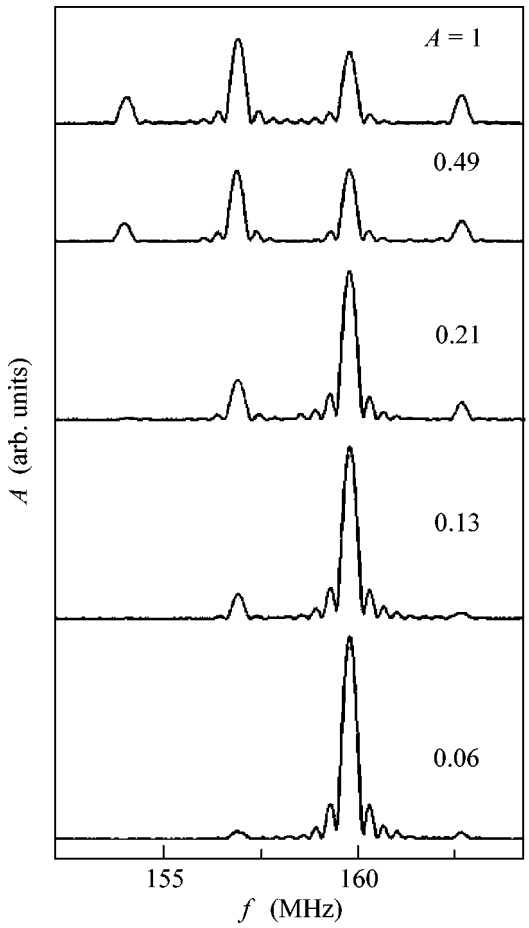

Fig. 5. Transformation of the frequency spectrum of a whistler wave as a function of the relative perturbation of the external magnetic field by an alternating field at the frequency f_1 = 3 MHz ($A \propto \delta B/B_0$, A = 1 corresponds to $\delta B/B_0 \simeq 5\%$).

Typical HF oscillograms (f_2 = 160 MHz) of signals from the receiving antenna are presented in Fig. 3. It is seen that the pulse received from the plasma in the presence of a LF perturbation of the magnetic field is strongly modulated (Fig. 3). The signal may have the form of individual wave packets (Figs. 3c, 3d) whose duration equals half the period of LF field variation (frequency f_1 = 3 MHz). In this case, modulation of the wave carrier frequency (f_2 = 160 MHz) was observed inside the modulation periods of the envelope. The effect of amplitude–frequency modulation of the signal increased as the wave propagation path in the perturbed plasma increased (Fig. 4). At the edge of the plasma channel the antenna detected a low-amplitude signal, but its frequency and envelope were strongly modulated (Fig. 3d).

Spectral measurements showed that, as the wave propagation path increased, the deepening of modulation was accompanied by an increase in the width of the signal frequency spectrum (an increase in the number of satellites of the fundamental frequency) and a shift of the spectrum toward low frequencies (Fig. 4). As the distance between the receiving and radiating antennas increased, the amplitude of the fundamental spectral component (f_2 = 160 MHz) decreased and became lower than the amplitude of the low-frequency satellites (Fig. 4b).

The efficiency of the parametric transformation of the spectrum was investigated as a function of the amplitude of the alternating field (f_1 = 3 MHz) localized in the duct (Fig. 5). As the parameter A increases, the amplitude of the main spectral maximum $f = f_2$ =

160 MHz decreases: the oscillation energy is transferred to the LF spectral components.

3. It is known that the refractive index for electromagnetic waves of the whistler frequency range $\sqrt{\omega_H\Omega_H} < \omega < \omega_H \ll \omega_p$ can be written in the following form:

$$n^2 = \frac{\omega_p^2}{\omega(\omega_H\cos\Theta - \omega)} \quad (1)$$

(c is the velocity of light in free space; ω and k are the frequency and the wave number of the whistler wave, respectively; ω_p and ω_H are the plasma and cyclotron frequencies of electrons, Ω_H is the ion cyclotron frequency, and Θ is the angle between the direction of the external magnetic field $\mathbf{B}_0$ and the wave vector $\mathbf{k}$). From Eq. (1), it is seen that a perturbation of the refractive index can be associated with both variations of the magnetic field (ω_H) and a perturbation of the concentration of plasma electrons (ω_p^2). It is not difficult to show that the relative perturbation of the external magnetic field in the field of a wave with $k_\perp \sim \omega_p/c$ is considerably larger than the relative perturbation of the plasma concentration

$$\frac{\delta N}{N_0} \simeq \left(\frac{\omega_H}{\omega_p}\right)^2 \frac{\delta B}{B_0}, \quad (2)$$

where δN and δB are the perturbations of the density and the magnetic field in the LF whistler wave. Under experimental conditions, $\omega_H/\omega_p \simeq 0.1$. The perturbation of the external magnetic field reaches $\delta B/B \sim 5\%$, and it is the periodic modulation of the magnetic field that makes the main contribution to the parametric effect under study. The shift of the spectrum can be explained by both the interaction of the HF signal with the traveling wave of the parameter (magnetic field) and the strong frequency dependence of the attenuation coefficient of the collisional damping of HF whistler waves.

We would like to call attention to the oscillograms of modulated signals (Figs. 3, 4) unusually shaped as individual, periodically repeated wave packets. This shape of the modulated signal reminds us of oscillograms of ion whistlers received from the circumterrestrial plasma in the ultralow frequency range. These are *Pc-1* (so-called pearl) micropulsations [8]. The similarity of the signals suggests that the mechanism responsible for the generation of the quasi-periodic sequences of "pearls" is similar to the mechanism presented in this paper. It is likely that the *Pc-1* generation is associated with the amplitude–frequency modulation of ion whistlers in the region near the equator by intense LF perturbations of the geomagnetic field.

This work was supported by the Russian Foundation for Basic Research (project no. 01-02-16578), and the Russian Department of Science (financing of unique installations, reg. no. 01-18).

REFERENCES

1. Ya. I. Likhter, O. A. Molchanov, and V. M. Chmyrev, Pis'ma Zh. Éksp. Teor. Fiz. **14**, 475 (1971) [JETP Lett. **14**, 325 (1971)].
2. Y. Omura, D. Nunn, H. Matsumoto, and M. J. Rycroft, J. Atmos. Terr. Phys. **53**, 351 (1991).
3. V. Sotnikov, V. Fiala, F. Lefeuvre, and D. Lagoutte, J. Geophys. Res. **96**, 11363 (1991).
4. S. Ohnami, M. Hayakawa, T. F. Bell, and T. Ondoh, Geophys. Res. Lett. **20**, 739 (1993).
5. V. Y. Trakhtengerts and M. Hayakawa, J. Geophys. Res. **98**, 19205 (1993).
6. T. M. Zaboronkova, A. V. Kostrov, A. V. Kudrin, *et al.*, Zh. Éksp. Teor. Fiz. **102**, 1151 (1992) [Sov. Phys. JETP **75**, 625 (1992)].
7. S. V. Egorov, A. V. Kostrov, and A. V. Tronin, Pis'ma Zh. Éksp. Teor. Fiz. **47**, 86 (1988) [JETP Lett. **47**, 102 (1988)].
8. A. Gulielmi, J. Kangas, and A. Potapov, J. Geophys. Res. **106**, 25847 (2001).

Translated by A. Bagatur'yants

JETP Letters, Vol. 78, No. 9, 2003, pp. 542–547. Translated from Pis'ma v Zhurnal Éksperimental'noĭ i Teoreticheskoĭ Fiziki, Vol. 78, No. 9, 2003, pp. 1030–1035.

Two Scenarios for Phase-Transformation in Disordered Media

V. V. Brazhkin* and A. G. Lyapin

Institute of High-Pressure Physics, Russian Academy of Sciences, Troitsk, Moscow region, 142190 Russia

**e-mail: brazkin@hppi.troitsk.ru*

Received September 24, 2003

The reasons for the existence of various scenarios for structural transformations in disordered condensed media, such as liquids and amorphous substances, where both smeared transformations and sharp first-order transitions may occur, were analyzed. The ratio between the spatial scale of structural correlations and the size of the smallest possible region occupied by a new phase in the matrix of initial modification is the key parameter determining the scenario for equilibrium phase transformations in liquids. In amorphous substances, the experimentally observed transformations occur far from equilibrium, and the possible size of the region occupied by the new phase corresponds to the minimal nucleus size. For some amorphous solids, quantitative analysis of the transformation width was carried out and the main classes of covalent substances, in which the smeared or sharp transitions occur, were revealed. Specific features of the interparticle interactions determining various transformation scenarios are discussed. © *2003 MAIK "Nauka/Interperiodica".*

PACS numbers: 64.70.-p; 61.43.-j; 61.20.-p; 62.50.+p

1. INTRODUCTION

To date, first-order phase transitions induced in crystals by external parameters have been studied rather well both theoretically and experimentally. By contrast, investigation of the pressure- and temperature-induced phase transformations in disordered condensed media—liquids and amorphous solids—is only at the early stage [1].

Experimental data on the phase (structural) transformations under pressure in liquids and amorphous solids are few in number [1]. For the majority of studied liquids (Cs, Rb, Te, Sn, Si, As_2Te_3, and Ge–Te) and many amorphous substances (*a*-SiO_2, *a*-GeO_2, *a*-C), the transformations are smeared in pressure and temperature and identified by a significant short-range structural rearrangement [1]. At the same time, sharp transitions formally close to the first-order phase transition are observed in liquid phosphorus [1, 2] and in amorphous *a*-H_2O or *a*-D_2O ice [1, 3]. Moreover, in the course of these transformations, the states of a macroscopic mixture of two phases with a well-defined interfaces were observed [4, 5]. Sharp transitions probably also occur in the Y_2O_3–Al_2O_3 melt, supercooled water, and supercooled Si and Ge melts [1] and, possibly, in some amorphous phases, e.g., in *a*-$Zn_{41}Sb_{59}$ [6].

The theoretical consideration of phase transformations in liquids and glasses mainly amounts to using empirical approaches based on the models of "regular solution" type [7–9]. In these models, all transformations are first-order phase transitions terminated at the critical points upon rise in temperature. The interrelation between the phase transitions in liquids and a certain microscopic type of interparticle interaction can be found in only a few of approaches [10]. Analysis of the equilibrium between two different metastable modifications in amorphous solids has conditional character, whereas real transformation is a kinetic phenomenon that is observed near the stability boundary (spinodal) of the initial amorphous phase and accompanied by various relaxational phenomena of an unusual nature [1].

The reasons for the existence of various transformation types (smeared and sharp) in disordered media have almost not been considered so far. With liquids, it is believed that the smeared transitions should become sharp upon lowering temperature [7–9]. In [11], various scenarios for transitions in melts were related to the amorphous or crystalline type of local ordering in liquid. Although the transition types in amorphous substances were reproduced by computer simulation using various interparticle potentials [12], the relevance of these potentials to real amorphous solids remains to be clarified.

In this work, the scenarios for the transformations accompanied by the sharp and smeared changes in the short-range order in liquids and amorphous solids are analyzed. It will be shown that the transition type is determined by the ratio of the size of the smallest possible region with the new short order to the correlation length of the medium-range order in a disordered medium. For liquids, the smallest region is given by the smallest fluctuation cluster that reduces energy of the system in the stability region of the initial modification, whereas, for the amorphous state, this region is determined by the critical nucleus of new modification in the metastable region of the initial phase.

0021-3640/03/7809-0542$24.00

2. PHASE TRANSFORMATIONS IN DISORDERED CONDENSED MEDIA. GENERAL

In the first-order phase transition, the chemical potential of a mixture of phases exceeds the corresponding value for the stable phase at all pressures and temperatures, except in the equilibrium curve. However, if the sizes of phase regions are small, one should include the interphase surface energy (conditional mixing energy) and the mixing entropy (provided that the different states can arise during the experimental times). The surface energy increases the chemical potential of the mixture, while the mixing entropy reduces it. It is then conceived that, if there is a structural transformation between different phases, the transition at sufficiently low temperatures should be sharp (of the first kind); as the temperature increases, the transition curve may terminate at the critical, triple, or tricritical point, or at the point of stability loss for one of the phases [1, 7, 13].

It is generally agreed that the aforementioned refers equally to the disordered condensed media. However, one of the main properties of the disordered state that distinguishes it from crystal, namely, *the structural inhomogeneity on the nanometer scale that is smaller than the characteristic correlation length d_{cor} of the medium order in disordered systems*, is not taken into account in the above approach. This inhomogeneity (Fig. 1a) in a disordered medium leads to the dispersion of geometric, dynamic, and energy characteristics of its characteristic structural units (in what follows, clusters) under the condition that the cluster size r_{cl} is smaller than d_{cor} (Fig. 1b).

It follows that, contrary to crystals, the main properties (energy, Gibbs energy, volume, etc., taken per one atom) of small clusters constituting the disordered system coincide with the macroscopic properties of the phase only if $r_{cl} > d_{cor}$ (Fig. 1b). If the size of the region with new short order is smaller than the correlation length d_{cor} in the initial disordered phase, then, due to the energy dispersion of individual clusters, the chemical potential of the initial modification can be reduced because of the appearance of clusters of a new Phase (Fig. 2a), and a cluster mixture with different short orders becomes the most favorable state in a certain transition region at any temperature (Fig. 2). In fact, this corresponds to the effective negative surface energy of the new phase, although the surface energy of an individual cluster, clearly, remains positive. For the existing empirical models, this situation means that the mixing energy in the Aptecar and Rapoport models [7, 8] or the frustration energy in the Tanaka model [9] is negative.

In this work, we do not consider the intrinsic transformation mechanism, which, evidently, is associated with the appearance of soft modes in the initial disordered phase. *But it should be emphasized that the minimal size of the region with new short order is precisely that which corresponds to the characteristic localization radius of soft modes.*

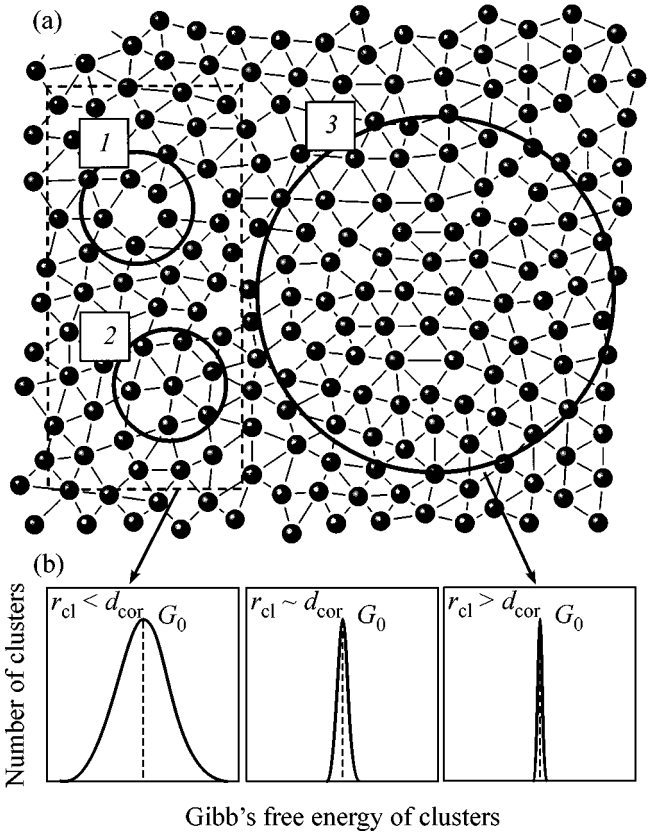

Fig. 1. (a) Model two-dimensional atomic amorphous network, where regions *1* and *2* illustrate the case of small clusters ($r_{cl} < d_{cor}$) with a wide scatter of cluster characteristics, and region *3* corresponds to a large cluster ($r_{cl} > d_{cor}$). (b) As the ratio between r_{cl} and d_{cor} changes, the distribution of cluster Gibbs energies (per atom) changes from broad in the case of $r_{cl} < d_{cor}$ to narrow, typical of crystals, in the case of $r_{cl} > d_{cor}$.

Therefore, the nanometer-scale dispersion of characteristics and the ratio between r_{cl} and d_{cor} are crucial in determining the possible scenario for phase transformation. If $r_{cl} < d_{cor}$, the phase transformation is smeared at any temperature. Conversely, the condition $r_{cl} > d_{cor}$ corresponds to a change from the smeared transformation scenario to the first-order phase transition, for which the transition curve will terminate at the critical point, in accordance with [7–9].

3. LIQUIDS

All the above refers in full measure to liquids as ergodic systems in which, by definition, various cluster states are accessible theoretically. In this case, the minimal cluster size r_{cl} in the region of structural transformation can be estimated from the comparison of a

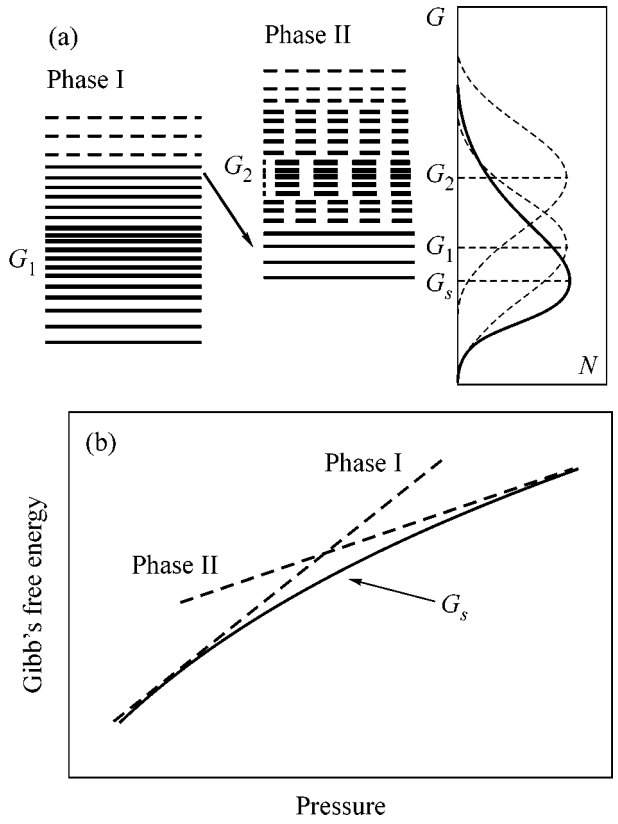

Fig. 2. (a) Diagram of Gibbs free energies in the region of transition from phase I to phase II for clusters in two amorphous phases with a broad distribution ($r_{cl} < d_{cor}$). On the whole, phase I is more stable, but its clusters with high-lying levels transform into the low-lying clusters of phase II (dashed lines correspond to the unfilled states), with the distribution center-of-gravity in the mixture of phases G_s lying lower than the characteristic Gibbs free energies of both phases I and II (G_1 and G_2). (b) The pressure dependence of Gibbs free energy of the system in the course of transformation (solid line) is smoothed and the corresponding curve lies lower than for the pure phases (dashed lines).

decrease in chemical potential as a result of cluster energy spectrum rearrangement with an increase by virtue of the local surface energy at the boundary of the regions with different short orders:

$$\frac{r_{cl}^3 \Delta G(r_{cl})}{a^3} = C_1 \sigma(r_{cl}) r_{cl}^2, \quad (1)$$

where $\Delta G(r_{cl})$ is the Gibbs energy distribution width for the clusters of a given size (Fig. 1b), $\sigma(r_{cl})$ is the surface energy of a typical cluster, a is the interatomic distance, and C_1 is a dimensionless numerical constant. The quantity σ can be estimated as [14]

$$\sigma = C_2 \frac{\varepsilon}{a^2} \frac{\Delta V}{V}, \quad (2)$$

where C_2 is the numerical constant, ε is the binding energy per atom, and $\Delta V/V$ is the relative jump in volume upon changing short-range order. The quantity ΔG is associated with the fluctuation of angles and bond lengths in cluster [15]:

$$\Delta G = C_3 \varepsilon \frac{\delta\varphi}{\varphi}, \quad (3)$$

where C_3 is the numerical constant and $\delta\varphi/\varphi$ is the characteristic mean fluctuation of geometric parameters in the amorphous network. From Eqs. (1)–(3) one has

$$r_{cl} = C_4 \frac{a(\Delta V/V)}{\delta\varphi/\varphi}, \quad (4)$$

where C_4 is the combination of numerical constants. At the same time, the correlation length d_{cor} at which the structural order is lost due to static fluctuations can be estimated as

$$d_{cor} = \frac{C_5 a}{\delta\varphi/\varphi}, \quad (5)$$

where C_5 is the numerical constant (on the order of unity) determined by the network geometry. From Eqs. (4) and (5), one gets, instead of $r_{cl} > d_{cor}$, the following condition for the first-order phase transition

$$\Delta V/V \geq C_5/C_4. \quad (6)$$

With such a simplified approach, phase transition in liquid is of the first kind if the relative jump in volume upon the transformation exceeds a certain critical value. In reality, the volume jumps achieve 10–60% in liquids where the first-order transitions are observed (P, supercooled H_2O, Si, Ge, and, possibly, C) [1]. Volume jumps as large as these are associated with a radical change in the structure of short-range order. Melts with crystal-like structure in the Patashinskii model [11] are characterized by the narrow ΔG distribution and, respectively, large C_4 constant. As a result, these melts can undergo first-order phase transitions with a small jump in volume. Such a situation occurs, for example, in liquid crystals and ionic melts of organic salts [1, 14].

4. AMORPHOUS SUBSTANCES

In amorphous substances, the transformations during experimental times occur far from the conditions of equilibrium curve. The new amorphous phase is formed through the appearance of its nuclei, but without their noticeable growth, so that the transition kinetics is determined by the nucleation scenario. The dispersion of structural and energy characteristics of clusters in the amorphous phase should cause a broad distribution of nucleation energy, but only if the size r_{min} of critical nucleus is smaller than the region of structural correlations in the amorphous substance [16], i.e., if $r_{min} < d_{cor}$ (Fig. 1). At $r_{min} > d_{cor}$, the amorphous phase can be considered as a homogeneous continuous medium, and the

nucleation of the new phase proceeds homogeneously and simultaneously at the same external parameters. In this case, the transformation kinetics between amorphous modifications will be the same as in the case of conditional first-order phase transitions. In other words, when analyzing the transformations in amorphous state, one should consider the smallest nuclei of the new phase in a deep metastability region of the primary modification, rather than the smallest clusters of new phase in the stability region of the initial phase. Therefore, for the transformations far from equilibrium in amorphous materials, the transition scenario is governed by the ratio between r_{min} and d_{cor}.

The size of critical nucleus can be estimated analogously to Eq. (1):

$$\Delta p \Delta V r_{min}^3 / V = C_6 \sigma r_{min}^2, \quad (7)$$

where the transformation occurs far from equilibrium, so that the distribution width ΔG is replaced by the supersaturation of metastable phase with respect to the Gibbs energy, $\Delta P \Delta V$, where ΔP is the difference between the transformation pressure and the pressure of conditional equilibrium transition, and it is also taken into account that $a^3 \sim V$. Then,

$$r_{min} = \frac{C_6 \sigma}{\Delta P(\Delta V)/V}. \quad (8)$$

The surface tension at the interface can be estimated as $\sigma \sim B_{eff} a(\Delta V/V)$, where the effective modulus B_{eff} is a combination of the bulk and shear moduli [14]. By inserting this estimate into Eq. (8), one obtains

$$r_{min} \sim a B_{eff}/\Delta P. \quad (9)$$

The structural correlation length in amorphous state, as a rule, varies only slightly from substance to substance and extends over five to eight coordination spheres, i.e., equals 15–25 Å [15]. At the same time, the critical size of the nucleus of new amorphous modification can strongly differ for different substances. The estimates of the minimal nucleus size for the transformations in the amorphous states of three most typical substances are given in the table. The estimates of r_{min} for a-SiO_2 are in good agreement with the results of molecular dynamics simulations [19, 20] and are evidence of a wide transition. For amorphous ice, the size of critical nucleus is comparable with the region of structural correlation in the initial amorphous phase, as a result of which the *lda–hda* transformation is sharp and corresponds to the first-order phase transition. The case of GeO_2 is intermediate. A comparison of the data for a-SiO_2, a-GeO_2, and a-H_2O (Fig. 3) shows that there is inverse correlation between the size of critical nucleus (table) and the relative transition width.

Estimates of the radii of minimal-sized nuclei for some transformations between amorphous phases (Eq. (9)) using experimental data for ΔP, and estimates of B_{eff} using formula $B_{eff} = (B + G)/2$, where B is the bulk modulus and G is the shear modulus

Substance	ΔP (Gpa)	B (Gpa)	G (Gpa)	r_{min} (Å)
H_2O [1, 3]	0.5–1	8–12	4–6	20–40
GeO_2 [17]	~10	40–150	20–50	10–20
SiO_2 [1, 18]	~20	50–150	30–60	5–10

5. ROLE OF INTERPARTICLE INTERACTION

For the model pair potential of collapsing hard spheres [10] (Fig. 4), the existence of critical parameters for the first-order phase transition can be understood from simple considerations. The potential energy of the system is the sum over all particles $E(V) = \int U(r)g(r)r^2 dr$, where $U(r)$ is the effective pair potential and $g(r)$ is the structural correlation function depending implicitly on volume. In the ordered system of particles, the volume dependences of energy and potential are analogous; i.e., the corresponding curve for energy has an anomalous shoulder, indicating that first-order phase transition with a jump in volume can occur in the system. In the disordered system, the feature in the energy curve is retained only if the width of anomalous region in the potential exceeds the smearing of correlation function in the disordered system (Figs. 4a–4c), otherwise (Figs. 4d–4f) the first-order phase transition does not occur. Note that there is a pictorial interrelation between the condition $r_{cl} > d_{cor}$ and the relation

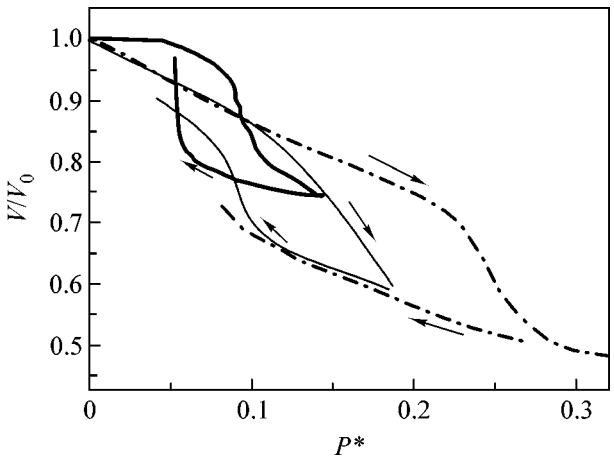

Fig. 3. Dependences of the relative volume on the dimensionless effective pressure P^* for the direct and reverse transformations between the amorphous phases of (solid line) H_2O [21], (thin line) GeO_2 [17], and (dot-and-dash line) SiO_2 [18, 19]. Curves taken from [19] and [21] are smoothed off. P^* was recalculated from usual pressure by the renormalization to the current bulk modulus $B(P)$ of the system.

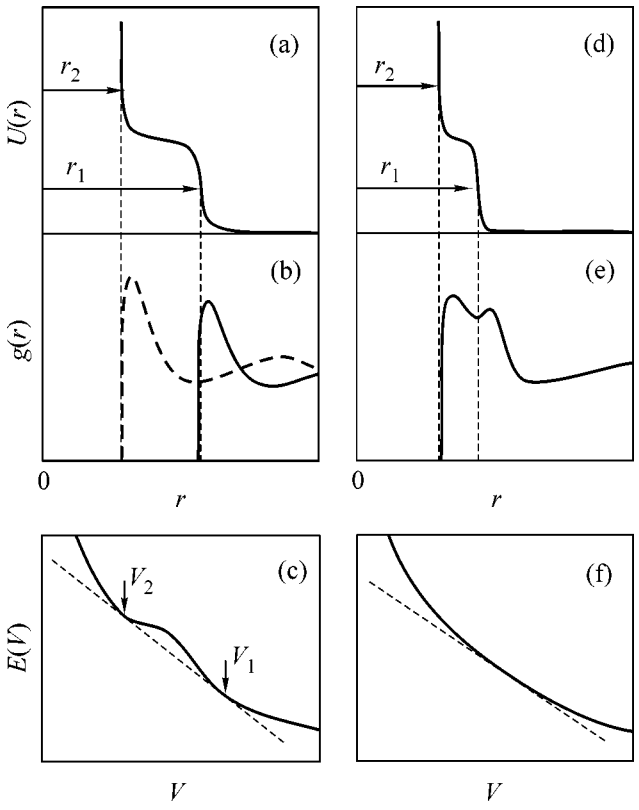

Fig. 4. (a) Interparticle potential, (b) pair correlation function, and (c) volume dependence of energy for the system of collapsing hard spheres with a broad step in the potential; first-order phase transition takes place. The solid and dashed lines in (b) correspond, respectively, to the states before and after the phase transition. Panels (d), (e), and (f) illustrate analogous dependences for the system of collapsing hard spheres with a narrow step in the potential, for which the transformation is smeared. The correlation function (e) corresponds to the state with intermediate ordering.

between the smearing of correlation function and the step magnitude in the interparticle potential. The step width in $g(r)$ is inversely proportional to the correlation length d_{cor}, while a decrease in the anomaly magnitude in the pair potential corresponds to a decrease in the surface tension and, hence, to lower r_{cl} values. The presence of critical values for the features in the interparticle potential, which is necessary for a sharp transition, radically differentiates the disordered systems from crystals, where even small features in the potential can lead to a first-order phase transition.

The above analysis clarifies the results of the computer simulation carried out in [12]. The sharp phase transition in a disordered system with strong interparticle attraction [12] corresponds to a large critical nucleus of new phase. Conversely, a weak attractive potential [12] corresponds to the low effective surface energy and small (one or two coordination spheres) critical nucleus.

The reason why the transformation scenarios in *a*-SiO_2 and *a*-GeO_2, on the one hand, and in *a*-H_2O, on the other, are different is due to the fact that the interparticle interactions in these systems have different character. In *a*-SiO_2 and *a*-GeO_2 glasses, the main structure-forming elements (Si(Ge)O_4 tetrahedra) are bonded to each other via weaker bending covalent forces and weak van der Waals forces, whereas amorphous ice can be considered as an oxygen-based atomic network without a hierarchy of strong and weak interactions [1, 3, 20]. The differences in the character of interaction and in the degree of connectivity in amorphous networks of *a*-SiO_2 and *a*-H_2O can be analyzed in terms of rigidity percolation [20, 22]. The effective coordination number for the covalent bonds in *a*-SiO_2 is smaller than the rigidity percolation threshold $Z = 2.4$, whereas, for the structure-forming oxygen network in *a*-H_2O, $Z = 4$ [3], evidencing the topological rigidity of amorphous ice.

Based on the above analysis, one can predict the character of hypothetical phase transitions in various covalent amorphous substances. For example, the low-temperature transformations in chalcogenide glasses, such as Se and S ($Z = 2$), are expected to be strongly smeared in pressure, whereas the transitions in tetrahedral amorphous semiconductors, such as *a*-Si and *A*-Ge ($Z = 4$), should be sharp at temperatures below the crystallization temperature of amorphous phases. Recent results of computer simulation of *a*-Si, *a*-Ge, and *a*-$GeSe_2$ [23, 24] indirectly confirm this prediction.

We are grateful to S.M. Stishov, V.N. Ryzhov, S.V. Popova, E.G. Ponyatovskiĭ, P. Keliris, and Y. Katayama for discussion of the problem. This work was supported by the Russian Foundation for Basic Research (project nos. 01-02-16557 and 02-02-16298), INTAS (grant no. 00-807), and JSPS.

REFERENCES

1. *New Kinds of Phase Transitions: Transformations in Disordered Substances*, Ed. by V. V. Brazhkin, S. V. Buldyrev, V. N. Ryzhov, and H. E. Stanley (Kluwer, Dordrecht, 2002), NATO Sci. Ser. 2: Math., Phys. Chem., Vol. 81.
2. Y. Katayama, T. Mizutani, W. Utsumi, *et al.*, Nature **403**, 170 (2000).
3. O. Mishima and H. E. Stanley, Nature **396**, 329 (1998).
4. Y. Katayama, *Gordon Research Conference, Research at High Pressure, Meriden, NH, USA, 2002*, private communication.
5. O. Mishima and Y. Suzuki, Nature **419**, 599 (2002).
6. V. E. Antonov, O. I. Barkalov, V. K. Fedotov, *et al.*, Phys. Rev. B **62**, 3130 (2000).
7. I. L. Aptekar', Sov. Phys. Dokl. **24**, 993 (1979).
8. E. Rapoport, J. Chem. Phys. **46**, 2891 (1967); J. Chem. Phys. **48**, 1433 (1968).
9. H. Tanaka, Phys. Rev. E **62**, 6968 (2000).

10. V. N. Ryzhov and S. M. Stishov, Phys. Rev. E **67**, 010201 (2003).
11. A. Z. Patashinskii and M. A. Ratner, J. Chem. Phys. **106**, 7249 (1997).
12. E. A. Jagla, Phys. Rev. E **63**, 061509 (2001).
13. E. G. Ponyatovskiĭ, Pis'ma Zh. Éksp. Teor. Fiz. **66**, 260 (1997) [JETP Lett. **66**, 281 (1997)].
14. A. Ubbelohde, *The Molten State of Matter* (Wiley, New York, 1978).
15. R. Zallen, *The Physics of Amorphous Solids* (Wiley, New York, 1998).
16. V. G. Karpov and D. W. Oxtoby, Phys. Rev. B **54**, 9734 (1996).
17. O. B. Tsiok, V. V. Brazhkin, A. G. Lyapin, and L. G. Khvostantsev, Phys. Rev. Lett. **80**, 999 (1998).
18. C. Zha, R. J. Hemley, H. Mao, *et al.*, Phys. Rev. B **50**, 13105 (1994).
19. D. J. Lacks, Phys. Rev. Lett. **80**, 5385 (1998).
20. K. Trachenko and M. T. Dove, Phys. Rev. B **67**, 064107 (2003).
21. V. Stal'gorova, E. L. Gromnitskaya, V. V. Brazhkin, and A. G. Lyapin, Pis'ma Zh. Éksp. Teor. Fiz. **69**, 653 (1999) [JETP Lett. **69**, 694 (1999)].
22. H. He and M. F. Thorpe, Phys. Rev. Lett. **54**, 2107 (1985).
23. M. Duradurdu and D. A. Drabold, Phys. Rev. B **64**, 014101 (2001).
24. M. Duradurdu and D. A. Drabold, Phys. Rev. B **65**, 104208 (2002).

Translated by V. Sakun

JETP Letters, Vol. 78, No. 9, 2003, pp. 548–550. Translated from Pis'ma v Zhurnal Éksperimental'noĭ i Teoreticheskoĭ Fiziki, Vol. 78, No. 9, 2003, pp. 1036–1038.

Influence of Zero-Point Anomalies in the Electron Density of States of Electrodes on the Inelastic Tunneling Spectrum

A. I. Khachaturov

Galkin Donetsk Physicotechnical Institute, National Academy of Sciences of Ukraine, Donetsk, 83114 Ukraine
e-mail: khach@sts.dipt.donetsk.ua

Received August 20, 2003

It is shown that a minimum in the electron density of states near the Fermi surface of one of the electrodes shifts the peaks in inelastic tunneling spectrum toward higher voltages. The shift depends on the correlation parameter and increases with temperature. It is argued that the observation of the shift in the local singularities of inelastic tunneling, in conjunction with the presence of large-scale zero-point anomaly in the differential conductivity, can serve as a firm evidence of the presence of the corresponding singularity in the electron density of metal oxides and magnetoresistive materials. © *2003 MAIK "Nauka/Interperiodica".*

PACS numbers: 73.40.Gk

The possible manifestation of zero-point root singularity in the differential conductivity $\sigma(V)$ of tunneling contacts metal–disordered material was predicted by Altshuler and Aronov in [1]. The detailed experimental studies carried out for amorphous $Ge_{1-x}Au_x$ alloys [2], bismuth films [3], and disordered aluminum films [4] provide strong evidence for the fact that a minimum in the electron density of states of a disordered electrode situated in close vicinity of the metal–insulator junction manifests itself as a zero-point root anomaly in the differential tunneling conductivity

$$\sigma(V) = \sigma_0(1 + \alpha\sqrt{|V|}). \quad (1)$$

Because of this, when the authors of [5] found that the tunneling conductivity of metal oxides, which had lost their superconducting properties for technological reasons, increased proportionally to the root of *V*, they invoked electron–electron interaction to explain this fact.

However, the situation for metal oxides is complicated by the fact that the root singularity is not the only zero-point anomaly in the tunneling conductivity. The linear dependence of conductivity $\sigma(V)$ on the V magnitude is observed in experiments with metal oxides much more frequently (see, e.g., [6, 7] and references therein):

$$\sigma(V) = \sigma_0(1 + \beta|V|). \quad (2)$$

In [8], it was suggested that both these effects have the common nature. The authors of that work are of the opinion that the power of bias applied to the junction can take any value in the interval from 0.5 to 1.0, depending on the degree of disorder. The same approach to the interpretation of such phenomena in tunneling conductivity of magnetoresistive materials was used in [9].

As a result of this, it should be noted that the presence of a zero-point singularity in the experimental curve by no means gives evidence for the presence of the corresponding anomaly in the density of states $N(E)$ of the substance of interest. Contrary to what is stated in [9], the differential conductivity is not a direct measure of the density of states in electrodes, because other factors can also have an appreciable effect on it. At present, there are a number of mechanisms that can explain both root and linear dependences for $\sigma(V)$ under rather trustworthy assumptions [6, 7].

At first glance, the nature of zero-point anomalies in the tunneling characteristics of metal oxides and magnetoresistive materials cannot be understood without invoking the results of additional nontunneling experiments. It is hoped that the effect predicted in this work can give an unambiguous answer to the question of interest within the framework of only the tunneling experiment.

We now show that the minimum centered at the Fermi level in the density of states of one of the electrodes shifts the positions of local singularities caused by the inelastic interaction of tunneling electrons with local impurities in the barrier. According to [10], the contribution to the tunneling current from the inelastic tunneling channel is

$$J_i(V) \propto \int_{-\infty}^{\infty} N_1(E)N_2(E + e(V - V_0))\,f(E) \times [1 - f(E + e(V - V_0))]dE, \quad (3)$$

where V_0 is the bias on the tunnel junction, $\hbar\omega = eV_0$ is the corresponding excitation energy in the barrier, and $f(E, T)$ is the Fermi–Dirac distribution function (energy E in Eq. (3) and in all subsequent formulas is measured

from the Fermi level of the initial electrode). In common materials, the density of states $N_1(E)$ and $N_2(E)$ are smooth functions that can be taken to be constant,

$$J_i(V) = C\int_{-\infty}^{\infty} N(E) f(E, T)[1 - f(E + e(V - V_0, T))]dE, \quad (4)$$

where C is a constant allowing for various E- and T-independent tunneling parameters. Expression (4) can readily be integrated and, after double differentiation, it gives a sharp peak centered at the bias voltage $V = V_0$ for the second derivative d^2I_i/dV^2 [10].

If the density of states of one of the electrodes is modified by the electron–electron interaction, then, according to [1], the density of states in the integrand in Eq. (4) is a function of E:

$$N(E) = N(0)\left[1 + \left(\left|\frac{E}{\Delta}\right|\right)^{\nu}\right]. \quad (5)$$

In this case, the analytic expression for d^2I_i/dV^2 can hardly be obtained at $T \neq 0$. Nevertheless, it can be calculated numerically:

$$\frac{d^2I_i}{dV^2} = C\int_{-\infty}^{\infty} N(E) f(E, T)\frac{\partial^2}{\partial V^2} f[E + e(V - V_0), T]dE. \quad (6)$$

At $T = 0$, the inelastic channel opens only at voltages V higher than V_0. Because all electrons in a layer of thickness $e(V - V_0)$ can be involved in the inelastic tunneling, the inelastic current is

$$I_i(V) = C\int_{-e(V-V_0)}^{0} N(E)dE$$

$$= C_1N(0)\int_{-e(V-V_0)}^{0}\left[1 + \left|\frac{E}{\Delta}\right|^{\nu}\right]dE \quad (7)$$

$$= C_1\Delta\left[e(V - V_0) + \frac{1}{\nu + 1}\left(\frac{e(V - V_0)}{\Delta}\right)^{\nu+1}\right],$$

where $C_1 = CN(0)$. Thus, the second derivative of inelastic current at $T = 0$ and $V > V_0$ is equal to

$$\frac{d^2I_i}{dV^2} = C_1\nu\frac{e^{\nu+1}}{\Delta^{\nu}}(V - V_0)^{\nu-1}. \quad (8)$$

The results of our calculations with $\nu = 1/2$, $\Delta = 0.01$ meV, and $V_0 = 100$ meV are presented in Fig. 1. At zero temperature and biases lower than V_0, the inelastic current is zero; at $V = V_0$ it undergoes infinite jump; and at $V > V_0$ it decreases following the law $d^2I_i/dV^2 = C_1e^{3/2}/2\sqrt{\Delta(V - V_0)}$ (curve *1* in Fig. 1). Curves *2*, *3*, and *4* were calculated by formula (6) for temperatures of 20, 40, and 77 K, respectively. The main feature distinguishing the behavior of these curves from the inelastic curves studied by Lambe and Jaklevic [10] is that, in our case, the position of the maximum in the curve for the V dependence of the second derivative of inelastic current with respect to voltage d^2I_i/dV^2 coincides with the threshold voltage only at $T = 0$. Whereas in [10] the temperature only smeared out the peak while the peak position did not change, in our case the peak not only broadens and decreases in amplitude but also shifts its maximum V_{max} to higher voltages. At a high (e.g., nitrogen) temperature, the peak shift $V_{sh} = V_{max} - V_0$ can be large enough. For instance, the maximal shift of the curves calculated for $\Delta = 10$ meV, is $V_{sh} = 8$ meV (curve *4* in Fig. 1). Note also that, as expected, the behavior of all curves at high voltages $eV \gg kT$ coincides with the behavior of the zero-temperature curve.

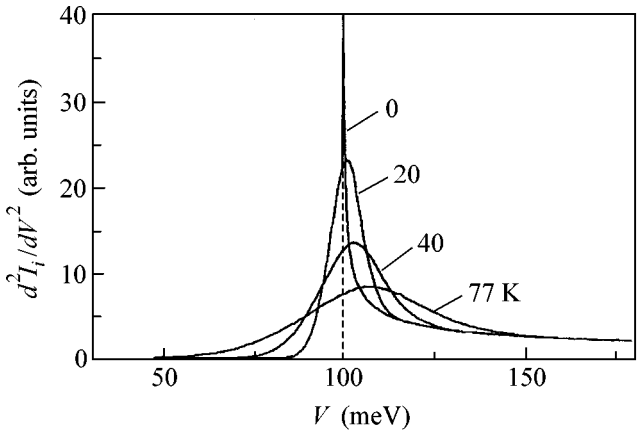

Fig. 1. Second derivatives d^2I_i/dV^2 of the inelastic tunneling current in the presence of root singularity $\nu = 1/2$ in the electron density of states of one of the electrodes. The parameter $\Delta = 10$ meV and the threshold voltage $V_0 = 100$ meV. Curves were calculated for temperatures indicated in the figure.

For $\nu = 1$, the zero-temperature behavior of the V dependence of d^2I_i/dV^2 is different from the case $\nu = 1/2$ in that, at $V > V_0$, the derivative is a constant value $d^2I_i/dV^2 = C_1e^2/\Delta$ (horizontal line *1* in Fig. 2). The curves calculated for $\Delta = 0.02$ meV and temperatures of 30, 50, and 77 K (curves *2*, *3*, *4* in Fig. 2) show that the shifts V_{sh} in this case are larger than in Fig. 1.

It is well known that the gap Δ_S in the single-particle density of states of superconducting electrodes shifts the spectroscopic features to higher voltages by a value equal to half of the bandgap: $V_{sh}^S = \Delta_S/2e$. Because of this, the assumption that a minimum in the density of states can also have a sizable effect on the positions of singularities in the inelastic tunneling spectra seems to be quite natural. We emphasize, however, that, contrary to the superconducting electrodes, for which the shift

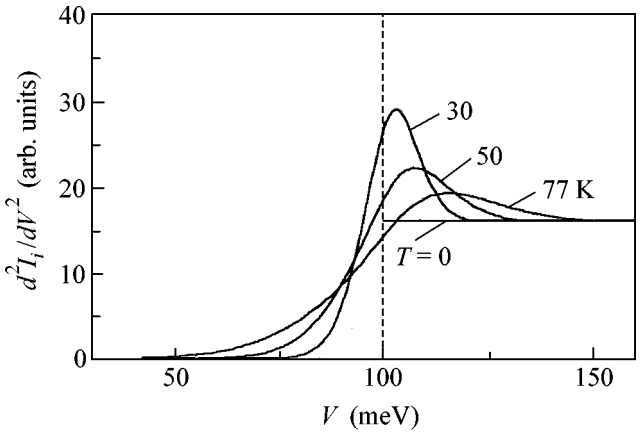

Fig. 2. Second derivatives d^2I_i/dV^2 of the inelastic tunneling current in the presence of linear singularity $\nu = 1$ in the electron density of states of one of the electrodes. The parameter $\Delta = 20$ meV and the threshold voltage $V_0 = 100$ meV.

V_{sh}^S can also be observed at zero temperatures, the effect predicted in this work is observed only at nonzero temperatures. There must be a certain relationship between the correlation parameter Δ, which can be estimated from the overall shape of the experimental $\sigma(V)$ curve, the temperature T, and the shift V_{sh}. The observation of this relation in the experiment would provide strong evidence that the presence of zero-point anomalies in the differential conductivity of tunneling contacts based on metal oxides and magnetoresistive materials is, indeed, indicative of the presence of corresponding singularity in the electron density of states.

I am grateful to V.M. Svistunov and M.A. Belogolovskiĭ for useful remarks.

REFERENCES

1. B. L. Altshuler and A. G. Aronov, Solid State Commun. **30**, 1155 (1979).
2. W. L. McMillan and J. Mochel, Phys. Rev. Lett. **46**, 556 (1981).
3. V. N. Lutskiĭ, A. S. Rylik, and A. K. Savchenko, Pis'ma Zh. Éksp. Teor. Fiz. **41**, 134 (1985) [JETP Lett. **41**, 163 (1985)].
4. M. E. Gershenzon, V. N. Gubin, and M. I. Faleĭ, Zh. Éksp. Teor. Fiz. **90**, 2196 (1986) [Sov. Phys. JETP **63**, 1287 (1986)].
5. V. M. Svistunov, M. A. Belogolovskii, and A. I. Khachaturov, in *Progress in High Temperature Superconductivity* (World Sci., Singapore, 1991), Vol. 32, p. 111.
6. J. R. Kirtley, S. Washburn, and D. J. Scalapino, Phys. Rev. B **45**, 336 (1992).
7. M. Grajcar, A. Plecenik, P. Seidel, *et al.*, Phys. Rev. B **55**, 11738 (1997).
8. H. Srikanth, K. P. Rajeev, G. V. Shivashankar, and A. K. Raychaudhuri, Physica C (Amsterdam) **195**, 87 (1992).
9. Ashutosh Tiwari and K. P. Rajeev, Phys. Rev. B **60**, 10591 (1999).
10. J. Lambe and R. C. Jaklevic, Phys. Rev. **165**, 821 (1968).

Translated by V. Sakun

JETP Letters, Vol. 78, No. 9, 2003, pp. 551–554. Translated from Pis'ma v Zhurnal Éksperimental'noĭ i Teoreticheskoĭ Fiziki, Vol. 78, No. 9, 2003, pp. 1039–1042.

Long-Range Magnetic Order in Quasi-One-Dimensional $NaCrSi_2O_6$ and $NaCrGe_2O_6$ Metal Oxides

A. N. Vasil'ev[1], O. L. Ignatchik[1], A. N. Sokolov[1], Z. Hiroi[2], M. Isobe[2], and Y. Ueda[2]

[1] *Moscow State University, Moscow, 119992 Russia*

[2] *Institute for Solid State Physics, Kashiwa, Chiba 277-8581, University, Tokyo, Japan*

Received September 22, 2003

Formation of a long-range magnetic order is observed at low temperatures in $NaCrSi_2O_6$ and $NaCrGe_2O_6$ quasi-one-dimensional metal oxide compounds with a pyroxene structure. The first of these compounds, $NaCrSi_2O_6$, is an antiferromagnet with the Néel temperature $T_N = 3$ K, while the second, $NaCrGe_2O_6$, is a ferromagnet with the Curie temperature $T_C = 6$ K. From the measurements of magnetization and specific heat of these compounds, the main parameters of their magnetic subsystems are determined. In $NaCrSi_2O_6$, a spin-flip transition is observed. A change in the type of magnetic order that accompanies the replacement of Si by Ge can be attributed to a change in the parameters of the competing direct antiferromagnetic Cr–Cr and indirect ferromagnetic Cr–O–Cr interactions in isolated chains of CrO_6 octahedra. © *2003 MAIK "Nauka/Interperiodica".*

PACS numbers: 75.10.Pq; 75.50.Ee; 75.50.Cc; 65.40.Ba; 75.60.Ej

Quasi-one-dimensional transition-metal-based metal oxides are of interest, because these materials can at low temperatures exhibit exotic ground states whose properties are determined by the magnetic interaction in a single preferred direction. In such systems, a long-range magnetic order is absent even at absolute zero, while a decrease in temperature is only accompanied by the enhancement of correlations in the arrangement of magnetic moments in a chain.

Magnetic properties of spin chains with integer and half-integer spins are basically different. The spectrum of magnetic excitations of a half-integer spin chain is gapless [1], while the spectrum of magnetic excitations of an integer spin chain contains such a gap [2]. Correspondingly, the magnetic susceptibility of a half-integer spin chain is finite at low temperatures while the magnetic susceptibility of an integer spin chain is zero.

A quasi-one-dimensional system is capable of forming a long-range magnetic order if the interchain interactions are taken into account. The type of magnetic order, i.e., ferromagnetic or antiferromagnetic, is determined by the signs of all magnetic interactions. As a rule, quasi-one-dimensional metal oxide magnets exhibit an antiferromagnetic ground state at low temperatures [3, 4].

In $LiVGe_2O_6$, which is a quasi-one-dimensional metal oxide with a pyroxene structure, the antiferromagnetic state is achieved at $T_N = 22$ K [5–9]. In titanium-based pyroxenes, $LiTiSi_2O_6$ and $NaTiSi_2O_6$, a singlet ground state is realized at $T_S = 230$ and 210 K, respectively, owing to the dimerization of the chains of TiO_6 octahedra [10]. The magnetic subsystems of all V^{3+}- and Ti^{3+}-based compounds studied exhibit pronounced quasi-one-dimensionality.

In this paper, we report the synthesis of $NaCrSi_2O_6$ and $NaCrGe_2O_6$ metal oxides with pyroxene structure and their study at low temperatures, which revealed different types of long-range magnetic order in these materials. Moreover, the magnetic quasi-one-dimensionality of these compounds was found to be strongly suppressed.

The aforementioned compounds were prepared by a solid-state synthesis from stiochiometric mixtures of Na_2CO_3, Cr_2O_3, and SiO_2 (or GeO_2) at a temperature of ~900°C for 24 h, and their single-phase composition was verified by X-ray studies. $NaCrSi_2O_6$ and $NaCrGe_2O_6$ pyroxenes crystallize in the $P2_1/c$ monoclinic structure. At room temperature, the lattice parameters of $NaCrSi_2O_6$ are $a = 0.951(7)$ nm, $b = 0.867(6)$ nm, $c = 0.524(0)$ nm, and $\beta = 107.3(3)°$; the lattice parameters of $NaCrGe_2O_6$ are $a = 0.988(2)$ nm, $b = 0.882(4)$ nm, $c = 0.544(1)$ nm, and $\beta = 107.5(9)°$. The pyroxene structure contains helical chains of edge-shared CrO_6 octahedra, with the common edge passing through the basis and apical O^{2-} oxygen ions. In the pyroxene crystal structure, chromium ions are trivalent and their spin moment is $S = 3/2$. The magnetization of powder samples was measured by a SQUID magnetometer, and the specific heat, by quasi-adiabatic Quantum Design (in the range 0.4–25 K), and Termis (6–250 K) calorimeters.

In $NaCrSi_2O_6$, the signal exhibits a peak at $T_M = 3.6$ K (Fig. 1a), whose behavior resembles the behavior of magnetic susceptibility of a three-dimensional antiferromagnet. However, this peak corresponds only to

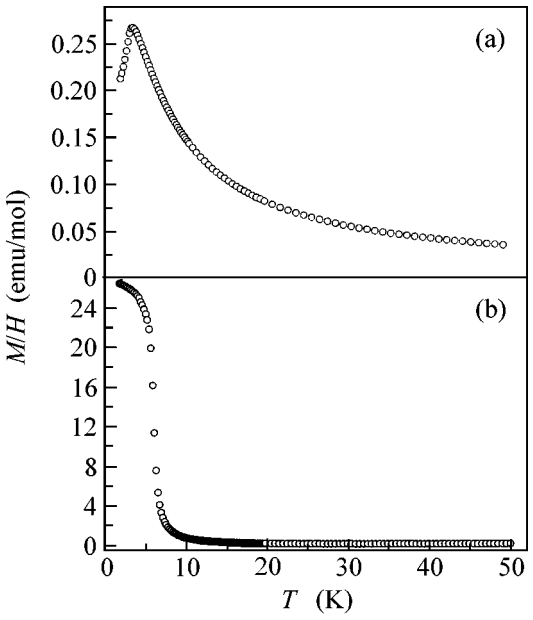

Fig. 1. Temperature dependences of reduced magnetization for (a) $NaCrSi_2O_6$ in a magnetic field of 1000 Oe and (b) $NaCrGe_2O_6$ in a magnetic field of 50 Oe.

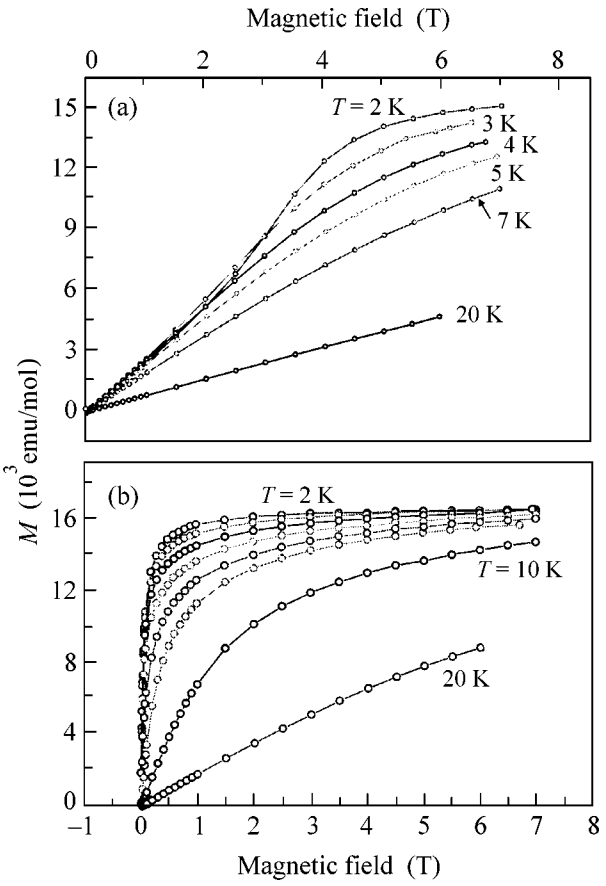

Fig. 2. Field dependences of magnetization for $NaCrSi_2O_6$ and $NaCrGe_2O_6$.

establishing the short-range magnetic order regime, while the three-dimensional ordering occurs at a lower temperature, T_N = 3 K, where a peak is observed in the temperature curve for $d(M/H)/dT$. In the curve obtained for $NaCrGe_2O_6$, one can see a sharp increase in magnetization at T_C = 6K, which is typical of ferromagnets (Fig. 1b).

From the analysis of high-temperature curves, it follows that, for $NaCrSi_2O_6$, the Weiss constant is Θ = –0.3 K, and, for $NaCrGe_2O_6$, Θ = 13 K. The effective magnetic moment of both compounds is $\mu_{eff} = 3.7\mu_B$, which is close to the purely spin moment of trivalent chromium Cr^{3+} (S = 3/2).

The temperature T_M corresponding to the maximum of magnetic susceptibility for a chain with S = 3/2 is related to the intrachain exchange-interaction parameter $J_\parallel$, by the formula $T_M = 0.211J_\parallel$ [11]. For $NaCrSi_2O_6$, this yields $J_\parallel \approx 1$ K. To determine the interchain exchange-interaction parameter $J_\perp$, the following relation is used [12]:

$$J_\perp = T_N/1.28n[\ln(5.8J_\parallel/T_N)]^{1/2},$$

where n = 4 is the coordination number for the interchain interaction. Calculations show that the interchain-interaction parameter $J_\perp \approx 1$ K in $NaCrSi_2O_6$ is virtually equal to the exchange-interaction parameter in a chain. From the data available, it is impossible to determine the sign of exchange interaction between chains. However, by analogy with $LiVGe_2O_6$, which is isostructural with $NaCrSi_2O_6$ [6], one can assume that this exchange has a ferromagnetic character. From the comparison between the Weiss Θ and Néel T_N temperatures in $NaCrSi_2O_6$, it follows that the intrachain and interchain exchange in this compound are close in magnitude and opposite in sign; i.e., the intrachain exchange parameters are antiferromagnetic. In $NaCrGe_2O_6$, the exchange interaction in a chain changes sign as compared to other pyroxenes, i.e., becomes ferromagnetic.

The field dependences of the magnetizations of $NaCrSi_2O_6$ and $NaCrGe_2O_6$ are shown in Fig. 2. They clearly demonstrate the distinction in the behavior of the antiferromagnetically and ferromagnetically ordered pyroxenes. In the antiferromagnetic $NaCrSi_2O_6$, a spin-flip transition is observed at low temperatures, while $NaCrGe_2O_6$ exhibits a behavior typical of ferromagnets. The saturation magnetizations of $NaCrSi_2O_6$ and $NaCrGe_2O_6$ virtually coincide and correspond to the estimate for a purely spin effective magnetic moment.

The temperature dependences of the specific heat of $NaCrSi_2O_6$ and $NaCrGe_2O_6$ are shown in Fig. 3. For these compounds, the specific-heat peaks occur at the antiferromagnetic- and ferromagnetic-transition temperatures, respectively. To separate the magnetic contri-

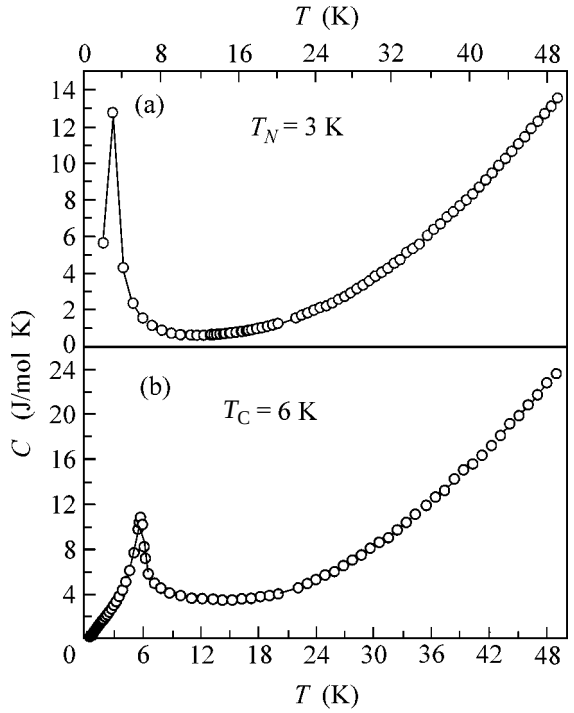

Fig. 3. Temperature dependences of specific heat for $NaCrSi_2O_6$ and $NaCrGe_2O_6$.

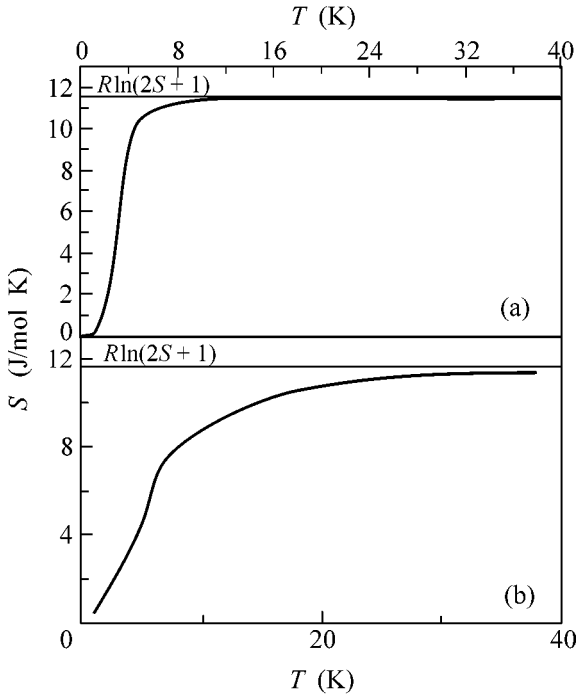

Fig. 4. Temperature dependences of magnetic entropy for $NaCrSi_2O_6$ and $NaCrGe_2O_6$.

bution to specific heat, we used the temperature dependences of specific heat of nonmagnetic isostructural scandium-based pyroxenes $NaScSi_2O_6$ and $NaScGe_2O_6$. The procedure of separating the contributions of the elastic and magnetic subsystems to the specific heat of a solid with the use of data obtained for an isostructural nonmagnetic compound was described in [13]. It includes scaling of the temperature dependences obtained for the entropy of an isostructural compound at $T \gg T_{N,C}$, where the magnetic entropy $R\ln(2S + 1)$ is completely separated. The magnetic entropy calculated in this manner for $NaCrSi_2O_6$ and $NaCrGe_2O_6$ is shown in Fig. 4. One can see that, for the most part, it is separated near the phase-transition temperatures. In this respect, pyroxenes noticeably differ from the isostructural vanadium-based compounds, where the entropy is distributed over a much broader temperature interval.

The antiferromagnetic exchange in the chains of edge-shared CrO_6 octahedra occurs owing to the direct overlap of chromium t_{2g} orbitals. This exchange rapidly weakens as the Cr–Cr distance increases. At the same time, a Cr–O–Cr ferromagnetic superexchange is likely to be also realized in the chains owing to a weak overlap between the chromium t_{2g} orbitals and oxygen p orbitals. If the interchain interaction is ferromagnetic, the competition between the direct exchange and the superexchange determines the type of three-dimensional magnetic ordering. The replacement of Si^{4+} (atomic radius in tetrahedral environment is 40 nm) by Ge^{4+} (atomic radius in tetrahedral environment is 53 nm) leads to a decrease in the direct overlap between the chromium t_{2g} orbitals as a result of the increase in the lattice parameters of $NaCrGe_2O_6$, as compared to $NaCrSi_2O_6$. In this situation, the indirect exchange predominates and, in $NaCrGe_2O_6$, unlike all other pyroxenes studied [5–10], a ferromagnetic ground state is realized.

Thus, magnetic and thermal studies of $NaCrSi_2O_6$ and $NaCrGe_2O_6$ point to such a strong decrease in the parameters of magnetic interaction in the chains that the interchain exchange starts to play the decisive role in the formation of a long-range magnetic order. This kind of relationship between the intrachain and interchain exchange-interaction parameters in the pyroxenes under study, in fact, places them beyond the class of low-dimensional compounds, which is another unexpected result of this study.

We are grateful to E.A. Popova, R.Z. Levitin, and D.I. Khomskiĭ for useful discussions. The work of the Russian group was supported by the Russian Foundation for Basic Research (project no. 03-02-16108).

REFERENCES

1. H. A. Bethe, Z. Phys. **71**, 205 (1931).
2. F. D. M. Haldane, Phys. Lett. A **93A**, 463 (1983).

3. A. N. Vasil'ev, L. A. Ponomarenko, A. I. Smirnov, *et al.*, Phys. Rev. B **60**, 3021 (1999).
4. A. N. Vasil'ev, L. A. Ponomarenko, H. Manaka, *et al.*, Phys. Rev. B **64**, 024419 (2001).
5. P. Millet, F. Mila, F. C. Zhang, *et al.*, Phys. Rev. Lett. **83**, 4176 (1999).
6. J. L. Gavilano, S. Mushkolaj, H. R. Ott, *et al.*, Phys. Rev. Lett. **85**, 409 (2000).
7. M. D. Lumsden, G. E. Granroth, D. Mandrus, *et al.*, Phys. Rev. B **62**, R9244 (2000).
8. J. Lou, T. Xiang, and Z. Su, Phys. Rev. Lett. **85**, 2380 (2000).
9. P. Vonlanthen, K. V. Tanaka, A. Goto, *et al.*, Phys. Rev. B **65**, 214413 (2002).
10. M. Isobe, E. Ninomiya, A. N. Vasil'ev, and Y. Ueda, J. Phys. Soc. Jpn. **71**, 1423 (2002).
11. L. J. de Jongh and A. R. Miedema, Adv. Phys. **50**, 947 (2001).
12. H. J. Schulz, Phys. Rev. Lett. **77**, 2790 (1996).
13. J. W. Stout and E. Catalano, J. Chem. Phys. **23**, 2013 (1955).

Translated by E. Golyamina

JETP Letters, Vol. 78, No. 9, 2003, pp. 555–559. Translated from Pis'ma v Zhurnal Éksperimental'noĭ i Teoreticheskoĭ Fiziki, Vol. 78, No. 9, 2003, pp. 1043–1047.

Oscillations of Superconducting Transition Temperature in Strong Ferromagnet–Superconductor Bilayers

B. P. Vodopyanov[1, 2] and L. R. Tagirov[1, 2]

[1] *Zavoĭskiĭ Physicotechnical Institute, Kazan Scientific Center, Russian Academy of Sciences, Sibirskiĭ trakt 10/7, Kazan 29, 420029 Tatarstan, Russia*

[2] *Kazan State University, ul. Lenina 18, Kazan, 420008 Tatarstan, Russia*

Received September 22, 2003

The superconducting transition temperature T_c of a "clean ferromagnet–dirty superconductor" bilayer is calculated using boundary conditions derived for the quasiclassical Green's function. This combination corresponds to the majority of experiments, in which Fe, Ni, Co, or Gd are used as a material for the ferromagnetic layer. It is shown that T_c oscillates upon changing thickness of the ferromagnetic layer, in accordance with the experimental observations. © *2003 MAIK "Nauka/Interperiodica".*

PACS numbers: 74.78.Fk; 74.50.+r; 74.62.-c

The superconductor–ferromagnet contacts and layered systems are of interest both from the viewpoint of implementing inhomogeneous pairing of the Larkin–Ovchinnikov–Fulde–Ferrel (LOFF) type [1, 2] and as a main combination of materials in constructing π junctions [3] and superconducting logical networks on their base [4, 5]. The inhomogeneous pairing in a ferromagnet manifests itself by the oscillations of superconducting transition temperature [6–9], tunneling density of states [10], and Josephson current [11–13] in the ferromagnet–superconductor (F/S) bi- and multilayers. Although the LOFF scenario for the superconductor contacts with weak ferromagnets (ferromagnetic alloys with a low (100 K and lower) magnetic ordering temperature [5, 10–13]) can be considered proved, the question remains open for the contacts of superconductors and strong ferromagnets (Fe, Co, Ni, Gd). The presently available calculations of the tunneling density of states [14, 15] and superconducting transition temperature for the F/S bilayers [15] do not predict oscillations of the above-mentioned quantities as functions of ferromagnetic layer thickness in the case of a clean ferromagnet. By the clean ferromagnet we mean a material in which the oscillation wavelength of the pair wave function is small compared to the bulk mean free path of conduction electrons. Therefore, an important question arises of how the information about the character of pair correlations can be gained for a strong ferromagnet if the LOFF-type correlations do not show themselves in the oscillatory phenomena, while the Josephson π junction can hardly be obtained because one is forced to deal with the thicknesses of two to five monolayers of ferromagnetic metal. In this work, we will show that the superconducting transition temperature in a "clean ferromagnet–superconductor" bilayer system oscillates with changing the thickness of the ferromagnetic layer.

1. Boundary conditions for a "clean ferromagnet–dirty superconductor" bilayer. In our preceding work [16], we have derived quasiclassical equations of superconductivity for metals with the spin-split conduction band:

$$\operatorname{sgn}(\hat{p}_{xj})\frac{\partial}{\partial x}\hat{g} + \frac{1}{2}\mathbf{v}_{\parallel}\frac{\partial}{\partial \rho}(\hat{v}_{xj}^{-1}\hat{g} + \hat{g}\hat{v}_{xj}^{-1}) + [\hat{K}, \hat{g}]_- = 0,$$

$$\operatorname{sgn}(\hat{p}_{xj})\frac{\partial}{\partial x}\hat{\Upsilon} + \frac{1}{2}\mathbf{v}_{\parallel}\frac{\partial}{\partial \rho}(\hat{v}_{xj}^{-1}\hat{\Upsilon} - \hat{\Upsilon}v_{xj}^{-1}) + [\hat{K}, \hat{\Upsilon}]_+ = 0, \quad (1)$$

$$\hat{K} = -i\hat{v}_{xj}^{-\frac{1}{2}}(i\varepsilon_n\hat{\tau}_n + \hat{\Delta} - \hat{\Sigma})\hat{v}_{xj}^{-\frac{1}{2}} - i(\hat{p}_{xj} - \hat{\tau}_x\hat{p}_{xj}\hat{\tau}_x)/2,$$

$$[a, b]_{\pm} = ab \pm ba.$$

Here, $\varepsilon_n = (2n + 1)\pi T$ is the Matsubara frequency; $\alpha = (\downarrow, \uparrow)$ is the spin index; $\hat{\tau}_\alpha$ are the Pauli matrices; and the quasiclassical Green's functions (GFs) $\hat{g}$ and $\hat{\Upsilon}$ of, respectively, superconductor (S) and ferromagnet (F) have the following structure:

$$\hat{g} = \begin{pmatrix} g_{\alpha\alpha} & f_{\alpha-\alpha} \\ -\bar{f}_{-\alpha\alpha} & \bar{g}_{-\alpha-\alpha} \end{pmatrix}, \quad \hat{g} = \begin{cases} \hat{g}_>, & \hat{p}_{xj} > 0, \\ \hat{g}_<, & \hat{p}_{xj} < 0. \end{cases} \quad (2)$$

The index $j = 1, 2$ denotes metals situated to the left and right of the F/S interface; the latter coincides with the $x = 0$ plane. We will assume that the ferromagnetic film of thickness d^F is on the left and the superconducting film of thickness $d^S > l^S$ (l^S is the mean free path in the superconductor) is on the right. $\hat{\Delta}$ and $\hat{p}_{xj}$ are the matrices of order parameter and of the conduction elec-

tron momentum component perpendicular to the contact plane,

$$\hat{\Delta} = \begin{pmatrix} 0 & \Delta \\ -\Delta^* & 0 \end{pmatrix}, \quad \hat{p}_x = \begin{pmatrix} p_{x\alpha} & 0 \\ 0 & p_{x(-\alpha)} \end{pmatrix},$$

and $\hat{\Sigma}$ is the impurity self-energy part [16, 17]

$$\hat{\Sigma}^F = -ic|u|^2 \int \frac{d\mathbf{p}_\parallel}{(2\pi)^2} (\hat{v}_x)^{-\frac{1}{2}} \hat{g}^F (\hat{v}_x)^{-\frac{1}{2}},$$

$$\hat{\Sigma}^S = -i\frac{1}{2\tau^S}\langle \hat{g}^S \rangle, \quad \frac{1}{\tau^S} = c|u|^2 \frac{mp^S}{\pi}.$$

Here, $\mathbf{p}_\parallel$ is the projection of electron momentum onto the contact plane; p^S is the Fermi momentum in superconductor; u is the interaction potential of electron and impurity atom; c is the impurity concentration; τ^S is the mean free time of electron in superconductor; and the angular brackets stand for the integration over the entire solid angle: $\langle \ldots \rangle = \oint d\Omega / 4\pi$.

In the case of specular electron reflection, the boundary conditions (BCs) to Eqs. (1) at the F/S interface have the following form [16]:

$$\begin{aligned} \hat{\tilde{g}}_a^+ \hat{b}_1 + \hat{b}_2 \hat{\tilde{g}}_a^+ + \hat{\tilde{g}}_a^- \hat{b}_3 + \hat{b}_4 \hat{\tilde{g}}_a^- &= \hat{b}_3 - \hat{b}_4, \\ \hat{\tilde{g}}_a^- \hat{b}_1 + \hat{b}_2 \hat{\tilde{g}}_a^- + \hat{\tilde{g}}_a^+ \hat{b}_3 + \hat{b}_4 \hat{\tilde{g}}_a^+ &= \hat{b}_1 - \hat{b}_2. \end{aligned} \tag{3}$$

The matrices $\hat{b}_i$ are

$$\begin{aligned} \hat{b}_1 &= \hat{\tilde{\Upsilon}}_s^+ \hat{\tilde{g}}_s^- + \hat{\tilde{\Upsilon}}_s^- \hat{\tilde{g}}_s^+, \quad \hat{b}_2 = \hat{\tilde{g}}_s^+ \hat{\tilde{\Upsilon}}_s^- + \hat{\tilde{g}}_s^- \hat{\tilde{\Upsilon}}_s^+, \\ \hat{b}_3 &= \hat{\tilde{\Upsilon}}_s^+ \hat{\tilde{g}}_s^+ + \hat{\tilde{\Upsilon}}_s^- \hat{\tilde{g}}_s^-, \quad \hat{b}_4 = \hat{\tilde{g}}_s^+ \hat{\tilde{\Upsilon}}_s^+ + \hat{\tilde{g}}_s^- \hat{\tilde{\Upsilon}}_s^-. \end{aligned} \tag{4}$$

In Eqs. (3) and (4), $\hat{\tilde{g}}_{a(s)}^{\pm} = 1/2[\hat{\tilde{g}}_{a(s)}^S \pm \hat{\tilde{g}}_{a(s)}^F]$, where the matrices $\hat{\tilde{g}}_{s(a)}$ and $\hat{\tilde{\Upsilon}}_{s(a)}$ are symmetric (s) and antisymmetric (a) with respect to the variable p_{xj}:

$$\begin{aligned} \hat{\tilde{g}}_{s(a)} &= 1/2[\hat{\tilde{g}}_> \pm \hat{\tilde{g}}_<], \quad \hat{\tilde{\Upsilon}}_{s(a)} = 1/2[\hat{\tilde{\Upsilon}}_> \pm \hat{\tilde{\Upsilon}}_<], \\ \hat{\tilde{g}}_>^S &= e^{i\tilde{\vartheta}_{rd}} \tilde{g}_>^S e^{-i\tilde{\vartheta}_{rd}}, \quad \hat{\tilde{g}}_<^S = e^{-i\tilde{\vartheta}_{rd}} \tilde{g}_<^S e^{i\tilde{\vartheta}_{rd}}, \\ \hat{\tilde{\Upsilon}}_>^S &= e^{i\tilde{\vartheta}_{rd}} \tilde{\Upsilon}_>^S e^{i\tilde{\vartheta}_{rd}}, \quad \hat{\tilde{\Upsilon}}_<^S = e^{-i\tilde{\vartheta}_{rd}} \hat{\Upsilon}_<^S e^{-i\tilde{\vartheta}_{rd}}, \\ \hat{\vartheta}_{rd} &= \frac{\hat{\vartheta}_r}{2} - \hat{\vartheta}_d, \end{aligned} \tag{5}$$

where $\hat{\vartheta}_r$ and $\hat{\vartheta}_d$ are the phases of scattering amplitudes at the F/S interface.

The explicit form of matrices $\hat{\tilde{g}}_s^{\pm}$ is given in [16]. To obtain BCs for the quasiclassical GFs at the interface between a strong ferromagnet and dirty superconductor, it is necessary to obtain solutions to Eqs. (1) for each of the metals. Near T_c, the matrices $\hat{g}^{S(F)}$ in the linear approximation in order parameter can be written as

$$\hat{g}^{S(F)} = \frac{\varepsilon_n}{|\varepsilon_n|}\hat{\tau}_z + \hat{f}^{S(F)}, \quad \hat{f}^{S(F)} = \begin{pmatrix} 0 & f_{\uparrow\downarrow}^{S(F)} \\ -\bar{f}_{\uparrow\downarrow}^{S(F)} & 0 \end{pmatrix},$$

then Eq. (1) for a superconductor homogeneous in the contact plane takes the following form:

$$\begin{aligned} \mathrm{sgn}(p_x^S)\frac{\varepsilon_n}{|\varepsilon_n|}\hat{\tau}_z l_x^S \frac{\partial}{\partial x}\hat{f}^S + \lambda^S \hat{f}^S &= \langle \hat{f}^S \rangle - 2i\tau^S \hat{\Delta}, \\ \lambda^S &= 1 + 2|\varepsilon_n|\tau^S. \end{aligned} \tag{6}$$

Here, $l_x^S = |v_x^S|\tau^S$ is the electron mean free path in the direction perpendicular to the contact plane. Passing over to symmetric $\hat{f}_s^S$ and antisymmetric $\hat{f}_a^S$ GFs by formulas (5), one obtains the following equations for $\hat{f}_s^S$ and $\hat{f}_a^S$:

$$\begin{aligned} l_x^2 \frac{\partial^2}{\partial x^2}\hat{f}_s^S - (\lambda^S)^2 \hat{f}_s^S + \lambda^S \langle \hat{f}_s^S \rangle &= 2i\lambda^S \tau^S \hat{\Delta}, \\ l_x \frac{\partial \hat{f}_s^S}{\partial x} &= -\lambda^S \mathrm{sgn}(\varepsilon_n)\hat{\tau}_z \hat{f}_a^S. \end{aligned} \tag{7}$$

The equations for the ferromagnetic quasiclassical GFs $\hat{f}_s^F$ and $\hat{f}_a^F$ are obtained in a similar manner:

$$\begin{aligned} \left(\frac{2l_{x\uparrow}l_{x\downarrow}}{l_{x\uparrow}+l_{x\downarrow}}\right)^2 \frac{\partial^2}{\partial x^2}\hat{f}_s^F - (\lambda^F)^2 \hat{f}_s^F \\ = -2\frac{\sqrt{v_{x\uparrow}v_{x\downarrow}}}{l_{x\uparrow}+l_{x\downarrow}}\tau_\uparrow \tau_\downarrow \lambda^F \left\langle \frac{1}{\tau_{\uparrow\downarrow}}\hat{f}_s^F \right\rangle, \\ \hat{f}_a^F = -\mathrm{sgn}(\varepsilon_n)\frac{2l_{x\uparrow}l_{x\downarrow}}{\lambda^F(l_{x\uparrow}+l_{x\downarrow})}\hat{\tau}_z \frac{\partial}{\partial x}\hat{f}_s^F, \\ \lambda^F = 1 + \frac{2\tau_\uparrow\tau_\downarrow(v_{x\uparrow}+v_{x\downarrow})}{l_{x\uparrow}+l_{x\downarrow}}|\varepsilon_n| - i\frac{2l_{x\uparrow}l_{x\downarrow}}{l_{x\uparrow}+l_{x\downarrow}}(p_{x\uparrow}-p_{x\downarrow})\frac{\varepsilon_n}{|\varepsilon_n|}, \\ \left\langle \frac{1}{\tau_{\uparrow\downarrow}}\hat{f}_s^F \right\rangle = c|u|^2 \int \frac{d\mathbf{p}_\parallel}{(2\pi)^2}\frac{1}{\sqrt{v_{x\uparrow}v_{x\downarrow}}}\hat{f}_s^F. \end{aligned} \tag{8}$$

Here, $l_{x\alpha} = |v_{x\alpha}^F|\tau_\alpha^F$ and τ_α^F is the electron mean free time in the corresponding conduction spin subband of the ferromagnet. In Eq. (8) and in what follows, the physical quantities with index $\alpha = (\uparrow, \downarrow)$ refer to the ferromagnet. The angular integration in Eq. (8) should be made taking into account the specular electron reflection from the interface:

$$p_\parallel = p_\downarrow \sin\theta_\downarrow = p_\uparrow \sin\theta_\uparrow = p^S \sin\theta^S. \tag{9}$$

In Eq. (9), $p_\uparrow$ and $p_\downarrow$ are the Fermi momenta in the spin subbands of the ferromagnet.

The solution to Eq. (6) for a semi-infinite sample with boundary condition $\hat{f}_a^S(x \longrightarrow \infty) = 0$ is

$$\hat{f}_s^S(x) = \mathrm{sgn}(\varepsilon_n)\hat{\tau}_z\hat{f}_a^S(x) + \frac{1}{l_x^S}\int_x^\infty d\xi e^{-\frac{\lambda^S(\xi - x)}{l_x^S}}[\langle \hat{f}_s^S(\xi)\rangle - 2i\tau^S\hat{\Delta}(\xi)]. \quad (10)$$

In Eq. (10), the integrand changes at a distance on the order of $\xi_T^S = (D^S/2\pi T)^{1/2} \gg l^S$, where $D^S = v^S l^S/3$ is the electron diffusivity in the superconductor. By expanding and factoring it outside the integral sign at the point $\xi = x$, one finds

$$\hat{f}_s^S(x) = \frac{\varepsilon_n}{|\varepsilon_n|}\hat{\tau}_z\hat{f}_a^S(x) + \frac{1}{\lambda^S}\left(1 + \frac{l_x^S}{\lambda^S}\frac{d}{dx}\right)\langle \hat{f}_s^S(x)\rangle. \quad (11)$$

For definiteness, we assume below that $p_\uparrow > p_\downarrow$ and seek for the ferromagnet solution to Eq. (8) in the form

$$\hat{f}_s^F(x) = C^F(\theta_\downarrow)\cosh[\kappa^F(\theta_\downarrow)(x + d^F)], \quad (12)$$

where

$$\kappa^F(\theta_\downarrow) = \kappa_1^F(\theta_\downarrow) + i\,\mathrm{sgn}(\varepsilon_n)\kappa_2^F(\theta_\downarrow),$$

$$\kappa_1^F(\theta_\downarrow) = (1 - \eta_1)\frac{l_{x\uparrow} + l_{x\downarrow}}{2l_{x\uparrow}l_{x\downarrow}} + \frac{v_{x\uparrow} + v_{x\downarrow}}{2v_{x\uparrow}v_{x\downarrow}}|\varepsilon_n|, \quad (13)$$

$$\kappa_2^F(\theta_\downarrow) = |p_{x\uparrow} - p_{x\downarrow}| + \eta_2\frac{l_\uparrow + l_\downarrow}{l_\uparrow l_\downarrow}.$$

In Eq. (13), the quantities η_1 and η_2 are independent of the angles $\theta_\uparrow$ and $\theta_\downarrow$. By substituting solution (12) into Eq. (8), one obtains the integral equation for the constants η_1 and η_2:

$$l_\uparrow\frac{p_\downarrow}{p_\uparrow}\int_0^{\pi/2} d\theta_\downarrow \frac{\sin(2\theta_\downarrow)\lambda^F(l_{x\uparrow} + l_{x\downarrow})}{(\lambda^F)^2(l_{x\uparrow} + l_{x\downarrow})^2 - (2l_{x\uparrow}l_{x\downarrow})^2(\kappa^F)^2} = 1.$$

For a ferromagnet with large splitting of spin subbands, the solution to this equation, accurate to the terms on the order of $(p_\uparrow l_\uparrow)^{-1} \ll 1$, has the form

$$\eta_1 = \frac{l_\uparrow p_\downarrow}{2p_\uparrow}\int_0^{\pi/2} d\theta_\downarrow \frac{\sin(2\theta_\downarrow)}{l_{x\uparrow} + l_{x\downarrow}}, \quad \eta_2 = 0. \quad (14)$$

Let us now express the function $\hat{f}_s^F(x)$ through $\hat{f}_a^F(x)$ at $x = 0$,

$$\hat{f}_s^F(0) = -\frac{\varepsilon_n}{|\varepsilon_n|}\frac{\lambda^F(l_{x\uparrow} + l_{x\downarrow})}{2l_{x\uparrow}l_{x\downarrow}\kappa^F\tanh(\kappa^F d^F)}\hat{\tau}_z\hat{f}_a^F(0), \quad (15)$$

and construct the $\hat{f}_s^\pm$ combinations of $\hat{f}_s^S(x)$ (11) and $\hat{f}_s^F(x)$ (15) at $x = 0$. By substituting them into the BC system (3), one finds $\hat{f}_a^S(0)$ and $\hat{f}_a^F(0)$:

$$\hat{f}_a^S(0) = -\mathrm{sgn}(\varepsilon_n)\hat{\tau}_z B\frac{1}{\lambda^S}\left(1 + \frac{l_x^S}{\lambda^S}\frac{d}{dx}\right)\langle \hat{f}_s^S(x)\rangle,$$

$$\hat{f}_a^F(0) = -2\frac{\varepsilon_n}{|\varepsilon_n|}\frac{\sqrt{D_\uparrow D_\downarrow}}{\Gamma}\frac{1}{\lambda^S}\hat{\tau}_z\left(1 + \frac{l_x^S}{\lambda^S}\frac{d}{dx}\right)\langle \hat{f}_s^S(x)\rangle,$$

$$B = \frac{\Gamma^S}{\Gamma}, \quad \Gamma^S = D_\uparrow + D_\downarrow + (\sqrt{R_\uparrow} - \sqrt{R_\downarrow})^2\nu^F, \quad (16)$$

$$\Gamma = 2[1 + \sqrt{R_\uparrow R_\downarrow} + (1 - \sqrt{R_\uparrow R_\downarrow})\nu^F],$$

$$\nu^F = \frac{\lambda^F(l_{x\uparrow} + l_{x\downarrow})}{2l_{x\uparrow}l_{x\downarrow}\kappa^F\tanh(\kappa^F d^F)}.$$

Here, $D_\alpha = 1 - R_\alpha$ is the quantum-mechanical transmission coefficient through the F/S interface for an electron with spin projection α. When solving the system of BC Eqs. (3), the spin dependence of the phases of scattering amplitudes was ignored.

It was pointed out in [18] that, at distances on the order of the momentum mean free path l^S from the interface, the terms proportional to ε_n and $\hat{\Delta}$ can be ignored, and the quantity

$$\langle \cos(\theta^S)\hat{f}^S\rangle = \frac{1}{2}\int_0^{\pi/2} d\theta^S \sin(2\theta^S)\hat{f}_a^S = \hat{C}^S \quad (17)$$

is constant. The $\hat{C}^S$ constant can be found, as in [18], by substituting the quantity $[-\hat{\tau}_z\,\mathrm{sgn}(\varepsilon_n)l_x^S(d/dx)\langle \hat{f}_s^S\rangle]$, corresponding to a solution to the Usadel equations [19] in the bulk of a dirty superconductor, for the GF $\hat{f}_a^S$ in Eq. (17). The result is

$$\hat{C}^S = -\hat{\tau}_z\,\mathrm{sgn}(\varepsilon_n)\frac{1}{3}l^S\frac{d}{dx}\langle \hat{f}_s^S\rangle. \quad (18)$$

Now, by evaluating the $\hat{C}^S$ constant once more using the GF $\hat{f}_a^S(0)$ from Eq. (16), one obtains the BC for the

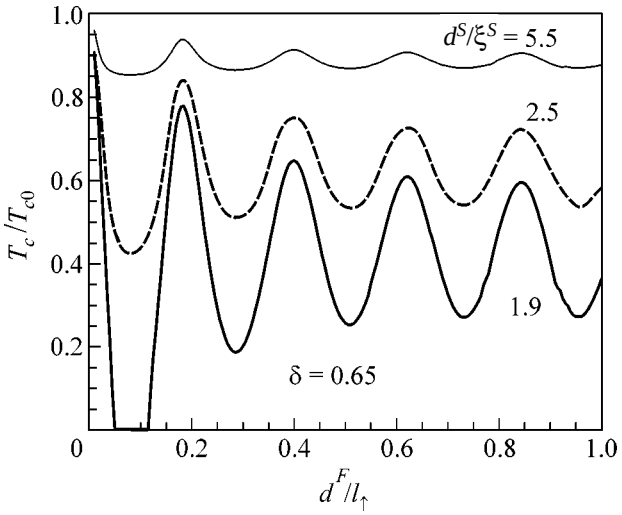

Fig. 1. Superconducting transition temperature of the S/F bilayer vs. the thickness of ferromagnetic layer with δ = 0.65. For the values of other physical parameters, see text.

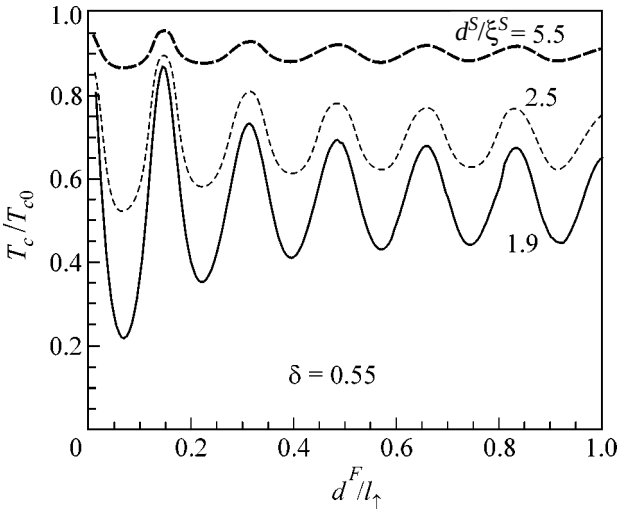

Fig. 2. Superconducting transition temperature of the S/F bilayer vs. the thickness of ferromagnetic layer with δ = 0.55. The values of other physical parameters are as in Fig. 1.

GF $\hat{F}_s^S(x) = \langle \hat{f}_s^S \rangle$ at the interface of a strong ferromagnet and a dirty superconductor:

$$l^S \frac{d}{dx}\hat{F}_s^S(x) = \gamma \hat{F}_s^S(x), \quad \gamma_1 = \frac{3}{2}\int_0^\varphi d\theta^S \sin(2\theta^S) B,$$
$$\gamma = \frac{\gamma_1}{1-\gamma_2}, \quad \gamma_2 = \frac{3}{2}\int_0^\varphi d\theta^S \sin(2\theta^S)\cos\theta^S B. \tag{19}$$

The upper limit in the integral in Eq. (19) depends on the ratio between the Fermi momenta of the contacting metals and is determined from the specular reflection condition (9). For instance, $\varphi = \pi/2$ at $p^S < p_\downarrow$. The quantity B in Eq. (16) is a function of the angles $\theta_\downarrow$ and θ^S related to each other by formulas (9). The obtained boundary condition is valid for the arbitrary interface transmittance.

2. Evaluation of the critical temperature for a F/S bilayer. To evaluate T_c of a bilayer, one has to solve the Usadel equation in the vicinity of superconducting critical temperature,

$$D\frac{d^2}{dx^2}\hat{F}_s^S - 2|\varepsilon_n|\hat{F}_s^S = 2i\hat{\Delta} \tag{20}$$

with BCs (19). The problem can easily be solved using a single-mode approximation suggested in [20]:

$$\hat{F}_s^S = -\frac{2i\hat{\Delta}}{|\varepsilon_n| + D(\kappa^S)^2}, \quad \hat{\Delta} = \hat{\Delta}_0 \cos[\kappa^S(x - d^S)], \tag{21}$$

where κ^S is determined from BCs (19):

$$l^S \kappa^S \tan(\kappa^S d^S) = \gamma. \tag{22}$$

By substituting Eq. (21) into the self-consistency equation

$$\hat{\Delta}\ln(t_c) = \pi T \sum_{n=-\infty}^{\infty}\left(i\hat{F}_s^S - \frac{\hat{\Delta}}{|\varepsilon_n|}\right); \quad t_c = \frac{T_c}{T_{c0}},$$

one arrives at the equation for the critical temperature of a clean ferromagnet–dirty superconductor bilayer:

$$\ln(t_c) = \Psi\left(\frac{1}{2}\right) - \mathrm{Re}\,\Psi\left(\frac{1}{2} + \frac{D^S(\kappa^S)^2}{4\pi T_{c0} t_c}\right). \tag{23}$$

3. Results and discussion. As in the preceding work [16], we determine the Fermi momentum of superconductor by the relation $(p^S)^2 = [(p_\uparrow)^2 + (p_\downarrow)^2]/2$ and evaluate the transmission coefficients D_α using model expressions for a direct contact of two metals (Eqs. (22) in [16]).

The results of calculation with parameters δ = $p_\downarrow/p_\uparrow = 0.65$, $p_\uparrow l_\uparrow = 40.0$, $l_\downarrow/l_\uparrow = 2.5$, and $\xi^S/\xi^S_{BCS} = 0.25$ (ξ^S equals ξ^S_T at temperature $T = T_{c0}$) are presented in Fig. 1. These parameters are close to those for the nickel contact with niobium or vanadium. One can see in Fig. 1 that, with an increase in the thickness of the ferromagnetic layer, the critical temperature of the bilayer undergoes damped oscillations, as was observed experimentally in [6–9]. If the superconductor becomes thin enough, T_c can display re-entrant behavior (the lower solid curve in Fig. 1), which was also observed in the experiment [21]. The results of another calculation with the conduction-band spin-splitting parameter δ = 0.55 (close to cobalt) are shown in Fig. 2. One can see from the comparison with Fig. 1 that the degree of suppression of the superconducting T_c

in contact with stronger ferromagnet (i.e., having smaller δ value) is lower, which seems at first glance to be illogical. What actually happens is that the transmittance of the S/F interface decreases with an increase in the polarization of conduction band because of the increasing mismatch between the Fermi momenta of superconductor and spin subbands in ferromagnet. The attendant isolation between the F and S layers predominates over the enhanced depairing effect of exchange field. This scenario was implemented experimentally in the Fe_xV_{1-x}/V bilayers [22]. As the iron concentration x in the ferromagnetic Fe_xV_{1-x} alloy increased, the critical thickness of the superconducting vanadium layer displayed nonmonotonic behavior at a fixed thickness of the ferromagnetic layer. The pure iron layer suppressed T_c weaker than did the alloy with $x \sim 0.6$. This work provides a theoretical basis for the discussion of the effect of conduction-band spin splitting on the transmittance of the S/F interface [9, 21–23]. Our results are not contradictory to the conclusions of work [15]: Figs. 1 and 2 show that, in the case of weak T_c suppression ($T_{c0} - T_c \ll T_{c0}$ and $d^F > l_\uparrow$), the T_c oscillation amplitude is substantially smaller than the asymptotic value $T_{c0} - T_c(d^F \longrightarrow \infty)$. Therefore, the oscillations fall beyond the approximation adopted in [15]. Interestingly, the oscillation damping constant does not increase with a decrease in the electron mean free path in the ferromagnet, as it could be expected, but decreases, at least for small thicknesses d^F. Such paradoxical behavior is explained by the fact that the exclusion effect for inclined electron trajectories longer than the electron mean free path in ferromagnetic film dominates. As the mean free path approaches the film thickness, the cone of trajectories, whose interference gives rise to the geometric oscillations of T_c, narrows around the normal to the interface, and the solution gradually becomes single-mode [23]. In a certain range of thicknesses, the effect of cone "collapse" and a decrease in the scatter of path lengths for interfering waves dominates over the increase in their damping.

In summary, a consistent theory of the proximity effect has been developed in this work for a "strong ferromagnet–dirty superconductor" system, and an answer is given to the fundamental question of whether the superconducting temperature oscillates as a function of thickness of the ferromagnetic film or not. The answer is positive: yes, it oscillates and the re-entrant behavior of superconducting T_c is possible upon changing thickness of the ferromagnetic layer. The effect of spin splitting on the transmittance of the F/S interface and, hence, on the oscillations of critical temperature has been included in the calculation explicitly and is consistent with the experiment. For a particular comparison with the experiment, the knowledge of many physical parameters is necessary for the theory. Some of them should be determined from the additional measurements with bilayers or pilot films prepared simultaneously with bilayers under the identical conditions. Complete experiments of this type are unknown to us.

We are grateful to G.B. Teĭtel'baum for discussion of results. This work was supported by the Russian Foundation for Basic Research (project no. 03-02-17432) and the program "Russian Universities—Basic Research" (project no. UR.01.01.061).

REFERENCES

1. A. I. Larkin and Yu. N. Ovchinnikov, Zh. Éksp. Teor. Fiz. **47**, 1136 (1964) [Sov. Phys. JETP **20**, 762 (1964)].
2. P. Fulde and R. A. Ferrel, Phys. Rev. **135**, A550 (1964).
3. Z. Radovic, M. Ledvij, L. Dobrosavljevic-Grujic, *et al.*, Phys. Rev. B **44**, 759 (1991).
4. L. R. Tagirov, Phys. Rev. Lett. **83**, 2058 (1999).
5. V. V. Ryazanov, V. A. Oboznov, A. V. Veretennikov, and A. Yu. Rusanov, Phys. Rev. B **65**, 020501 (2002).
6. J. S. Jiang, D. Davidovic, D. H. Reich, and C. L. Chien, Phys. Rev. Lett. **74**, 314 (1995).
7. Th. Mühge, N. N. Garifyanov, Yu. V. Goryunov, *et al.*, Phys. Rev. Lett. **77**, 1857 (1996).
8. Y. Obi, M. Ikebe, T. Kubo, and H. Fujimori, Physica C (Amsterdam) **317–318**, 149 (1999).
9. L. Lazar, K. Westerholt, H. Zabel, *et al.*, Phys. Rev. B **61**, 3711 (2000).
10. T. Kontos, M. Aprili, J. Lesueur, and X. Grison, Phys. Rev. Lett. **86**, 304 (2001).
11. V. V. Ryazanov, V. A. Oboznov, A. Yu. Rusanov, *et al.*, Phys. Rev. Lett. **86**, 2427 (2001).
12. T. Kontos, M. Aprili, J. Lesueur, *et al.*, Phys. Rev. Lett. **89**, 137007 (2002).
13. Y. Blum, A. Tsukernik, M. Karpovski, and A. Palevski, Phys. Rev. Lett. **89**, 187004 (2002).
14. I. Baladie and A. I. Buzdin, Phys. Rev. B **64**, 224514 (2001).
15. F. S. Bergeret, A. F. Volkov, and K. B. Efetov, Phys. Rev. B **65**, 134505 (2002).
16. B. P. Vodopyanov and L. R. Tagirov, Pis'ma Zh. Éksp. Teor. Fiz. **77**, 153 (2003) [JETP Lett. **77**, 126 (2003)].
17. A. I. Larkin and Yu. N. Ovchinnikov, J. Low Temp. Phys. **10**, 401 (1973).
18. M. Yu. Kupriyanov and V. F. Lukichev, Zh. Éksp. Teor. Fiz. **94**, 139 (1988) [Sov. Phys. JETP **67**, 1163 (1988)].
19. K. D. Usadel, Phys. Rev. Lett. **25**, 507 (1970).
20. Z. Radović, L. Dobrosavljević-Grujić, A. I. Buzdin, and J. R. Clem, Phys. Rev. B **38**, 2388 (1988).
21. I. A. Garifullin, D. A. Tikhonov, N. N. Garifyanov, *et al.*, Phys. Rev. B **66**, 020505(R) (2002).
22. J. Aarts, J. M. E. Geers, E. Bruck, *et al.*, Phys. Rev. B **56**, 2779 (1997).
23. L. R. Tagirov, Physica C (Amsterdam) **307**, 145 (1998).

Translated by V. Sakun

JETP Letters, Vol. 78, No. 9, 2003, pp. 560–563. Translated from Pis'ma v Zhurnal Éksperimental'noĭ i Teoreticheskoĭ Fiziki, Vol. 78, No. 9, 2003, pp. 1048–1052.

Ring Interferometer on the Basis of 2D Electron Gas in a Double Quantum Well

A. A. Bykov[1, *], D. V. Nomokonov[1], A. K. Bakarov[1], A. I. Toropov[1], O. Estibals[2], and J. C. Portal[2]

[1] *Institute of Semiconductor Physics, Siberian Division, Russian Academy of Sciences, Novosibirsk, 630090 Russia*
**e-mail: bykov@thermo.isp.nsc.ru*

[2] *Grenoble High Magnetic Fields Laboratory, MPI-FKF and CNRS B.P.166, F-38042 Grenoble, France*

Received September 25, 2003

Magnetotransport properties of submicron rings fabricated on the basis of 2D electron gas in a GaAs double quantum well are studied. It is shown that, in such interferometers, the Aharonov–Bohm effect is caused by coherent processes in two weakly coupled rings, which have different widths of electron channels. In these interferometers, a phase inversion of *h*/*e* oscillations is observed under the action of the parallel component of a tilted magnetic field. This phenomenon is qualitatively explained by a redistribution of charge carriers in the two rings. © *2003 MAIK "Nauka/Interperiodica".*

PACS numbers: 73.21.Fg; 73.23.-b

Studies of the charge carrier transport in ring interferometers and quantum dots fabricated on the basis of 2D electron gas in selectively doped semiconductor structures were initiated more than 15 years ago [1, 2] and remain topical to this day [3]. In the last few years, interest in studying the properties of these microstructures has been primarily associated with the fact that they serve as a basis for designing qubits [4] and for realizing fundamentally new information technologies that use quantum computations. This paper reports the study of coherent properties of ring interferometers fabricated on the basis of 2D electron gas in a GaAs double quantum well with AlAs/GaAs superlattice barriers. It is found that the quantum transport in such rings is influenced not only by the perpendicular component of magnetic field but also by its parallel component.

The initial selectively doped structures were grown by molecular beam epitaxy (MBE). The cross section of a double quantum well is schematically shown in Fig. 1a. The central barrier was a 5-nm-thick AlGaAs layer, and the external barriers were AlAs/GaAs superlattices of the second kind [5]. The δ-Si doping layers were located in the superlattice external barriers on both sides of the quantum wells, each being 10 nm wide. The MBE structures were processed by optical lithography and liquid etching to obtain bridges 50 μm in width. Each bridge had one pair of current terminals and three pairs of Hall terminals separated by 100 μm. The concentrations and mobilities of 2D electron gas were determined from the transverse and longitudinal magnetoresistance at a temperature of $T = 4.2$ K, and their values before and after illumination by a red light-emitting diode were as follows: $n_s = 1.7 \times 10^{12}$ cm^{-2}, $\mu = 95 \times 10^3$ cm^2/(V s) and $n_s = 2.0 \times 10^{12}$ cm^{-2}, and $\mu = 130 \times 10^3$ cm^2/(V s).

The ring was fabricated by electron beam lithography and dry etching and positioned between two pairs of Hall terminals. The resulting sample is schematically shown in Fig. 1b. The mean ring radius, which was equal to half the sum of the outer and inner radii provided by lithography, was $r_0 = 0.3$ μm. Experiments were carried out at temperatures from 4.2 to 1.6 K in magnetic fields B up to 15 T. The ring resistance was measured by the four-probe method. The parallel component of the magnetic field was perpendicular to the bridge longitudinal axis. The tilt of the magnetic field was controlled by the value of the transverse (Hall) resistance.

Figure 2a shows the dependences $R_{34}(1/B)$ before and after illumination of the sample by a red light-emitting diode (curves *1* and *2*, respectively). The results of Fourier analysis of these dependences are presented in Fig. 2b. One can see that the Fourier transform of Shubnikov–de Haas oscillations shows two maxima in both cases. The concentration of 2D electron gas, when determined from the transverse magnetoresistance, was equal to the sum of concentrations calculated from the positions of these maxima. This means that, in the MBE structure under study, two energy levels, E_0 and E_1, are filled. The distance between these levels before illumination was $\Delta E = E_1 - E_0 \simeq 14$ meV. After illumination, it became smaller and was equal to 11 meV. From the calculation of energy positions of the E_0 and E_1 levels in the structure shown in Fig. 1a, it was found that the tunnelling coupling of wells must result in the splitting $\Delta E \simeq 1$ meV. Thus, the value of ΔE observed for the

0021-3640/03/7809-0560$24.00

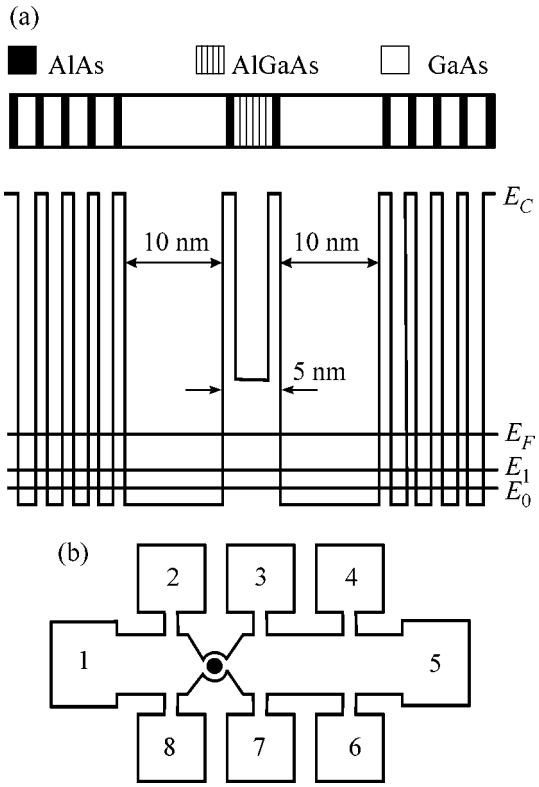

Fig. 1. (a) Schematical section and energy diagram of a GaAs double quantum well with AlAs/GaAs superlattice barriers. (b) Schematic representation of a ring interferometer with (1, 5) current and (2–4, 6–8) potential terminals.

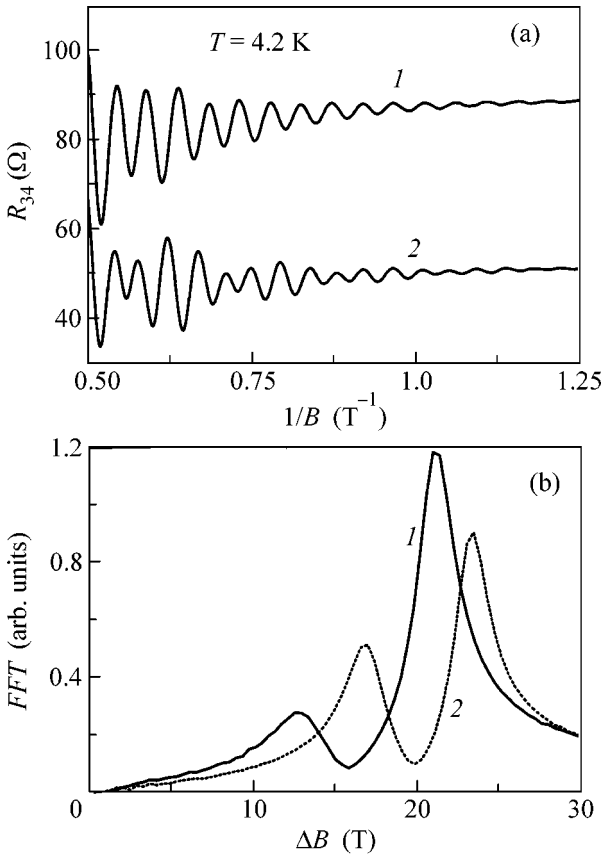

Fig. 2. (a) Dependences $R_{34}(1/B)$ at T = 4.2 K (*1*) before and (*2*) after illumination. (b) Results of a fast Fourier transform of the $R_{34}(1/B)$ functions (*1*) before and (*2*) after illumination.

given MBE structure is mainly caused by the shift of the wells in the energy axis as a result of the bending of energy bands under the effect of internal electrostatic field, rather than by the tunneling coupling of the wells.

Figure 3a shows the field dependence of the resistance $R_{23}(B)$ in a perpendicular magnetic field before the illumination of the interferometer. The curve representing $\Delta R_{23}(B)$ exhibits periodic resistance oscillations symmetric with respect to the sign of magnetic field. The dependences $R_{23}(B)$ and $\Delta R_{23}(B)$ obtained after the illumination of the sample are shown in Fig. 3b in a broader range of B. One can see that periodic oscillations in the rings under study disappear in magnetic fields higher than 3 T. The Fourier transform of these oscillations (Fig. 4a) show two clearly distinguishable groups of frequencies. The maximal amplitudes in these groups differ by approximately a factor of four, and the mean frequencies, by a factor of two. The mean frequency in the group with higher amplitude corresponds to the quantization of magnetic flux through the area of a circle with the effective radius $r_{\text{eff}} \simeq 0.30$ μm, which is equal (within experimental error) to the mean radius of the ring r_0 provided by the electron beam lithography. This means that the periodic resistance oscillations observed in the rings under study are the h/e oscillations. Then, the group of frequencies with the smaller amplitude is caused by the $h/2e$ oscillations. The phase coherence length determined from the amplitude ratio of the h/e and $h/2e$ oscillations [6] is about 0.7 μm at T = 1.6 K.

Let us discuss the experimental results. As is known, the half-width of the spectral peak of h/e oscillations in submicron rings allows one to estimate the width w_e of electron channels [7]. In our case, this estimate provided a value of about 60 nm. At the same time, the channel width can be estimated from the characteristic magnetic field B_m at which the Aharonov–Bohm oscillations disappear [1]. This field B_m is determined from the condition $(\hbar/eB_m)^{1/2} = w_e/2$. From Fig. 3b, one can see that the Aharonov–Bohm oscillations are observed up to B_m = (2.5–3) T, which gives $w_e \sim 30$ nm for the channel width. Thus, for the effective channel width of our interferometer based on a GaAs double quantum well, the estimate obtained from the halfwidth of the peak of h/e oscillations proved to be noticeably greater than the estimate obtained from B_m (in contrast to the case of rings based on a single quantum well in a GaAs/AlGaAs heterojunction [1]). We explain this discrepancy by the fact that the interferometers under

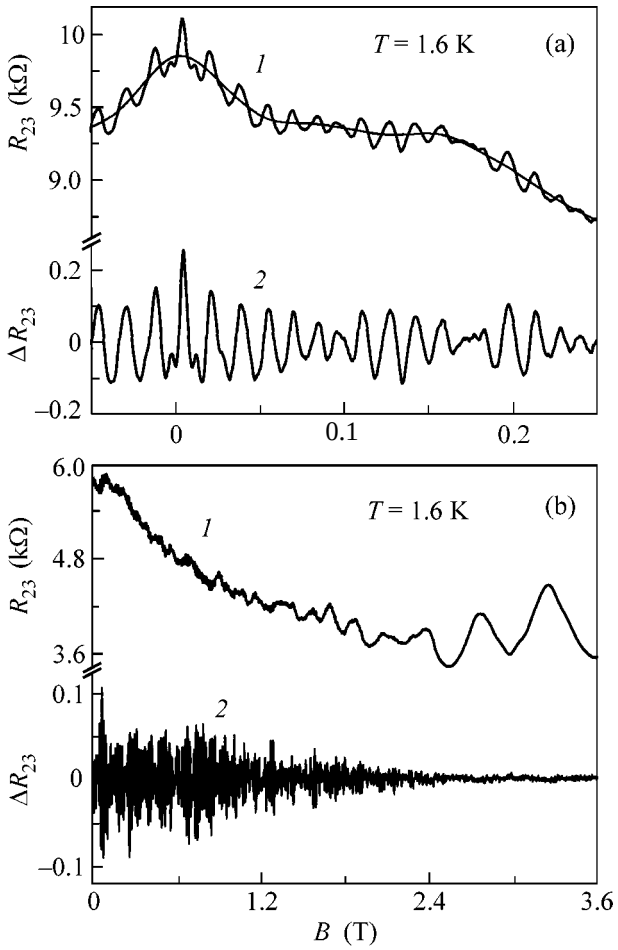

Fig. 3. (a) Dependences $R_{23}(B)$ and $\Delta R_{23}(B)$ before illumination at T = 1.6 K: (*1*) experimental (thick line) and smoothed (thin line) curves obtained for $R_{23}(B)$, and (*2*) the difference between the experimental and smoothed curves $\Delta R_{23}(B)$. (b) Dependences $R_{23}(B)$ and $\Delta R_{23}(B)$ after illumination at T = 1.6 K: (*1*) experimental curve obtained for $R_{23}(B)$ and (*2*) $\Delta R_{23}(B)$.

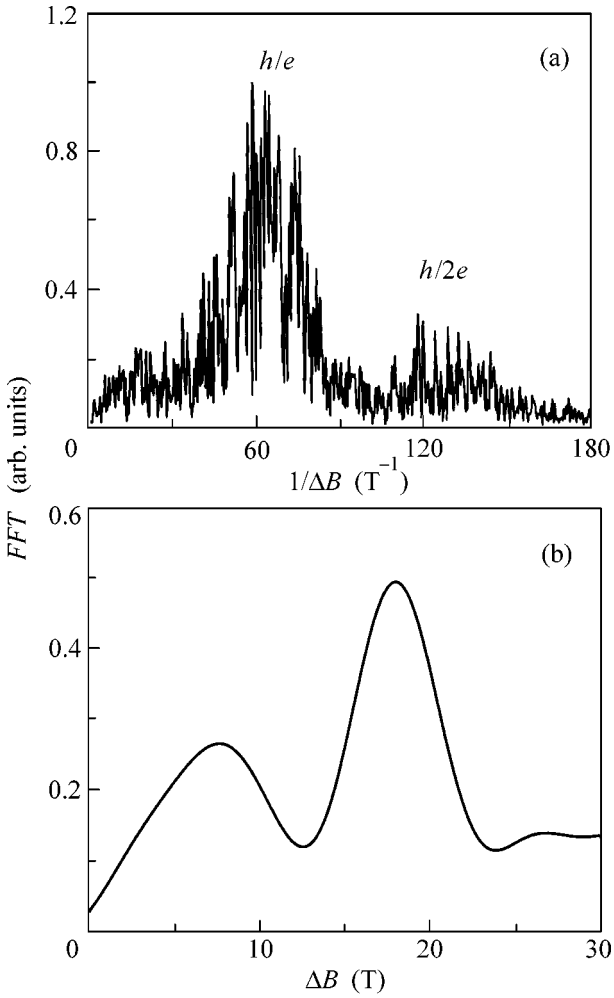

Fig. 4. (a) Result of fast Fourier transform of the $\Delta R_{23}(B)$ functions in the field range from 0 to 3 T. (b) Result of a fast Fourier transform of the $R_{23}(1/B)$ function.

study actually consist of two weakly coupled rings with different widths of electron channels. Since, in the narrower ring, the Aharonov–Bohm oscillations are suppressed in a stronger field, the estimate of the channel width by B_m may provide the value of w_e only for the "narrow" ring. At the same time, the estimate of w_e from the halfwidth of the *h*/*e* oscillation peak may allow one to determine the width of only the wider ring, because the broader peak superimposed on the narrower peak masks the latter. Thus, in the situation with two rings of the same radius but different width, the value of B_m is determined by the "narrow" ring while the halfwidth of the peak of *h*/*e* oscillations is determined by the "wide" ring.

It is well known that w_e of the submicron rings fabricated on the basis of selectively doped semiconductors is determined not only by lithography but, to a considerable extent, by the lateral depletion regions appearing along the etch boundaries. The width of these regions is the smaller the greater the concentration of 2D electron gas in the initial structure [8, 9]. A Fourier transform of Shubnikov–de Haas oscillations observed in the interferometer (Fig. 4b) revealed two peaks (as in the case of 2D electron gas in the initial structure). The 2D electron gas concentrations corresponding to these peaks proved to be slightly lower than in the wide regions of the sample: 0.4×10^{12} and 0.9×10^{12} cm^{-2}. From the above-mentioned dependence of the size of depletion regions (and, hence, the channel widths) on the initial concentrations of charge carriers in the wells, one can assume that the ring lying in the well with lower concentration has a smaller width of electron channels, as compared to the ring lying in the well with higher concentration. In the interferometer under study, the rings are separated by a 5-nm-thick barrier, while the width of the lateral depletion regions along the electron channels is about 120 nm. Taking into account the ratio of these geometric dimensions, we can assume

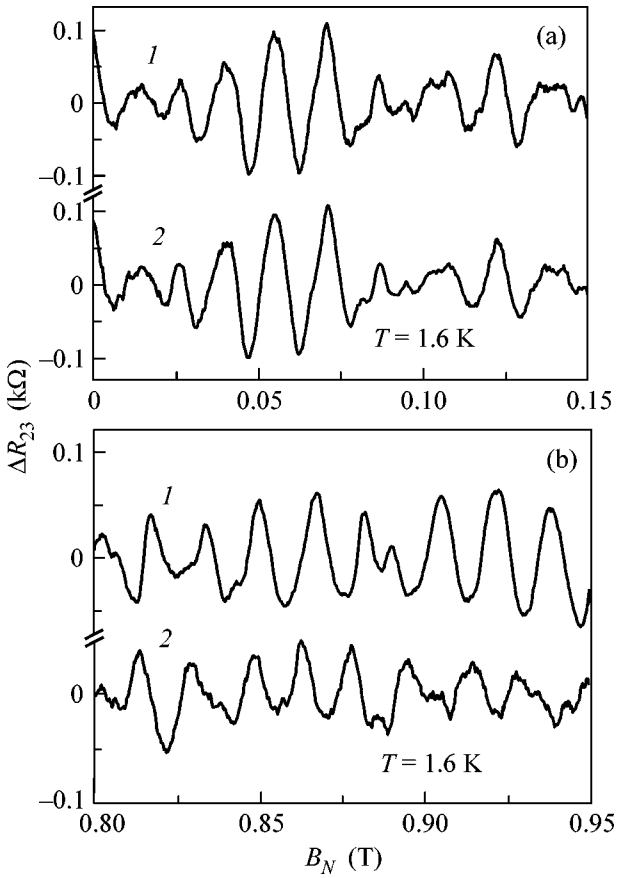

Fig. 5. (a, b) Dependences of ΔR_{23} at $T = 1.6$ K on the perpendicular component of magnetic field B_N: (*1*) in a perpendicular magnetic field with $B_N = B$ and (*2*) in a tilted magnetic field with $B_N = B/15$.

that both rings are in practically identical conditions with respect to the lateral confining potential. Since the rings have noticeably different widths, we can conclude that the lateral confining potential strongly differs in shape from the rectangular potential.

In [10], it was shown that the spectrum of energy states in an asymmetric double quantum well placed in a parallel magnetic field can be considerably modified, leading to the charge-carrier redistribution between the wells. We assume that, for our interferometers consisting of two vertically coupled rings, a parallel magnetic field should also modify the energy spectrum of the rings and lead to the electron redistribution between them, as in the case of a double quantum well. This assumption qualitatively agrees with the fact that, in our experiments, the dependences of the interferometer resistances on the normal component B_N of magnetic field are different in perpendicular and tilted fields.

From Fig. 5a, one can see that, in the case where the parallel component of the tilted field is small, the difference in the interference components of ring resistance is virtually absent. As the parallel component of B increases (Fig. 5b), the oscillations observed in the tilted field tend to be in antiphase with the oscillations observed in the perpendicular magnetic field. Qualitatively, this can be explained by the above-mentioned redistribution of charge carriers in the two rings under the action of the parallel magnetic field. However, it should be noted that, in the interferometers under study, the rings are weakly coupled, and the phase inversion observed for the h/e oscillations may be caused not only by the modification of the ring spectra but also by a synchronous (common) shift of the ring energy levels in the parallel magnetic field. Our estimates of the shifts of the E_0 and E_1 levels for the structure under study in the parallel magnetic field $B = 15$ T did not allow us to determine which of the two mechanisms dominates the phase inversion of h/e oscillations. For a more definite answer to this question, it is necessary to develop a theory of charge-carrier transport in a ring interferometer in a tilted magnetic field and to compare this theory with the experimental data.

Thus, we have fabricated submicron rings on the basis of 2D electron gas in a double quantum well and studied their coherent properties. In such interferometers, we observed a phase inversion of Aharonov–Bohm oscillations under the action of the parallel component of a tilted magnetic field. In other words, we experimentally demonstrated the principal possibility of controlling the coherent processes in ring interferometers by a parallel magnetic field.

We are grateful to A. Vedernikov and V. Tkachenko for fruitful discussions. The work was supported by the Russian Foundation for Basic Research (project no. 01-02-16892).

REFERENCES

1. G. Timp, A. M. Chang, J. E. Cunningham, *et al.*, Phys. Rev. Lett. **58**, 2814 (1987).
2. U. Meirav, M. A. Kastner, and S. J. Wind, Phys. Rev. Lett. **65**, 771 (1990).
3. V. A. Tkachenko, A. A. Bykov, D. G. Baksheev, *et al.*, Zh. Éksp. Teor. Fiz. **124**, 351 (2003) [JETP **97**, 317 (2003)].
4. J. M. Elzerman, R. Hanson, J. S. Greidanus, *et al.*, Phys. Rev. B **67**, 161308 (2003).
5. K.-J. Friedland, R. Hey, H. Kostial, *et al.*, Phys. Rev. Lett. **77**, 4616 (1996).
6. A. E. Hansen, A. Kristensen, S. Pedersen, *et al.*, Phys. Rev. B **64**, 045327 (2001).
7. R. A. Webb, S. Washburn, C. Umbach, and R. A. Laibowitz, Phys. Rev. Lett. **54**, 2696 (1985).
8. A. A. Bykov, L. V. Litvin, and S. P. Moshchenko, Surf. Sci. **361–362**, 747 (1996).
9. A. A. Bykov, A. K. Bakarov, L. V. Litvin, and A. I. Toropov, Pis'ma Zh. Éksp. Teor. Fiz. **72**, 300 (2000) [JETP Lett. **72**, 209 (2000)].
10. A. A. Gorbatsevich, V. V. Kapaev, and Yu. V. Kopaev, Pis'ma Zh. Éksp. Teor. Fiz. **57**, 565 (1993) [JETP Lett. **57**, 580 (1993)].

Translated by E. Golyamina

JETP Letters, Vol. 78, No. 9, 2003, pp. 564–568. Translated from Pis'ma v Zhurnal Éksperimental'noĭ i Teoreticheskoĭ Fiziki, Vol. 78, No. 9, 2003, pp. 1053–1057.

Electric Control of Magnetic Moment in a Ferromagnet/Semiconductor Hybrid System

V. L. Korenev

Ioffe Physicotechnical Institute, Russian Academy of Sciences, St. Petersburg, 194021 Russia

e-mail: korenev@orient.ioffe.ru

Received September 8, 2003; in final form, September 25, 2003

It is shown that the exchange coupling in a "ferromagnet/semiconductor quantum well" heterostructure allows the electric control of the orientation of magnetic moment in the ferromagnet. A highly anisotropic exchange interaction between holes in the quantum well and magnetic atoms in the ferromagnet causes the orientational transition: magnetic moment leaves the plane and becomes oriented along the normal. The normal component of magnetization can be inverted by applying voltage pulses to the structure gate. © *2003 MAIK "Nauka/Interperiodica".*

PACS numbers: 85.35.Be; 85.75.-d

Ferromagnet/semiconductor hybrid systems are promising from the point of view of integration of magnetic systems with semiconductor electronics [1, 2]. On the one hand, the nonequilibrium electron spin of a semiconductor can be used as a detector reading information about the state of a magnetic film. For example, the authors of [3, 4] reported the detection of stray fields of a ferromagnet (FM) using the optical orientation [5] of semiconductor electrons. With the injection from FM into a semiconductor, electrons of the semiconductor acquire a nonequilibrium spin proportional to the electron spin in the ferromagnet [6]. On the other hand, to achieve full integration of magnetism with electronics, it is necessary to use a semiconductor for *controlling* the magnetic properties of ferromagnetic films. Then, it will be possible to perform electronic readout and recording of data on magnetic materials without using magnetic heads. The effect of a semiconductor on an FM was revealed in [3, 4], where it was shown that illumination of a Ni/*n*-GaAs structure caused a twofold change in the coercive force of the NiGaAs ferromagnetic interface. This phenomenon was explained in [7] by the exchange interaction between electrons positioned at deep centers near the ferromagnet/semiconductor heterointerface and magnetic atoms of the ferromagnet (proximity effect). Under conditions of optical orientation, the proximity effect can lead to a magnetization of the film by circularly polarized light [8, 9]. In almost all the cited publications, the *nonequilibrium* spin of semiconductor electrons is used either for detecting the FM [2–4, 6] or for controlling the ferromagnetism [8, 9]. For a successful operation of such devices, an electron of the semiconductor must possess a long spin memory time and a macroscopic spin diffusion length, which is possible only at low temperatures [3, 4, 10]. At the same time, for an optical control of ferromagnetism, the aforementioned nonequilibrium spin *is not necessary* [7, 11], which offers promise for high-temperature applications of spintronics.

This paper shows that, in the absence of an external magnetic field, the exchange coupling of the spin systems of an FM and a semiconductor quantum well (QW) provides the possibility to electrically control the orientation of magnetization of the FM. In this case, the average spin of charge carriers (holes in the example under consideration) in the semiconductor is in the state of thermodynamic equilibrium. The strongly anisotropic exchange interaction between holes in the QW and magnetic atoms of the FM gives rise to an orientational transition: magnetization **M** is rotated from the plane of the structure toward the normal direction. In their turn, holes in the QW become spin polarized, thereby providing the stability of such a configuration. The orientation of the vector **M** is controlled by the variation of the hole concentration (and, hence, their spin density) in the QW, which is accomplished by applying a bias voltage to the gate of the structure. The normal component of the vector **M** can be inverted by applying the gate voltage V_G in the form of π pulses (analogue of the π pulse in magnetic resonance). This creates a fundamentally different approach to the design of spintronic devices: the direction of the magnetic moment of an FM is controlled via the electric (rather than optical [8, 9]) modulation of the exchange coupling of the FM with a semiconductor.

The physical meaning of the effect of orientational transition can be understood from Fig. 1. A ferromagnetic film with a magnetization **M** covers a semiconductor heterostructure consisting of a quantum well, which is separated from the ferromagnetic film and from the underlying nonmagnetic metal by barriers.

The nonmagnetic metal gate capping the structure is designed for the control of hole concentration (density of hole gas, DHG) in the QW. In the absence of exchange interaction between holes in the QW and magnetic atoms in the FM, the easy magnetization direction in the FM coincides with the x axis. In addition, it is assumed that the spin–orbit splitting of heavy and light holes is large and, hence, the spin of the QW holes is rigidly bound to the normal direction [12]. If the barrier between FM and QW is impermeable, the spin systems of FM and QW are uncoupled. In this case, the FM magnetization lies in the plane of the structure and is parallel to the x axis, while the hole gas in the QW is not spin polarized (the external magnetic field is zero). However, if the barrier is semitransparent, the wave functions of heavy holes and magnetic atoms of the FM overlap and an exchange interaction arises between holes and magnetic atoms. Since the hole spin is rigidly bound to the normal, this interaction is proportional to the product of the hole-spin and vector **M** z components. As the exchange interaction increases, a spontaneous spin polarization of holes becomes favorable (Fig. 1). In turn, the polarized holes rotate the vector **M** from the plane toward the normal direction [13]. The energy of the configuration shown in Fig. 1 does not change if the polarization directions of holes and vector **M** are simultaneously inverted. Therefore, one can say that the new axis, along which vector **M** becomes oriented is a bi-directional axis; i.e., it is analogous to the easy magnetization axis. This is an equilibrium configuration, which can be calculated from the condition for free-energy minimum in the system. At low temperature, this energy is close to that of the FM/QW system [14]. The energy density, i.e., energy per unit surface area of the system, includes: (i) the magnetic anisotropy energy [15] $E_A = -\beta m_x^2/2$ of the ferromagnet [16], where $\beta > 0$ is the magnetic anisotropy constant and m_x is the projection of the unit vector **m** along **M** onto the x axis of easy magnetization; (ii) the energy $E_{exc} = -Jnm_zp/2$ of exchange coupling of the FM magnetic atoms with the QW holes [8, 13], where J is the exchange interaction constant between holes with concentration n and polarization $p = (n_{+3/2} - n_{-3/2})/(n_{+3/2} + n_{-3/2})$ and magnetic atoms whose magnetic moment has a component m_z along the normal ($n_{\pm 3/2}$ is the concentrations of holes whose moments have projections $\pm 3/2$ on the z axis). The value of the constant J depends on the properties of the FM contacting the QW, as well as on the transmittance of the barrier between the FM and the QW, and is a phenomenological parameter of the problem. The exchange interaction will be strongly anisotropic if the splitting energy Δ of heavy and light holes in the QW is greater than the exchange J and kinetic energy μ of the hole motion in the QW plane (only the heavy hole subband is filled); and (iii) the additional energy $E_f = n^2p^2/2g$ of a Fermi gas of heavy holes associated with their spin polarization. The density of states g may differ from the two-dimensional density $m_h/\pi\hbar^2$ (m_h is the mass of a heavy hole in the QW plane) because of the effect of interaction between holes and the effect of particle exchange between FM and QW. In the framework of the simplest model, we assume that g is independent of hole concentration and is equal to the two-dimensional density. Then, the total energy per unit surface area is

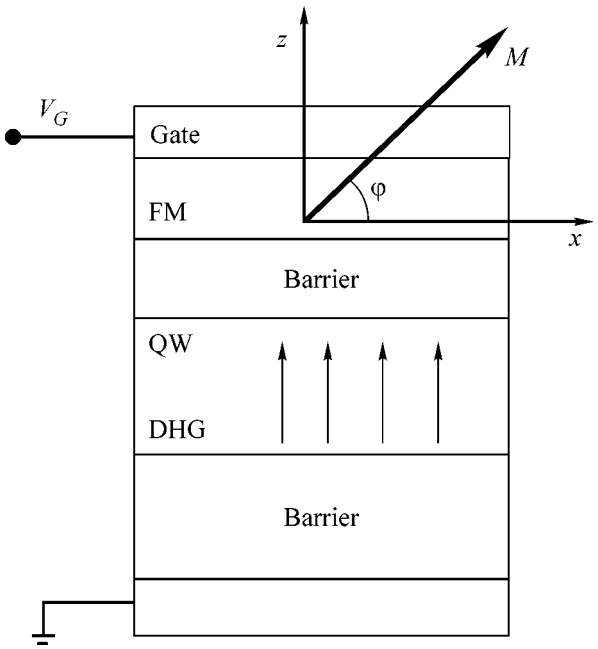

Fig. 1. Schematic diagram of the structure operating on the basis of the proximity effect. A semitransparent barrier separates the FM from the QW which, in turn, is separated by a barrier from the nonmagnetic metal contact. The metal gate on top of the structure serves for controlling the hole concentration in the QW. The arrows in the QW indicate the orientation of the hole spin.

$$\varepsilon = -(\beta m_x^2/2) - (Jnm_zp/2) + (n^2p^2/2g). \quad (1)$$

If the components of **m** are represented as $m_x = \cos(\varphi)$ and $m_z = \sin(\varphi)$ (the angle φ is measured from the plane of the structure), the necessary conditions of an extremum, i.e., $\partial\varepsilon/\partial\varphi = 0$ and $\partial\varepsilon/\partial p = 0$, are satisfied for

$$m_z = \sin(\varphi) = \frac{Jnp}{2\beta}, \quad p = \frac{Jp}{2n}\sin(\varphi);$$
$$m_z = +1, \quad p = \frac{Jp}{2n}; \quad m_z = -1, \quad p = -\frac{Jp}{2n}. \quad (2)$$

An analysis of the characteristic equation of quadratic form shows that the first pair (m_z, p) from Eqs. (2) realizes a minimum at the point $m_z = p = 0$ for the values of the FM–QW coupling parameter $K \equiv J^2h/4\beta < 1$. For $K > 1$ the minimum disappears. However, in this case, a minimum is realized for the second and third pairs of solutions (2) corresponding to the same energy. Since the magnitude of hole polarization cannot exceed unity, the second and third pairs of solutions is meaningful at

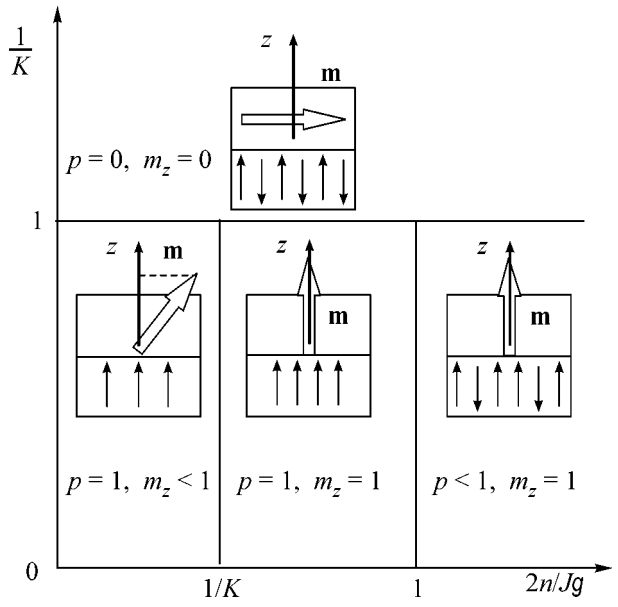

Fig. 2. Diagram of different configurations in the FM/QW system depending on the hole concentration (the abscissa axis) and the reciprocal coupling parameter (the ordinate axis).

high hole concentrations $n > Jg/2$. As the concentration decreases, the hole polarization becomes equal to its limiting value. Therefore, in the low-concentration region, one should seek for the minimal value of energy (1) as a function of angle φ with the additional condition of $p = 1$ [17]. Substituting it into Eq. (1), we arrive at the necessary condition for an extremum in the concentration region $n < Jg/2$:

$$m_z = \sin(\varphi) = \frac{Jn}{2\beta} = K\frac{2n}{Jg}. \quad (3)$$

Since $|m_z| < 1$, the minimum is realized for $n < Jg/2K < Jg/2$. In this region, the z component of magnetization grows linearly with concentration and reaches unity at $n = Jg/2K$; in the region $Jg/2 > n > Jg/2K$, it is equal to unity. The results obtained above allow a simple interpretation. If the exchange interaction between holes in the QW and magnetic atoms of the FM is small ($K < 1$), the magnetization lies in the plane of the structure along the easy axis while the hole gas is nonpolarized at any concentration (the upper part of Fig. 2). The situation changes when the coupling between the FM and the semiconductor is strong ($K > 1$, the lower part of Fig. 2). In the region $n < Jg/2K$, the number of holes is insufficient for magnetizing the FM across the plane while the z component of magnetization linearly increases with concentration and is equal to unity when $n \geq Jg/2K$. Holes are completely spin polarized up to $n = Jg/2K$ (this concentration corresponds to the equality of the exchange splitting of holes to twice their Fermi energy, i.e., $J = 2\mu$). At high concentrations, the hole polarization decreases, because the energy difference between spin subbands of heavy holes is smaller than 2μ. At the same time, the energy of the exchange coupling of the FM with the QW is determined by the hole polarization density $\Sigma \equiv np = Jg/2$, which is constant in this region.

The orientation of **M** can be controlled by varying the hole concentration in the QW by way of applying a bias voltage to the gate of the structure (Fig. 1). A similar situation was realized [18] in an InMnAs ferromagnet whose hysteresis loop was varied by applying a gate voltage V_G. The phenomenon was attributed by the authors to the small change in T_c that accompanied the change in the hole concentration *inside* the InMnAs structure. However, this structure had a thin (5 nm) nonmagnetic InAs layer near the ferromagnet [18], the existence of this layer being very important for controlling the FM [19]. If we assume that the voltage V_G changes the number of holes in the InAs layer, the results reported in [18, 19] can be explained in the framework of the model considered above. When $V_G < 0$, the holes fill InAs and the easy axis is oriented along the normal, which leads to a hysteresis in a magnetic field parallel to the normal. If the holes leave InAs ($V_G > 0$), the easy axis lies in the plane of the structure and the magnetization across the easy axis exhibits a nonhysteretic behavior. To verify this hypothesis, it is necessary to measure the orientation of **M** (rather than its z component [18, 19]).

Let us estimate the coupling parameter $K \equiv J^2g/4\beta$ for a $Zn_{1-x}Cr_xTe$ high-temperature ferromagnetic semiconductor ($x = 0.2$, $T_c = 300$ K [20]). The magnetic anisotropy constant can be estimated by the formula $\beta = 4\pi M^2 d$ [16] on the assumption that it originates from magnetostatic energy (easy-plane anisotropy). The concentration of magnetic atoms is $N = xN_0 \approx 3.5 \times 10^{21}$ cm^{-3} (the anion concentration N_0 is determined by the ZnTe lattice constant $a_0 = 6.1$ Å [21]). The magnetic moment per one Cr ion is equal to ≈2 Bohr magnetons at $T \approx 200$ K [20]. Then, the magnetization is $M \approx 65$ G and the anisotropy constant is $\beta = 0.027$ Erg/cm^2 for a 5 nm thick film [22]. If the QW is grown on the basis of CdTe, the coupling parameter is greater than unity when $J > 25$ meV ($m_h = 0.25m_0$ [23]). Under these conditions, the hole concentration at which the magnetization is oriented across the plane of the structure is $n = Jg/2K = 2\beta/J < 10^{12}$ cm^{-2}. The p–d exchange constant in ZnCrTe is approximately equal to 4 eV [21]. Therefore, the maximal splitting (≈0.8 eV at $x = 0.2$) is more than 30 times greater than the required value of J. The value of J can be fitted by varying the overlapping of the wave functions of holes in the QW and magnetic atoms in the FM via the variation of the QW parameters.

As noted above, in the low-concentration region $n < Jg/2K$, the magnetization does not lie in the plane and makes an angle φ with the x axis. In equilibrium, the magnetic moment is oriented along the effective mag-

netic field $\mathbf{H}_{\text{eff}} = -\partial\varepsilon/\partial\mathbf{M}_s$ [24], where the energy (in the case under consideration, per unit surface area) is given by Eq. (1) and $\mathbf{M}_s = \mathbf{M}d$ is the magnetic moment per unit surface area. The x component of the field, $H^x_{\text{eff}} \equiv |\mathbf{H}_A| = \beta m_x/Md$, represents the anisotropy field $\mathbf{H}_A$ while the z component, $H^z_{\text{eff}} \equiv |\mathbf{H}_{\text{exch}}| = Jn/2Md = \beta m_z/Md$, is the anisotropic exchange field $\mathbf{H}_{\text{exch}}$ acting on the FM from the side of the holes of the QW. The latter expression was derived with allowance for Eq. (3) and for the fact that the hole polarization is $p = 1$. The equilibrium situation is illustrated in Fig. 3a. Assume that the field $|\mathbf{H}_{\text{exch}}|$ jumps to zero. Then, the magnetic moment performs a coherent rotation about the anisotropy field according to the equation $d\mathbf{m}/dt = \gamma\mathbf{H}_{\text{eff}} \times \mathbf{m}$ [24] with a precession period of $T = 2\pi/\gamma|\mathbf{H}_A| = 2\pi Md/\gamma\beta m_z$ (γ is the gyromagnetic ratio). Within a time of $\tau = T/2$, the z component of magnetization is inverted (Fig. 3b). If, at this instant, the exchange coupling between FM and QW is reestablished, the equilibrium state will be the state with the inverted m_z component. Indeed, if the spin relaxation time of holes is small, the polarization of holes and the exchange field $\mathbf{H}_{\text{exch}}$ change their sign at the end of the pulse, and the magnetization becomes again oriented along the total effective magnetic field. Hence, the FM/QW spin system is in the second stable state with inverted m_z and p. The requirement that the spin relaxation be fast is easily satisfied for holes at high temperatures [5]. The field $\mathbf{H}_{\text{exch}}$ can be switched off by supplying pulsed voltage V_G to the gate (Fig. 1). When a pulse of $V_G > 0$ is applied in the interval from 0 to $\tau = T/2$, the QW is depleted of holes, and the field is $|\mathbf{H}_{\text{exch}}| = 0$. The precession period can be controlled by tuning the x component of magnetization through the variation of the hole concentration in the QW before supplying the pulse. For example, if $m_x = 1/4$, then, at $\beta = 4\pi M^2 d$, we have $\tau = 1/\gamma M \approx 1$ ns. For a coherent rotation of magnetization, it is necessary that the damping parameter λ in the Landau–Lifshits dynamic equation [24] be smaller than the reciprocal period of Larmor precession in the effective magnetic field, $1/T = 5 \times 10^5$ Hz. For a $Zn_{1-x}Cr_xTe$ semiconductor, the parameter λ is unknown but one can expect that it is fairly small (e.g., in a nickel ferrite, $\lambda \approx 10^7$–10^8 Hz [25] and the characteristic relaxation time of magnetization is 10–100 ns). For the inversion of m_z, it is not necessary to use rectangular pulses with sharp edges. It is sufficient to apply a smooth pulse with a duration of $t \approx T/2$ [26].

Thus, in an FM/QW hybrid system, the exchange interaction between holes in the QW and magnetic atoms of the adjacent FM causes an orientational transition, which consists in the rotation of magnetization from the plane of the structure toward the normal direction. This effect makes it possible to electrically control the orientation of magnetization in the FM.

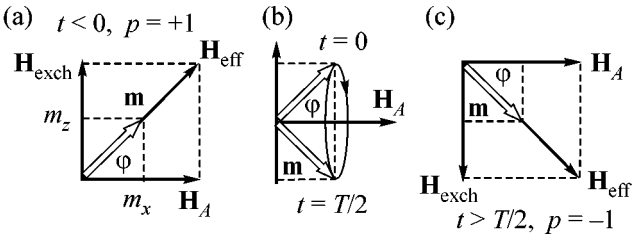

Fig. 3. Control over the orientation of vector **m** with a pulsed variation of the hole polarization density in the QW: (a) before the pulse is supplied, a stable equilibrium occurs for $m_z > 0$ and $p = +1$; (b) during the time interval $[0, T/2]$, a free precession of vector **M** about the anisotropy field $\mathbf{H}_A$ takes place; and (c) after the end of the pulse, the system is in the second stable state with inverted values of m_z and p.

I am grateful to K.V. Kavokin and I.A. Merkulov for discussions. This work was supported by the Russian Foundation for Basic Research and the Civil Research and Development Foundation.

REFERENCES

1. G. A. Prinz, Science **250**, 1092 (1990); Phys. Today **48**, 58 (1995).
2. S. A. Wolf, D. D. Awschalom, R. A. Buhrman, *et al.*, Science **294**, 1488 (2001).
3. R. I. Dzhioev, B. P. Zakharchenya, P. A. Ivanov, and V. L. Korenev, Pis'ma Zh. Éksp. Teor. Fiz. **60**, 650 (1994) [JETP Lett. **60**, 661 (1994)].
4. R. I. Dzhioev, B. P. Zakharchenya, and V. L. Korenev, Fiz. Tverd. Tela (St. Petersburg) **37**, 3510 (1995) [Phys. Solid State **37**, 1929 (1995)].
5. *Optical Orientation*, Ed. by F. Meier and B. P. Zakharchenya (North-Holland, Amsterdam, 1984; Nauka, Leningrad, 1989).
6. S. F. Alvarado and P. Renaud, Phys. Rev. Lett. **68**, 1387 (1992).
7. V. L. Korenev, Fiz. Tverd. Tela (St. Petersburg) **38**, 910 (1996) [Phys. Solid State **38**, 502 (1996)].
8. V. L. Korenev, Solid State Commun. **102**, 13 (1997).
9. A. Oiwa, Y. Mitsumori, R. Moriya, *et al.*, Phys. Rev. Lett. **88**, 137202 (2002).
10. C. Weisbuch, PhD Thesis (1977); V. L. Vekua, in *Proceedings of V Republic Colloquium on Optics and Spectroscopy of Semiconductors and Dielectrics, Sukhumi* (1984), p. 124; R. I. Dzhioev, B. P. Zakharchenya, V. L. Korenev, and M. N. Stepanova, Fiz. Tverd. Tela (St. Petersburg) **39**, 1975 (1997) [Phys. Solid State **39**, 1765 (1997)].
11. I. A. Merkulov and G. G. Samsonidze, Fiz. Tverd. Tela (Leningrad) **22**, 2437 (1980) [Sov. Phys. Solid State **22**, 1419 (1980)].
12. Spin–orbit interaction in combination with dimensional quantization causes splitting Δ of heavy ($\pm 3/2$) and light ($\pm 1/2$) hole subbands in the quantum well (P. Y. Yu and M. Cardona, *Fundamentals of Semiconductors* (Springer, Berlin, 1996)). The ground state corresponds to heavy holes with momentum projections of +3/2 and –3/2 on

the axis of the structure growth. If the characteristic value of J for the exchange interaction that mixes heavy and light holes is smaller than Δ, the moment projections of +3/2 and –3/2 are good quantum numbers (the exchange interaction has no matrix elements between the +3/2 and –3/2 states). In this sense, the hole spin is rigidly bound to the direction of the structure growth. Therefore, when writing spin Hamiltonian (1), it is possible to limit the consideration to a two-level system of +3/2 and –3/2 of the hole ground state while the exchange interaction terms that change the hole spin by unity can be neglected.

13. A similar problem for a semimagnetic quantum well containing Mn ions in the paramagnetic phase (but in an external magnetic field) was considered in: I. A. Merkulov and K. V. Kavokin, Phys. Rev. B **52**, 1751 (1995); I. A. Merkulov, D. R. Yakovlev, K. V. Kavokin, *et al.*, Fiz. Tverd. Tela (St. Petersburg) **39**, 2079 (1997) [Phys. Solid State **39**, 1859 (1997)]; K. V. Kavokin, Phys. Rev. B **59**, 9822 (1999).
14. The temperature must be small compared to T_C, Fermi energy μ, and constant J. However, in absolute units, T may be great, and the results obtained above can be used for estimations up to 100–200 K.
15. L. D. Landau and E. M. Lifshitz, *Course of Theoretical Physics*, Vol. 8: *Electrodynamics of Continuous Media*, 3rd ed. (Nauka, Moscow, 1992; Pergamon, New York, 1984). In this case, we ignore the energy of inhomogeneity by assuming that the film thickness d is much smaller than the domain wall thickness, so that the magnetization rotates uniformly and the exchange energy of the FM remains unchanged.
16. If the magnetostatic energy $2\pi M^2 m_z^2$ is included in the consideration, the quantity β in the final result should be replaced by $\beta + 4\pi M^2$.
17. For definiteness, we consider the state with positive p and m_z. The second state is obtained by the sign inversion of p and m_z. In addition, we assume that $J > 0$, which favors a parallel orientation of magnetization and hole polarization, i.e., an antiferromagnetic interaction between hole spins and magnetic atoms. A generalization to the case of ferromagnetic interaction presents no special problems.
18. H. Ohno, D. Chiba, F. Matsukura, *et al.*, Nature **408**, 944 (2000).
19. F. Matsukura, D. Chiba, T. Omiya, *et al.*, Physica E (Amsterdam) **12**, 351 (2002).
20. H. Saito, V. Zayets, S. Yamagata, and K. Ando, Phys. Rev. Lett. **90**, 207202 (2003).
21. T. Dietl, H. Ohno, and F. Matsukura, Phys. Rev. B **63**, 195205 (2001).
22. In this case, the exchange energy density of the FM itself is $\alpha \gg \beta$ ($\alpha \approx T_c N d \approx 70$ erg/cm^2), so that the Curie temperature variation is small: $\Delta T_c/T_c \sim J^2 g/\alpha \sim 0.1\%$. The exchange interaction of the FM and QW spin systems overcomes only the energy of magnetic anisotropy of the FM, which is caused by weak relativistic interactions.
23. G. Fishman, Phys. Rev. B **52**, 11132 (1995).
24. L. D. Landau and E. M. Lifshitz, Phys. Z. Sowjetunion **8**, 153 (1935).
25. S. Chikasumi, *Physics of Ferromagnetism. Magnetic Characteristics and Engineering Application* (Syokabo, Tokyo, 1984; Mir, Moscow, 1987), Vol. 2.
26. H. W. Schumacher, C. Chappert, R. C. Sousa, *et al.*, Phys. Rev. Lett. **90**, 017204 (2003).

Translated by E. Golyamina

JETP Letters, Vol. 78, No. 9, 2003, pp. 569–573. Translated from Pis'ma v Zhurnal Éksperimental'noĭ i Teoreticheskoĭ Fiziki, Vol. 78, No. 9, 2003, pp. 1058–1062.

New Magnetic States in Copper Metaborate CuB_2O_4

A. I. Pankrats[1, *], G. A. Petrakovskii[1], M. A. Popov[1], K. A. Sablina[1], L. A. Prozorova[2], S. S. Sosin[2], G. Szimczak[3], R. Szimczak[3], and M. Baran[3]

[1] *Kirenskiĭ Institute of Physics, Siberian Division, Russian Academy of Sciences, Akademgorodok, Krasnoyarsk, 660036 Russia*

**e-mail: pank@iph.krasn.ru*

[2] *Kapitza Institute for Physical Problems, Russian Academy of Sciences, ul. Kosygina 2, Moscow, 117334 Russia*

[3] *Institute of Physics, Polish Academy of Sciences, 02-668 Warsaw, Poland*

Received September 26, 2003

The static and resonance properties of copper metaborate CuB_2O_4 were experimentally studied in a magnetic field applied in the crystal tetragonal plane. The field-induced second-order phase transition to a weakly ferromagnetic state was observed in the temperature range 10–20 K. The low-field state is characterized by the absence of spontaneous moment, and it represents, presumably, a long-period helicoid. At temperatures below 2 K, two sequential first-order phase transitions were observed. They were accompanied by jumps in resonance absorption with a hysteresis upon changing field-scan direction. These transitions can be caused by the transformation of the incommensurate spin structure into the helicoidal states with periods commensurate with the lattice translation period. © *2003 MAIK "Nauka/Interperiodica".*

PACS numbers: 75.50.Cc; 75.30.Kz; 75.60.Ej; 76.50.+g

1. INTRODUCTION

The tetragonal copper metaborate crystal CuB_2O_4 belongs to the family of copper oxides whose intense research was stimulated by the discovery of high-temperature superconductivity. In the early works devoted to the magnetic properties of a CuB_2O_4 single crystal [1], it was found that, in the temperature range from 10 K to the Néel temperature $T_N = 20$ K, this compound is a weak ferromagnet, in which the magnetic moments of sublattices and the spontaneous magnetic moment lie in the tetragonal crystal plane. Upon a decrease in temperature, an abrupt decrease in magnetization was observed near $T = 10$ K, indicating the transition to a new magnetic phase. The resonance studies [2] showed that, although the magnetic moments of copper ions remain in the basal crystal plane, the spontaneous moment disappears. It was conjectured in the cited work that the low-temperature magnetic state of CuB_2O_4 can be helicoidal. Neutron inelastic scattering studies [3] showed that, in the absence of a magnetic field, an incommensurate magnetic state of the type of magnetic soliton lattice with the structure wave vector oriented along the tetragonal axis is established below 10 K. The magnetic resonance [2] and magnetostatic [4] studies in a magnetic field applied in the crystal tetragonal plane showed that, in the temperature range $T <$ 10 K, the modulated magnetic structure transforms into a weakly ferromagnetic state with a magnetic moment lying in the same plane. The temperature dependence of the interface separating these two states was obtained and subsequently confirmed by neutron diffraction measurements [5]. Analysis of the field dependences of magnetization [4] allowed the assumption to be made [6] that the weakly ferromagnetic state is induced in the temperature range 10–20 K by the magnetic field and transforms into a new magnetic state with zero spontaneous magnetic moment upon lowering the field. The purpose of this work was to study the assumed phase transition by the magnetic resonance method, which is one of the most sensitive to the magnetic state of a substance, and by the magnetostatic measurements. It was also of interest to carry out magnetic resonance studies at temperatures $T < 2$ K, where the anomalies were observed in the neutron elastic scattering and μSR data [7].

2. SAMPLES AND EXPERIMENTAL METHOD

Single-crystal samples of copper metaborate CuB_2O_4 were grown by the spontaneous crystallization method [8]. Since the critical magnetic fields of the assumed phase transition are rather low (less than 800 Oe), the resonance measurements should be performed in the frequency range 3–6 GHz. For this purpose, a spectrometer of the transmission type with a quasi-toroidal cavity was used (for details, see [9]). The cavity operating frequency was tuned using accessory quartz plates of different size, which were placed in a node of electric field. The static magnetic field was created by a superconducting solenoid. Single crystal CuB_2O_4 of size $1.2 \times 1.8 \times 2.8$ mm was placed in a node of magnetic field so that the static field was oriented in the [110] direction of the basal plane, while the perpen-

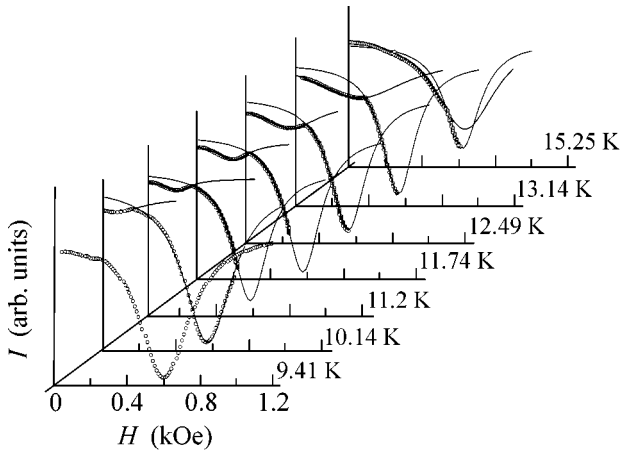

Fig. 1. Resonance absorption spectra of CuB_2O_4 at $T >$ 10 K and a frequency of 3.48 GHz. Dots are the experimental data and solid lines are the Lorentzian fits.

dicular microwave magnetic field was directed along the tetragonal axis C_4. Magnetostatic measurements were performed on an MPMS-5 SQUID magnetometer.

3. EXPERIMENTAL RESULTS

The examples of resonance absorption spectra recorded with a magnetic field scan at frequency ν = 3.48 GHz are presented in Fig. 1 for various temperatures above 9 K. At T = 9.4 K, a single high-intensity resonance line with a width of about 300 Oe is observed at a resonance field of 600 Oe. As the temperature increases, an additional low-intensity line appears at low fields starting with $T \simeq 9.5$ K. With an increase in temperature, this line rapidly shifts to higher fields, and its amplitude and width increase. The solid lines in the figure are fits of the Lorentzian curves to the experimental points. Similar transformation of the resonance spectrum is observed at frequency ν = 5.15 GHz, but the additional line now appears at temperatures above 12.6 K. In all spectra, kink points can be set off in the field $H = H_{c_\perp}$, where one absorption line changes to the other. Magnetic hysteresis upon changing the scan direction was not observed.

The curves for the field dependence of magnetization at temperatures 10, 11, and 14 K in a magnetic field applied in the [110] direction of the tetragonal plane are shown in Fig. 2. These curves were recorded in the interval from 0 to ±1000 Oe with the back and forth field scans. They are symmetric about the origin of coordinates and do not show magnetic hysteresis. At all temperatures, the curves for magnetization field dependence have a kink point coinciding with the kink points in the resonance absorption spectra. The kink points $H_{c_\perp}$ separate these curves into two parts. The initial portions of the curves emanate from the origin of coordinates and are nonlinear, with the degree of nonlinearity decreasing upon elevation of temperature. At $H > H_{c_\perp}$, the dependences become nonlinear and can be represented as $m(H) = m_0 + \chi H$, where m_0 is the spontaneous magnetic moment and χ is magnetic susceptibility. The curves measured in a field directed along [100] is qualitatively analogous to the curves measured for a [110]-directed field.

Magnetic resonance at temperatures below 4.2 K was studied at a frequency of 5.15 GHz. As the temperature decreased down to $T \simeq 2$ K, a single smooth absorption line with a width of about 900 Oe was observed. Upon further decrease in temperature, weak

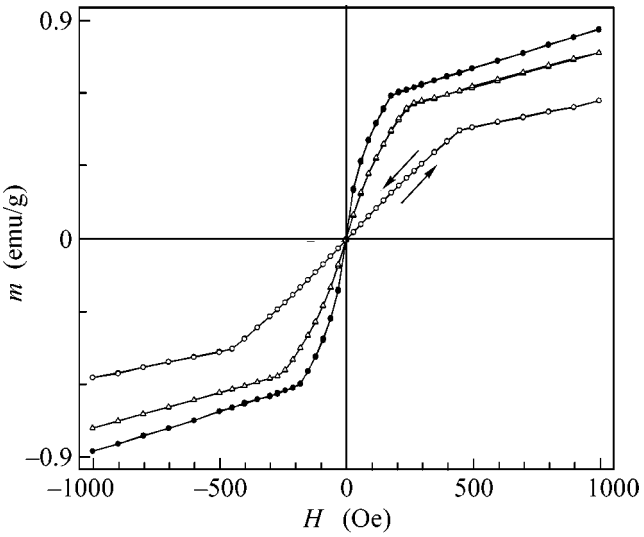

Fig. 2. Magnetization as a function of magnetic field applied in the [110] direction at temperatures of 10, 11, and 14 K.

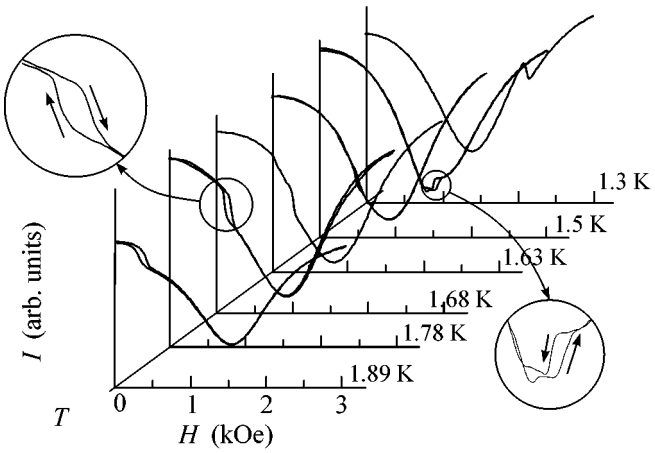

Fig. 3. Resonance absorption spectra of CuB_2O_4 in a low-temperature range at a frequency of 5.15 GHz.

features appeared in the absorption spectrum (Fig. 3). At T = 1.89 K, a step appears at the left wing of resonance line in the field H_{c_1}, and it demonstrates a hysteresis upon the back and forth field scans. With lowering the temperature of the sample, this step shifts to higher fields, while another step of the same form appears at low fields at H_{c_2}. As the temperature further decreases, both steps undergo upfield shift with a decrease in the distance between them, and they virtually merge into a single continuous transition at T = 1.3 K.

4. DISCUSSION

An analysis of the experimental data presented in Fig. 1 and a comparison with the results of Lorentzian curve fitting allow one to assert that the absorption spectrum in the temperature range 10–20 K is not a sum of two lines but consists of two single lines that change each other in the field $H = H_{c_\perp}$. Therefore, $H_{c_\perp}$ is the phase-transition field, and the fragments of resonance lines observed at $H < H_{c_\perp}$ and $H > H_{c_\perp}$ belong to the different states. The conclusion about the phase transition is confirmed by the analysis of the magnetization field dependences measured in the [100] and [110] directions. The magnetostatic properties will be discussed in detail elsewhere; in this work, we will focus only on the results concerning the phase diagram. As was pointed out above, for all temperature in the range 10–20 K, the field $H_{c_\perp}$ separates the curve for the magnetization field dependence into two parts, with its initial portion emanating from the origin of coordinates. Consequently, this field corresponds to the phase transition from the state with zero spontaneous moment to a weakly ferromagnetic state. The temperature dependence of the critical field was reproduced from the data of resonance and static experiments (boundary between states *2* and *3* in the phase diagram in Fig. 4). With an increase in temperature, $H_{c_\perp}$ first increases and then decreases as T_N is approached. The resonance and static data for the [110] direction well correlate with each other. The $H_{c_\perp}(T)$ curve for the [100] direction goes slightly lower, but the anisotropy in the tetragonal plane is small. The absence of magnetic hysteresis in the transition region for both static and resonance data and the continuous (without jumps in absorption) transformation of one resonance line to the other are evidence of the second-order phase transition.

To elucidate the nature of low-field state, it is necessary to analyze the field-and-frequency dependence of magnetic resonance in both phases at $T \simeq 13.1$ K (Fig. 5). The curve for the high-field phase was constructed using our data and the data of [2], which are

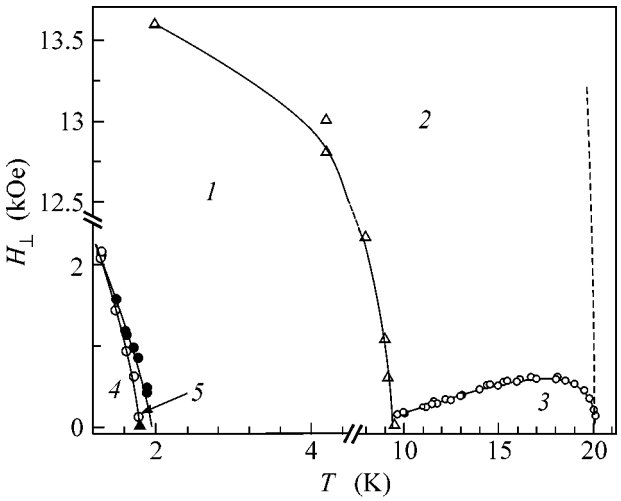

Fig. 4. Phase diagram of CuB_2O_4 in a magnetic field perpendicular to the tetragonal axis; circles are for the results of resonance and magnetostatic measurements, △ are the data from [2, 4], ▲ are the neutron diffraction results [7], solid lines are drawn for clarity, and the dotted line is the line of transition to the paramagnetic state.

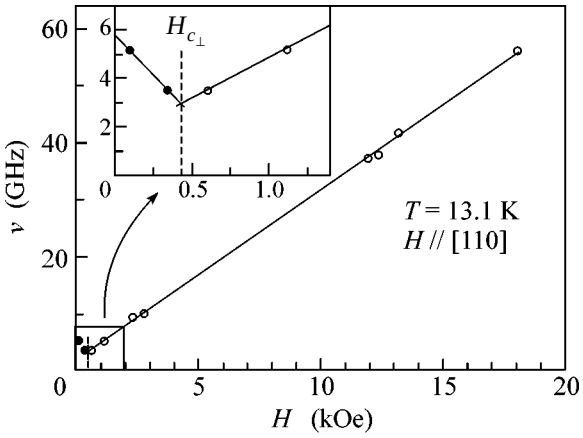

Fig. 5. Field-and-frequency dependences for the high- and low-field states at $T \simeq 13.1$ K; solid line is drawn according to Eq. (1).

well described by the corresponding dependence for a weak ferromagnet:

$$\nu^2 = \gamma^2 H(H + H_D) + \Delta^2, \qquad (1)$$

where H_D and Δ are the Dzyaloshinski field and the energy gap, respectively. The solid line in Fig. 5 corresponds to dependence (1) with the parameters H_D = (1.6 ± 0.4) kOe and Δ = (1.5 ± 1) GHz. The relatively low accuracy of determining these parameters is caused by the poor temperature stability in these measurements. At $H < H_{c_\perp}$, this dependence can be analyzed only qualitatively, because measurements were made

only for two frequencies. Nevertheless, one can firmly state that the resonance frequency in this phase decreases with an increasing magnetic field. An analogous dependence can occur in the presence of tetragonal anisotropy in an easy plane or if C_4 is the easy magnetic axis. In the first case, the critical field $H_{c_\perp}$ can be interpreted as a turnover field in the basal plane and, in the second, as a field at which the smooth reorientation of antiferromagnetic vector from the $\mathbf{L} \parallel C_4$ to the $\mathbf{L} \perp C_4$ position is completed, as a result of which a weak ferromagnetic moment increases linearly with field. However, these variants are inconsistent with the magnetostatic measurements of this work and of [4], and, hence, the observed phase transition is caused by different reasons. It is conceivable that the observed magnetic resonance spectrum is caused by the existence of a modulated (commensurate or incommensurate) state in the low-field phase. With an increase in magnetic field, the translation period λ of this structure increases [10] and the dispersion curve $\omega(k)$ splits into the phason and acoustic branches at the boundary $q_0 = \pi/\lambda$ of the "first Brillouin zone" [11]. Inasmuch as a uniform microwave field can excite magnons with $k = 2q_0$ corresponding to zero-quasimomentum transfer in a spin structure with long-wave modulation, the magnetic resonance spectrum should display a branch which has zero-field gap $\omega(2q_0)/(2\pi)$ and smoothly changes to the corresponding branch of the commensurate phase in the vicinity of critical field $H_{c_\perp}$.

This assumption also enables one to explain why the spontaneous magnetic moment is zero and the field-dependence curve for magnetization has a kink at $H = H_{c_\perp}$. The helicoidal spatial distribution averages out the local weak ferromagnetic moments at $H = 0$. Due to the distortion of ideal helicoid by a magnetic field, the moments are reoriented along the field and, simultaneously, the antiferromagnetic susceptibility increases, and both processes are completed upon the transition to the commensurate weakly ferromagnetic state. The absence of zero-field splitting (typical of modulated structures) of magnetic peaks in the neutron diffraction patterns at $T > 10$ K [3] may be caused by the fact that the modulation has a long period and its wave vector is, likely, much smaller than the experimental resolution.

Let us now consider the resonance properties in the low-temperature region. The absorption step observed in the resonance spectrum at 1.89 K correlates with the jump in intensity of magnetic satellites in the neutron diffraction pattern at $T \simeq 1.8$ K [7] and allows one to assume that it is caused by the magnetic phase transition. At even lower temperatures, one more jump in absorption appears in the resonance lines at $H_{c_1} < H_{c_2}$. The presence of hysteresis for both jumps upon the back and forth field scans allows the conclusion to be drawn that the phase transitions at H_{c_1} and H_{c_2} are first-order transitions. The temperature dependences for both critical fields are shown in the phase diagram (Fig. 4). As compared to the published phase diagrams [2, 4, 5] containing incommensurate 1 and weakly ferromagnetic 2 states, new states 3, 4, and 5 are added in the diagram in Fig. 4. State 3 appears in the temperature range 10–20 K and, most probably, is a long-period modulated state [12]. When analyzing states 4 and 5, one should take into account that, according to the neutron diffraction data [7, 13], the magnetic structure remains modulated down to a temperature of 200 mK. One can assume that the transition observed in the neutron diffraction experiment at $T \simeq 1.8$ K is a lock-in transition from the incommensurate phase to the modulated state with a wave vector commensurate with the lattice translation period [14]. In the phase diagram, this corresponds to the transition from state 1 to state 5. In this case, the wave vector in the commensurate state can take values $k_{mn} = (2\pi/c)(m/n)$, where c is the lattice constant and m and n are mutually prime numbers. Since the resonance lines for states 4 and 5 differ only slightly, one can assume that they (as well as the new states observed upon further decrease in temperature in the range $T \simeq 1$ K [13]) differ only in the numbers m and n. This signifies that the cascade of transitions at $T < 2$ K represents a so-called "devil staircase" of transitions between the commensurate states.

5. CONCLUSIONS

The magnetic phase diagram of copper metaborate CuB_2O_4 in a magnetic field lying in the tetragonal crystal plane has been studied in detail in this work. Analysis of the obtained static and resonance data enables one to assume that the magnetic state in the temperature range 10–20 K forms a helicoidal long-period structure. It has been established that, in magnetic fields below 1 kOe, this state transforms into a weakly ferromagnetic state that is not spontaneous at all temperatures below T_N, but is induced by a magnetic field. At low temperatures $T < 2$ K, two sequential close-spaced first-order phase transitions have been observed. These are presumably transitions to the modulated states with different magnetic wave vectors that are commensurate with the lattice translation period.

We are grateful to V.I. Marchenko and M.E. Zhitomirskiĭ for helpful discussions. This work was supported by the Russian Foundation for Basic Research (project no. 03-02-16701) and the Ministry of Education of the Russian Federation (grant no. E02-3.4-227).

REFERENCES

1. G. Petrakovskii, D. Velikanov, A. Vorotinov, *et al.*, J. Magn. Magn. Mater. **205**, 105 (1999).
2. A. I. Pankrats, G. A. Petrakovskiĭ, and N. V. Volkov, Fiz. Tverd. Tela (St. Petersburg) **42**, 93 (2000) [Phys. Solid State **42**, 96 (2000)].
3. B. Roessli, J. Schefer, G. Petrakovskii, *et al.*, Phys. Rev. Lett. **86**, 1885 (2001).

4. G. A. Petrakovskiĭ, A. D. Balaev, and A. M. Vorotynov, Fiz. Tverd. Tela (St. Petersburg) **42**, 313 (2000) [Phys. Solid State **42**, 321 (2000)].
5. J. Schefer, M. Boehm, B. Roessli, *et al.*, Appl. Phys. A **74**, S1740 (2002).
6. G. A. Petrakovskiĭ, A. I. Pankrats, M. A. Popov, *et al.*, Fiz. Nizk. Temp. **28**, 840 (2002) [Low Temp. Phys. **28**, 606 (2002)].
7. M. Boehm, B. Roessli, J. Schefer, *et al.*, Physica B (Amsterdam) **318**, 277 (2002).
8. G. A. Petrakovskiĭ, K. A. Sablina, D. A. Velikanov, *et al.*, Kristallografiya **45**, 926 (2000) [Crystallogr. Rep. **45**, 853 (2000)].
9. L. A. Prozorova, S. S. Sosin, D. V. Efremov, and S. V. Petrov, Zh. Éksp. Teor. Fiz. **112**, 1893 (1997) [JETP **85**, 1035 (1997)].
10. I. E. Dzyaloshinskiĭ, Zh. Éksp. Teor. Fiz. **47**, 992 (1964) [Sov. Phys. JETP **20**, 665 (1964)].
11. W. L. McMillan, Phys. Rev. B **16**, 4655 (1977); V. L. Pokrovsky and A. L. Talapov, Sov. Phys. JETP **48**, 579 (1978).
12. G. A. Petrakovskiĭ, M. A. Popov, B. Roessli, and B. Ouladdiaf, Zh. Éksp. Teor. Fiz. **120**, 926 (2001) [JETP **93**, 809 (2001)].
13. M. Boehm, B. Roessli, J. Schefer, *et al.*, Phys. Rev. B **68**, 024405 (2003).
14. M. A. Popov, G. A. Petrakovskiĭ, and V. I. Zinenko, Fiz. Tverd. Tela (St. Petersburg) **46** (2004, in press).

Translated by V. Sakun

JETP Letters, Vol. 78, No. 9, 2003, pp. 574–577. Translated from Pis'ma v Zhurnal Éksperimental'noĭ i Teoreticheskoĭ Fiziki, Vol. 78, No. 9, 2003, pp. 1063–1067.

Thermodynamic Inequalities in a Superfluid

A. F. Andreev[1, 2, *] and L. A. Melnikovsky[1, **]

[1] *Kapitza Institute for Physical Problems, Russian Academy of Sciences, ul. Kosygina 2, Moscow, 119334 Russia*
**e-mail: andreev@kapitza.ras.ru*
[2] *Low Temperature Laboratory, Helsinki University of Technology, FIN-02015 HUT, Finland*
***e-mail: leva@kapitza.ras.ru*
Received October 3, 2003

General conditions for thermodynamic stability of a superfluid are studied in the full space of thermodynamic variables, including (along with the conventional thermodynamic coordinates such as pressure and temperature) superfluid motion velocity and momentum density. The stability conditions lead to the thermodynamic inequalities that replace the Landau superfluidity criterion at nonzero temperatures. © *2003 MAIK "Nauka/Interperiodica".*

PACS numbers: 67.40.Kh; 67.57.Bc

1. INTRODUCTION

The experimentally observed superfluidity breakdown is ordinarily associated with the vortex formation and occurs at velocities much lower than the Landau critical velocity. For this reason, one can restrict oneself only to the leading terms in the expansion of equations of superfluid dynamics in powers of low velocity.

However, there are experiments [1] that are devoted to studying the superfluid motion through narrow orifices. Under these conditions, the maximal velocity is a decreasing function of the orifice width and can achieve values on the order of Landau critical velocity for a sufficiently small orifice cross section. Therefore, all thermodynamic quantities become nontrivial functions of not-too-low velocities (i.e., they depend not only on the conventional thermodynamic variables such as pressure and temperature). With this general formulation, we make no assumptions about the smallness of velocity (but use only the fact that fluid at rest is isotropic) and determine the full set of thermodynamic inequalities, i.e., conditions imposed on the thermodynamic functions by the requirement for the stability of the superfluid state.

Using the phonon–roton model, we calculate the maximal velocity that is compatible with the obtained thermodynamic inequalities and demonstrate that it can be interpreted as the generalization of the Landau critical velocity to nonzero temperatures. This thermodynamic scenario for superfluidity breakdown probably occurs in experiments on critical velocities in narrow orifices.

2. STABILITY

When deriving general equations of superfluid dynamics, it is assumed [2] that every small element of fluid is in the local equilibrium, and this equilibrium is stable. For the state to be stable, it is necessary that it realize entropy maximum (at least, local) for a closed system. Instead of studying the conditions for entropy maximum, it is more suitable [3] to use the equivalent condition for energy minimum at a constant entropy and constant additive integrals of motion.

The total energy $E_{\rm tot}$ of the fluid can be represented as the integral $E_{\rm tot} = \int E\, d\mathbf{r}$ of energy density E over the entire volume. The energy density is obtained using the Galilean transformations

$$E = \frac{\rho v_{\rm s}^2}{2} + \mathbf{v}_{\rm s}\mathbf{j}_0 + E_0. \qquad (1)$$

Here, $\mathbf{v}_{\rm s}$ is the superfluid velocity, ρ is the mass density, and the index 0 denotes the quantities measured in the superfluid-component reference frame (i.e., frame where the superfluid velocity is zero). Therefore, E_0 and $\mathbf{j}_0$ are, respectively, the energy density and the momentum density relative to the superfluid component. The former is a function of ρ, $\mathbf{j}_0$, and entropy density S. The differential of E_0 can be written as

$$dE_0 = TdS + \mu d\rho + \mathbf{w}d\mathbf{j}_0, \qquad (2)$$

where the Lagrange multipliers T, μ, and $\mathbf{w}$ have the meaning of, respectively, temperature, chemical potential, and so-called relative velocity of the normal and superfluid components.

For the isotropic fluid, the following useful relations can be obtained for the partial derivatives of $\mathbf{j}_0$ with respect to $\mathbf{w}$:

$$\left(\frac{\partial j_0^k}{\partial w^l}\right)_{T,\rho} = \frac{w^k w^l}{w^2}\left(\frac{\partial j_0}{\partial w}\right)_{T,\rho} + \left(\frac{\delta^{kl}}{w} - \frac{w^k w^l}{w^3}\right) j_0. \qquad (3)$$

Indeed, the velocity $\mathbf{w}$ and momentum density $\mathbf{j}_0$ are parallel to each other:

$$\mathbf{j}_0 = j_0(T, \rho, w)\frac{\mathbf{w}}{w}.$$

By differentiating this identity, one obtains Eq. (3).

Next, transforming Eq. (1) and using Eq. (2), one can write dE as

$$dE = TdS + \left(\mu + \frac{v_s^2}{2} - \mathbf{v}_s\mathbf{v}_n\right)d\rho + (\mathbf{j} - \rho\mathbf{v}_n)d\mathrm{v}_s + \mathbf{v}_n d\mathbf{j}, \quad (4)$$

where $\mathbf{j} = \rho\mathbf{v}_s + \mathbf{j}_0$ is the total momentum density and $\mathbf{v}_n = \mathbf{v}_s + \mathbf{w}$ is the normal velocity.

The stability implies that any "allowed" fluctuation raises the total energy E_{tot} of the system. The allowed fluctuations are those which do not change conserved quantities. This signifies that the minimum of E_{tot} should be sought for at constant entropy and all additive integrals of motion: mass, momentum, and superfluid velocity. Whereas the mass and momentum conservation phenomena are well-known, the conservation of the superfluid velocity deserves special remarks. Indeed, superfluid motion has the potential character; i.e., the velocity $\mathbf{v}_s$ is the gradient of a certain scalar, $\mathbf{v}_s = \nabla\phi$. The same relation can be written for the time derivative, $\dot{\mathbf{v}}_s = \nabla\dot{\phi}$. The latter expression, clearly, is the conservation law for all three components of vector $\mathbf{V}_s = \int \mathbf{v}_s\, d\mathbf{r}$, which, hence, is the additional integral of motion specific to a superfluid.

Consider a macroscopic fluctuation δS, $\delta\rho$, $\delta\mathbf{v}_s$, and $\delta\mathbf{j}$ of all variables. Since these quantities are conserved, the first variation of the total energy of a homogeneous system is identical to zero:

$$\delta E_{\mathrm{tot}} = \int\left\{\left(\frac{\partial E}{\partial S}\right)_{\rho, \mathbf{v}_s, \mathbf{j}}\delta S + \left(\frac{\partial E}{\partial \rho}\right)_{S, \mathbf{v}_s, \mathbf{j}}\delta\rho + \left(\frac{\partial E}{\partial \mathbf{v}_s}\right)_{S, \rho, \mathbf{j}}\delta\mathbf{v}_s + \left(\frac{\partial E}{\partial \mathbf{j}}\right)_{S, \rho, \mathbf{v}_s}\delta\mathbf{j}\right\}d\mathbf{r} \equiv 0.$$

The 8×8 matrix of the quadratic form for the second variation of the total energy is the Jacobian

$$Q = \left\|\frac{\partial(T, \mathbf{v}_n, \mu + v_s^2/2 - \mathbf{v}_s\mathbf{v}_n, \mathbf{j} - \rho\mathbf{v}_n)}{\partial(S, \mathbf{j}, \rho, \mathbf{v}_s)}\right\|.$$

It is positively definite if all principal minors M_1, M_2, …, M_8 in the upper left corner are positive. Below, we consider, by turns, the requirements on these minors.

The first requirement for the positiveness

$$M_1 = \frac{\partial(T, \mathbf{j}, \rho, \mathbf{v}_s)}{\partial(S, \mathbf{j}, \rho, \mathbf{v}_s)} = \frac{\partial(T, \mathbf{j}, \rho, \mathbf{v}_s)}{\partial(T, \mathbf{v}_n, \rho, \mathbf{v}_s)}\frac{\partial(T, \mathbf{v}_n, \rho, \mathbf{v}_s)}{\partial(S, \mathbf{j}, \rho, \mathbf{v}_s)}$$

$$= \left(\frac{\partial j_0}{\partial w}\right)_{T, \rho}\left(\left(\frac{\partial S}{\partial T}\right)_{\rho, w}\left(\frac{\partial j_0}{\partial w}\right)_{T, \rho} - \left(\frac{\partial j_0}{\partial T}\right)^2_{\rho, w}\right)^{-1} > 0$$

is the generalization of the usual requirement for the positive heat capacity. Below, it will be shown (Eq. (8)) that $(\partial j_0/\partial w)_{T, \rho} > 0$, so that the last inequality, in fact, can be written as

$$\left(\frac{\partial S}{\partial T}\right)_{\rho, w}\left(\frac{\partial j_0}{\partial w}\right)_{T, \rho} - \left(\frac{\partial j_0}{\partial T}\right)^2_{\rho, w} > 0. \quad (5)$$

The positiveness of the following group of minors can easily be verified using the transformations

$$Q' = \left\|\frac{\partial(T, \mathbf{v}_n, \rho, \mathbf{v}_s)}{\partial(S, \mathbf{j}, \rho, \mathbf{v}_s)}\right\| = \left\|\frac{\partial(T, \mathbf{j}, \rho, \mathbf{v}_s)}{\partial(S, \mathbf{j}, \rho, \mathbf{v}_s)}\right\|\left\|\frac{\partial(T, \mathbf{v}_n, \rho, \mathbf{v}_s)}{\partial(T, \mathbf{j}, \rho, \mathbf{v}_s)}\right\|. \quad (6)$$

It follows that the minors M_2, M_3, and M_4 will be positive if all minors of the second term in Eq. (6) are positive:

$$\left\|\left(\frac{\partial \mathbf{j}}{\partial \mathbf{v}_n}\right)_{T, \rho, \mathbf{v}_s}\right\|^{-1} = \left\|\left(\frac{\partial \mathbf{j}_0}{\partial \mathbf{w}}\right)_{T, \rho}\right\|^{-1} = \left\|\begin{array}{ccc} (\partial j_0/\partial w)_{T, \rho} & 0 & 0 \\ 0 & j_0/w & 0 \\ 0 & 0 & j_0/w \end{array}\right\|^{-1}.$$

We used identity (3) and chose the direction of vector $\mathbf{w}$ as the first coordinate axis. Thus, our set is augmented by the following inequalities:

$$\mathbf{j}_0\mathbf{w} \geq 0, \quad (7)$$

$$\left(\frac{\partial j_0}{\partial w}\right)_{T, \rho} > 0. \quad (8)$$

The same transformation, when applied to the largest minor, yields

$$Q = Q'\left\|\frac{\partial(T, \mathbf{v}_n, \mu + v_s^2/2 - \mathbf{v}_s\mathbf{v}_n, \mathbf{j} - \rho\mathbf{v}_n)}{\partial(T, \mathbf{v}_n, \rho, \mathbf{v}_s)}\right\| = Q'Q''.$$

Similarly, the minors M_5, M_6, M_7, and M_8 are positive if the nonzero principal minors of the Q'' matrix are positive. Using the thermodynamic identity

$$d\mu = \frac{dp}{\rho} - \frac{S}{\rho}dT - \frac{\mathbf{j}_0}{\rho}d\mathbf{w},$$

one gets

$$\left(\frac{\partial(\mu + v_s^2/2 - \mathbf{v}_s\mathbf{v}_n)}{\partial\rho}\right)_{T,\mathbf{v}_n,\mathbf{v}_s} = \left(\frac{\partial\mu}{\partial\rho}\right)_{T,\mathbf{w}} = \frac{1}{\rho}\left(\frac{\partial p}{\partial\rho}\right)_{T,w}.$$

Below, the explicit expression is given for the submatrix corresponding to the ρ, v_s^x, v_s^y, v_s^z subspace of matrix Q''. The x axis is directed along the vector $\mathbf{w}$. Using Eq. (3), one obtains

$$\begin{Vmatrix} (\partial p/\partial\rho)_{T,w}/\rho & (\partial j_0/\partial\rho)_{T,w} - w & 0 & 0 \\ (\partial j_0/\partial\rho)_{T,w} - w & \rho - (\partial j_0/\partial w)_{T,\rho} & 0 & 0 \\ 0 & 0 & \rho - \dfrac{j_0}{w} & 0 \\ 0 & 0 & 0 & \rho - \dfrac{j_0}{w} \end{Vmatrix}.$$

The corresponding inequalities have the form

$$\left(\frac{\partial p}{\partial\rho}\right)_{T,w} > 0, \tag{9}$$

which is the generalized requirement (in the case of nonzero relative velocity w) for the positive compressibility,

$$j_0 < w\rho \tag{10}$$

and

$$\left(\frac{\partial p}{\partial\rho}\right)_{T,w}\left(\rho - \left(\frac{\partial j_0}{\partial w}\right)_{T,\rho}\right) - \rho\left(\left(\frac{\partial j_0}{\partial\rho}\right)_{T,w} - w\right)^2 > 0. \tag{11}$$

Inequalities (5), (7)–(11) comprise a full set of conditions for thermodynamic stability.

3. DISCUSSION

In the situation with a "stopped normal component," the mass flow $\mathbf{f}$ relative to the normal component may prove to be a more suitable variable than the flow $\mathbf{j}_0$ relative to the superfluid component. Using the obvious relation $f = \rho w - j_0$, one can reformulate the obtained inequalities as

$$\mathbf{f}\mathbf{w} < 0, \quad f < w\rho, \tag{12}$$

$$0 < \left(\frac{\partial f}{\partial w}\right)_{\rho,T} < \rho, \tag{13}$$

$$\left(\frac{\partial S}{\partial T}\right)_{\rho,w}\left(\rho - \left(\frac{\partial f}{\partial w}\right)_{T,\rho}\right) > \left(\frac{\partial f}{\partial T}\right)_{\rho,w}^2, \tag{14}$$

$$\left(\frac{\partial p}{\partial\rho}\right)_{T,w}\left(\frac{\partial f}{\partial w}\right)_{\rho,T} > \rho\left(\frac{\partial f}{\partial\rho}\right)_{w,T}^2. \tag{15}$$

As a simple example of using the derived inequalities, we consider the case $w = 0$. From Eqs. (12)–(15), one has

$$\left(\frac{\partial S}{\partial T}\right)_{\rho,w} > 0, \quad \left(\frac{\partial p}{\partial\rho}\right)_{T,w} > 0, \tag{16}$$

$$\rho > \left(\frac{\partial j_0}{\partial w}\right)_{T,\rho} > 0. \tag{17}$$

In usual notation, the last inequality has a clear physical meaning:

$$\rho_s > 0, \quad \rho_n > 0. \tag{18}$$

4. PHONON–ROTON MODEL

Let us apply the obtained stability criteria to a real ^{4}He superfluid. To evaluate the derivatives entering the inequalities, a microscopic model is necessary. The role of the latter can successfully be played by the Landau phonon–roton theory, which is valid over a wide range of temperatures and velocities. We will use it for calculating the quasiparticle contribution to the "modified" free energy in the coordinate system where the superfluid component is at rest:

$$\tilde{\mathcal{F}}_0 = \mathcal{F}_0 - \mathbf{w}\mathbf{j}_0, \quad d\tilde{\mathcal{F}}_0 = -SdT - \mathbf{j}_0 d\mathbf{w}.$$

This potential can be obtained from the spectrum of elementary excitations using the well-known expression

$$\tilde{\mathcal{F}}_0 = T\int \ln\left(1 - \exp\left(\frac{\mathbf{p}\mathbf{w} - \epsilon(p)}{T}\right)\right)\frac{d\mathbf{p}}{(2\pi\hbar)^3}.$$

Here, the excitation energy $\epsilon(p)$ for two branches is given by

$$\epsilon_{ph}(p) = cp, \quad \epsilon_r(p) = \Delta + (p - p_0)^2/2m.$$

The indices ph and r are used for the quantities relating to phonons and rotons, respectively; c is the sound velocity; Δ is the roton gap; and m and p_0 are the roton effective mass and momentum, respectively (the used numerical data can be found in [4, 5]: $\rho = 0.145$ g/cm^3, $\Delta = 8.7$ K, $m = 0.16m_{He}$, $p_0/\hbar\rho^{1/3} = 3.673\times10^8$ g$^{-1/3}$, $c = 238$ m/s, $\partial\Delta/\partial\rho = -0.47\times10^{-14}$ cm^5 s^{-2}, $\partial m/\partial\rho = -0.45\times10^{-23}$ cm^3, and $\partial c/\partial\rho = 467\times10^3$ cm^4 s^{-1} g^{-1}). For a small dimensionless parameter $m\Delta/p_0^2 \sim 0.03 \ll 1$, the Landau critical velocity is determined by the expression $v_L = \Delta/p_0$.

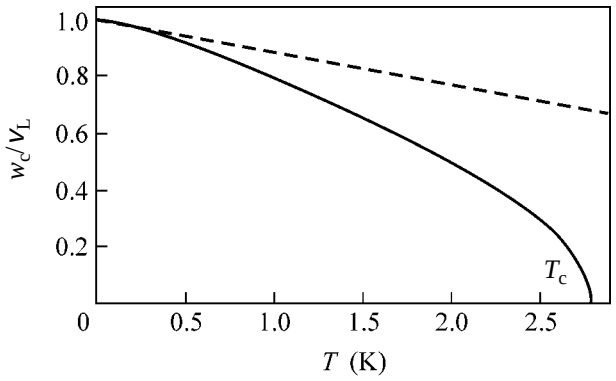

Critical velocity w_c as a function of temperature T at normal pressure. The dashed line corresponds to the equality $T = \Delta - p_0 w$; one can see that the condition $T < \Delta - p_0 w$ is fulfilled over the entire stability region. At zero temperature, the "instability" critical velocity w_c coincides with the Landau critical velocity v_L, and it turns to zero at the critical temperature T_c (λ point) (see Eq. (18)). In the phonon–roton model, the critical temperature is $T_c \approx 2.8$ K.

After integration, the above relationships bring about the following expression for the contribution to the free energy:

$$\tilde{\mathcal{F}}_0 = -\frac{T^4\pi^2}{90\hbar^3c^3}\left(1-\frac{w^2}{c^2}\right)^{-2}$$

$$-\frac{T^{5/2}m^{1/2}}{2^{1/2}\pi^{3/2}\hbar^3}\frac{p_0}{w}\sinh\frac{wp_0}{T}\exp\left(-\frac{\Delta}{T}\right).$$

By differentiating this potential, one can obtain all the desired thermodynamic quantities. Namely,

$$S = -(\partial\tilde{\mathcal{F}}_0/\partial T)_{w,\rho}, \quad j_0 = -(\partial\tilde{\mathcal{F}}_0/\partial w)_{T,\rho}.$$

The quasiparticle contribution to the pressure derivatives are ignored.

Inequality (11) breaks first. The point set satisfying this inequality in the T–w plane is shown in the figure. Fluid loses stability in the region above the solid line drawn in the figure.

At zero temperature, the critical velocity tends to the Landau critical velocity v_L. Note that, for the systems where all excitations allow fluid-dynamic description (in other words, in the systems without roton branch), inequality (11) at zero temperature implies that the condition $(\partial p/\partial\rho)_{T,w} - w^2 > 0$ is fulfilled; i.e., $w < c$.

5. CONCLUSIONS

It is assumed that the superfluidity breakdown in narrow orifices has the following nature [1]. As long as the cross section is not too small, the critical velocity is independent of temperature and increases as the orifice narrows. This is precisely the behavior that is typical of the Feynman critical velocity associated with the vortex formation.

In very narrow orifices, the vortex critical velocity becomes so high that the superfluidity breakdown mechanism and its properties change: the critical velocity no longer depends on the orifice cross section, but decreases with a rise in temperature. Such a behavior is ordinarily related [1] to the Iordanskii–Langer–Fisher mechanism [6]. However, because of the lack of reliable information about orifice profiles, this theory was not compared numerically with the experiment.

At the same time, the experimentally observed behavior of critical velocity can be associated with the stability criterion described above. In other words, we suggest an alternative explanation of the experimental results on the assumption that the thermodynamic limit w_c is achieved in narrow orifices.

When comparing our predictions with the experimental data, one should bear in mind the following. The assumption that the critical velocity is determined by the stability limit implies that the equations of fluid dynamics inside the channel are essentially nonlinear. In particular, this means that the superfluid component cannot be considered as an incompressible fluid fraction. In other words, the phase difference between the channel ends is not proportional to the maximal attained velocity.

It is worth noting that the approach used in this work for the critical velocity as a stability limit is similar to the approach used in the Kramer work [7]. Although the inequalities proposed in that work are not thermodynamic, the numerical values of critical velocity obtained by Kramer on the basis of the phonon–roton model are close to the values shown in the figure.

We are grateful to I.A. Fomin for helpful discussions. This work was supported by the INTAS (grant no. 01-686), CRDF (grant no. RP1-2411-MO-02), Russian Foundation for Basic Research (project no. 03-02-16401), and the Presidential Program for the Support of Leading Scientific Schools.

REFERENCES

1. E. Varoquaux, W. Zimmermann, and O. Avnel, in *Excitations in Two-Dimensional and Three-Dimensional Quantum Fluids*, Ed. by A. F. G. Wyatt and H. J. Lauter (Plenum, New York, 1991), NATO ASI Ser., p. 343.
2. I. M. Khalatnikov, *An Introduction to the Theory of Superfluidity* (Benjamin, New York, 1965).
3. L. D. Landau and E. M. Lifshitz, *Course of Theoretical Physics*, Vol. 5: *Statistical Physics*, 3rd ed. (Nauka, Moscow, 1976; Pergamon Press, Oxford, 1980).
4. R. J. Donnelly and P. H. Roberts, J. Low Temp. Phys. **27**, 687 (1977).
5. R. J. Donnelly, J. A. Donnelly, and R. N. Hills, J. Low Temp. Phys. **44**, 471 (1981).
6. J. S. Langer and J. D. Reppy, in *Progress in Low Temperature Physics*, Ed. by C. J. Gorter (North-Holland, Amsterdam, 1970), Vol. 6, Chap. 1.
7. L. Kramer, Phys. Rev. **179**, 149 (1969).

Translated by V. Sakun

JETP Letters, Vol. 78, No. 9, 2003, pp. 578–582. From Pis'ma v Zhurnal Éksperimental'noĭ i Teoreticheskoĭ Fiziki, Vol. 78, No. 9, 2003, pp. 1068–1072.

Tunneling Conductivity Features of the New Reconstructed Phases on the GaN(0001) Surface¶

N. S. Maslova[1], V. I. Panov[1], K. Wu[2], Q. Z. Xue[2], T. Nagao[2], and A. I. Oreshkin[1, 2, *]

[1] *Physical Department, Moscow State University, Moscow, 119992 Russia*

[2] *Institute for Materials Research, Tohoku University, Sendai 980-8577, Japan*

**e-mail: oreshkin@spmlab.phys.msu.su*

Received October 6, 2003

Two new Au-induced reconstructed phases on the GaN(0001) surface have been identified and investigated by STM/STS method. Ringlike and $c(2\times12)$ surface nanostructures were observed on STM images. The commensurate $c(2\times12)$ structure (α-phase), according to our spectroscopic measurements, demonstrates properties of a 1D system, whereas the incommensurate β-phase looks similar to a disordered 2D system. © *2003 MAIK "Nauka/Interperiodica".*

PACS numbers: 68.35.Bs; 68.35.Rh; 68.37.Ec

GaN and its related alloys have become a very attractive subject in the past several years for several reasons. On the one hand, GaN is of interest for practical application in a short-wave optical range for the creation of optoelectronic devices and, on the other hand, the unique incommensurate fluidlike structure of the surface stimulates interest such as the transition from incommensurate to commensurate phases by the adsorption of metals, and the influence of the fluid structure on the growth of metals on the GaN surface. During the last several years, we have been able to observe great developments in both high quality material growth [1] and device fabrications [2–4]. At the same time, some fundamental questions, i.e., on adsorption mechanism, growth mode, possible metal-induced reconstructions, and their properties are still not clear. Wurtzite GaN is a polar semiconductor with two basal planes, i.e., the Ga-polar (0001) and N-polar $(000\bar{1})$. While the intrinsic bulk-terminated GaN(0001) surface is disordered, a series of surface reconstructions can be prepared by moving additional Ga from the N-rich 2×2 [5, 6] to the Ga-rich 4×4, 2×2, 5×5 [7, 8], 4×6 [5], and the most Ga-rich pseudo-1×1 surfaces [5–9]. Typical MOCVD and MBE growth of GaN are performed under Ga-rich conditions, and it has been shown that the pseudo-1×1 surface plays the role of surfactant layer, promoting the two-dimensional step-flow growth [9, 10]. Thus, from a practical point of view, the pseudo-1×1 surface is the first candidate for studying metal adsorption and growth. Smith *et al.* [5, 6] have determined that the surface has about 2–3 ML (1 ML refers to the atomic density in the GaN(0001) plane, i.e., 1.1×10^{15} cm^{-2}) additional Ga, and it is characterized by a δ-1×1 reflection high-energy electron diffraction (RHEED) pattern. The STM image is usually smooth and featureless, and 1×1 corrugation can be observed only under specific tunneling conditions. A "Ga fluid" model has been proposed by Smith *et al.* [5, 6] and Northrup *et al.* [11]. According to this model, two additional Ga adlayers above GaN surface are present. The first layer of Ga is fixed in 1×1 configuration, and the second layer (top layer) has a contracted structure with the Ga density of 1.3 ML (similar to some metal surfaces at high temperature, e.g., Ir [12], Pt [13], and Au [14]). It is very interesting to note that the top layer of Ga is intrinsically mobile at room temperature, resulting in the 1×1 corrugation observed by the STM. Mula *et al.* [9] have reported that the pseudo-1×1 surface is very stable, and further deposition of several hundred ML Ga does not change the structure, indicating a zero sticking coefficient of Ga on this Ga-saturated surface.

We chose the GaN(0001)-pseudo-1×1-Ga (hereafter "Ga-fluid") surface as the substrate and then studied the adsorption of the Au submonolayer at RT. We found two new reconstructions induced by Au at RT, i.e., the commensurate $c(2\times12)$ reconstruction (α-phase) and incommensurate β-phase. Results of spectra measurements clearly demonstrate a possibility of formation of 1D and 2D systems on the basis of a mixed Au–Ga adatom structure. All the experiments were performed in ultrahigh vacuum conditions. The quality of tunneling tips was controlled by a field ion microscope (FIM) attached to the STM chamber [15]. We used commercial PtIr tips as successfully as tips prepared from the ⟨111⟩-oriented W-crystal wire by electrochemical etching. Before scanning, the tips were degas at 500°C during 8 h, then field evaporation was used to remove the oxide layers and to shape the scanning tips. The substrate was a commercial 1.5-mm-thick GaN(0001) film

¶This article was submitted by the authors in English.

grown on a SiC(0001) wafer by MOCVD. RHEED was employed to monitor the surface structure during growth. Au was evaporated from a tungsten coil heater, and the Au flux was controlled by the heater current. The typical flux used in the present study was 0.2 ML/min.

Both filled and empty state images were acquired at a constant current mode with a tunnel bias voltage applied to the sample and a tunneling current of 20 pA. The GaN(0001)-pseudo-1×1 was formed by terminating MBE growth on the GaN(0001) surface under Ga-rich conditions. Figure 1 shows an STM image of Ga-rich surface (pseudo-1×1), prepared by deposition of about 2 ML of Ga above the last GaN bilayer. This STM image shows large and smooth terraces with the typical terrace width of several hundred Å, with no specific features in either filled or empty state STM images. The 1×1 atomic corrugation can be observed only with a very sharp tip at very low bias voltage, as shown in the inset in Fig. 1a. The RHEED pattern of this surface shows a "1×1" pattern consistent with STM observation. The presence of the satellite peaks indicates the contraction of the Ga adatom layer, and the 1×1 structure observed by STM is due to the mobility of the top Ga adlayer. These observations are consistent with the report by Smith and Northrup [6, 11]. After deposition of the Au submonolayer on the pseudo-1×1 surface at room temperature, we were able to observe two new phases on the surface. There are two reconstructions: commensurate $c(2 \times 12)$ (α-phase) and incommensurate β-phase. The area of the two new phases increases with increasing Au coverage until they fully cover the whole surface. Figure 1b shows the simultaneous formation of α- and β-phases at Au coverage of about 0.02 ML. As can be seen from this image, two patches of α- and β-phases are formed on the same terrace (double-step height) initially covered by "Ga fluid." The size of the terrace is about 1000 Å. The corrugation height of α-phase is apparently bigger than that for the β-phase (the height profile measurement gives a height difference of 2.0 and 0.5 Å, respectively, with respect to the Ga fluid surface). The $c(2 \times 12)$ reconstruction (α-phase) (Fig. 2a) contains parallel atomic rows running along the $[11\bar{2}0]$ direction, in which each pair of bright rows is separated by a dark row. The unit cell is rectangular, and the periodicity in the $[11\bar{2}0]$ and $[1\bar{1}00]$ directions is $2a$ and $6(\sqrt{3}/2)a$, respectively, which is denoted as $c(2 \times 12)$ reconstruction. The periodicity can be further confirmed by the RHEED measurement as shown in Fig. 2b. The "6×" in the $[11\bar{2}0]$ azimuth and a "4×" in the $[1\bar{1}00]$ azimuth are clearly identified, corresponding to a $c(2 \times 12)$ periodicity in the real space. Another common Au-induced phase is the incommensurate β-phase. Figure 3 shows two STM images of the same place of the β-phase at different bias voltage polarities.

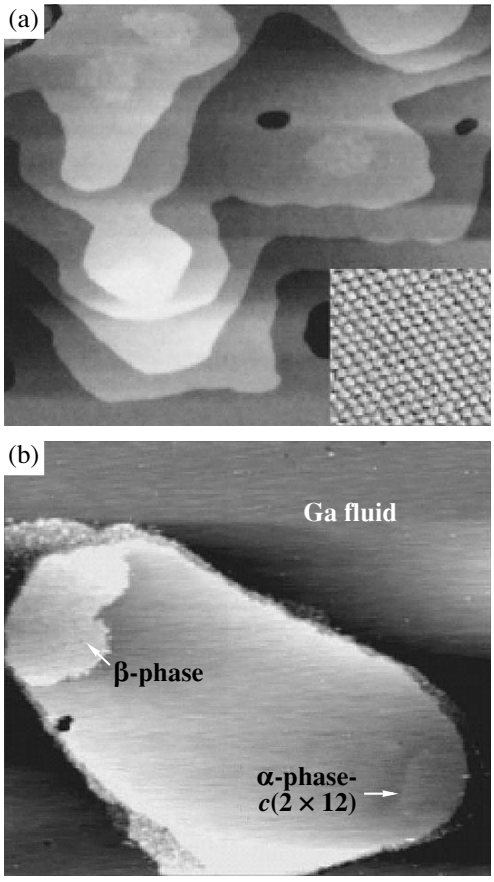

Fig. 1. Filled-state STM images of (a) as-prepared "Ga fluid" (2500 × 2200 Å). At normal tunneling conditions, the surface is smooth and without corrugation. The inset image shows a 40 × 40 Å area with 1×1 corrugation obtained at a sample bias of –0.1 V. (b) After adsorption of Au at coverage of ~0.02 ML, two patches of $c(2 \times 12)$ (α-phase) and β-phase form on the same isolated double step-height terrace (about 1200 Å in size).

The corrugation height is smaller for a filled-states STM image (Fig. 3a) compare to an empty-states one (Fig. 3b). This will be discussed in more detail later. The structure consists of hexagonally packed protrusions with a distance of the nearest neighbor of ~8.6 Å. The closed-packing direction is along the $[1\bar{1}00]$ direction, 30° rotated from the closed-packing direction of substrate, $[11\bar{2}0]$. Ringlike modulation patterns can be observed randomly distributed on the surface. We suggest that the incommensurate β-phase is comprised of two-dimensionally grown Au islands, with the underlying Ga bilayer structure still remaining. First, the height difference between the β-phase and the "Ga fluid" substrate is about 2 Å, consistent to the interlayer distance of the Au(111) plane (this is much higher than the $c(2 \times 12)$-Au phase where the height difference is only about 0.5 Å). Second, the nearest maxima spacing is 8.6 Å, being incommensurate with the substrate lat-

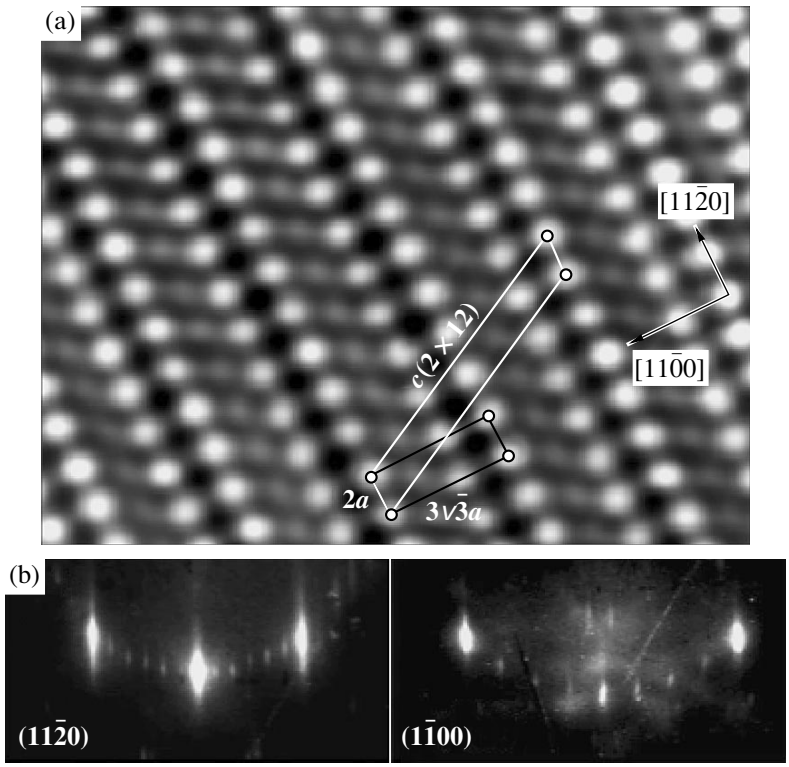

Fig. 2. (a) Zoom in image of the $c(2 \times 12)$ reconstruction. The tunneling current is 20 pA at sample bias voltage of 0.4 V, the image scale is 90×70 Å. (b) RHEED pattern of the $c(2 \times 12)$ surface, where 6× in the [11$\bar{2}$0] and 4× in the [1$\bar{1}$00] directions are identified. This corresponds to a $c(2 \times 12)$ periodicity in the real space.

tice constant of 3.19 Å. But it is approximately three times the lattice constant on the Au(111) plane, 2.88 Å. So, this structure can be explained by pure Au(111) islands formed on top of the Ga fluid surface. The 3× corrugation is possible in strain-induced modulation patterns due to a 4% lattice mismatch between Au (2.88 Å) and the Ga-fluid (2.76 Å), that is much smaller than the mismatch between Au and the bulk GaN substrate (10%). This is the reason why we can prepare flat Au film on the Ga-fluid surface, while the growth of Au on bulk-terminated GaN surface results in 3D agglomerations (the result will be published elsewhere). It should be noted that, upon formation of the β-phase, the originally mobile Ga atoms on the underneath of the "Ga fluid" substrate have to cease moving. This may result in the segregation of some of the Ga atoms into the Au surface, which is a likely origin of the ringlike patterns observed in the STM images. The discovered ringlike structure can be of interest for nanotechnology because of good reproduction and a small scattering parameter.

The *I–V* characteristics measured above the surface area of β- and α-phases are present in Fig. 4. Prior to taking these measurements, the tip was fixed at a certain surface site (ringlike or $c(2 \times 12)$ structure) with fixed tunneling parameters: $V_s = -2.0$ V, $I_t = 50$ pA. The best STM images of the ringlike structure were obtained in the range of $V_s = \pm 0.5$ V. This is in the good agreement with our STS spectra. As one would expect from Fig. 4a, the contrast of the STM image at $V_s = +0.5$ V should be higher than this one at $V_s = -0.5$ V. This difference is clearly seen from Fig. 3. It is obvious that the spectra have a metallic-like character. Tunneling conductivity measured above the $c(2 \times 12)$ structure reveal a peak at zero bias voltage. Moreover, two dips at 0.25 and –0.15 V are clearly seen on normalized tunneling conductivity $(dI/dV)/(I/V)$ curves. Two peaks also appear on tunneling conductivity curves at 0.5 and –0.5 V. We connect this behavior of tunneling conductivity with a quasi-one-dimensional character of the electronic density of states along the double-chain structure ($c(2 \times 12)$). The electron states of the double-chain structure ($c(2 \times 12)$) can be described by the simple model Hamiltonian:

$$\hat{H} = \sum_{k,\sigma} \varepsilon_{1k} a^{+}_{1k\sigma} a_{1k\sigma} + \varepsilon_{2k} a^{+}_{2k\sigma} a_{2k\sigma} + T a^{+}_{1k\sigma} a_{2k\sigma} + \text{h.c.}, \quad (1)$$

where $\varepsilon_{1k} = \varepsilon_{2k} = t\cos(ka)$ is the 1D energy spectrum of electrons along each noninteracting chain; t is the hopping matrix element between the nearest neighboring

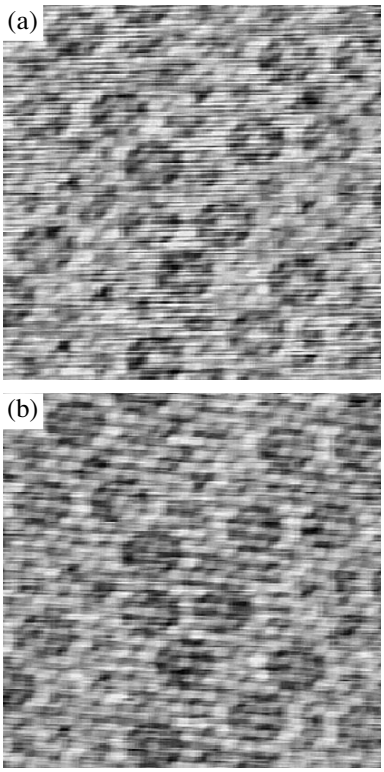

Fig. 3. STM image of the same site of β-phase structure (175 × 175 Å). The tunneling current is 50 pA. (a) Filled-state STM image of ringlike structure (V = –0.5 V). (b) Empty-state STM image of ringlike structure (V = 0.5 V).

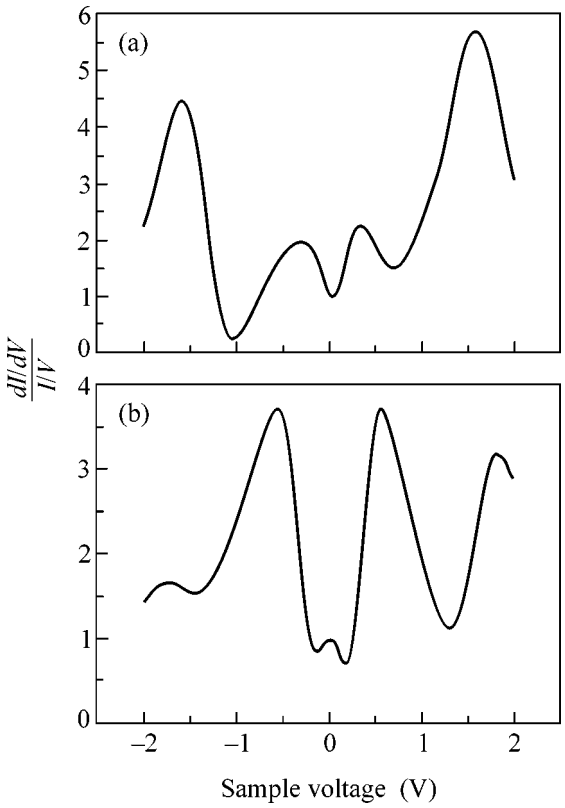

Fig. 4. Normalized tunneling conductivity measured above: (a) ringlike structure, (b) $c(2 \times 12)$ structure.

sites along each chain of $c(2 \times 12)$ structure; and $a^{+}_{ik\sigma}$ ($a_{ik\sigma}$) is the creation (annihilation) operator of electrons in the state of momentum k and spin σ in the ith chain (i = 1, 2). The last term in the Hamiltonian corresponds to the interaction between nearest neighbors in different chains with hopping matrix element T. In k-space, the exact retarded electron Green function along each chain can be easily obtained. For example,

$$G^{1}_{kk} = \frac{\omega - \varepsilon_{2k}}{(\omega - \varepsilon_{1k})(\omega - \varepsilon_{2k}) - T^2}. \quad (2)$$

The poles of Green functions determine the electronic spectrum of double-chain structure:

$$\omega_{\pm} = t\cos(ka) \pm T. \quad (3)$$

The density of states along each of the interacting chains can be obtained as

$$-\frac{1}{\pi}\mathrm{Sp}_k\mathrm{Im}(G^{1(2)}_{kk}(\omega)) = \nu_{1(2)}(\omega). \quad (4)$$

So, we have two splitted quasi-1D bands, which are centered at $\pm T$ and have the width $2t$. In the symmetric case, one can obtain splitted bands and a 1D character of density of states:

$$\nu_{1(2)}(\omega) = \frac{1}{2ta}\left(1 - \left(\frac{\omega - T}{t}\right)^2\right)^{-1/2} + \frac{1}{2ta}\left(1 - \left(\frac{\omega + T}{t}\right)^2\right)^{-1/2}. \quad (5)$$

It is reasonable to assume that T and t are comparable because the distance between the chains is just the same as the interatomic distance along the chain. So, one can expect the appearance of two dips in the tunneling conductivity spectra when the value of applied bias approaches the energy center of each splitted 1D band: $eV = \pm T$. When applied voltage eV is close to the energy values of band edges: $eV = -T \pm t$ or $eV = T \pm t$, one should obtain strongly increased tunneling conductivity, because the 1D density of states has power law singularity at band edges with power law exponent –1/2. Similar dependence of local tunneling conductivity versus applied bias voltage observed near double-chain structure during STS measurements is shown in Fig. 4b. Singularities in tunneling conductivity are smoothed by interaction with a substrate, but peaks in $(dI/dV)/(I/V)$ curves corresponding to the edges of each 1D splitted band are clearly seen at zero applied bias and at V =

0.5 V and $V = -0.5$ V. Two dips are also present at $(dI/dV)/(I/V)$ curves at applied bias $V = 0.25$ V and $V = -0.15$ V. In contrast to the $c(2 \times 12)$ structure, the tunneling conductivity above ringlike surface structure has no features of the quasi-1D density of states. The tunneling conductivity peak at zero applied bias voltage is absent: a dip is clearly seen at $eV = 0$ on $(dI/dV)/(I/V)$ curves. Two peaks for ringlike structure instead of dips for $c(2 \times 12)$ structure have been found when the applied bias voltage is 0.2 or –0.2 V. Such behavior of local tunneling conductivity, especially the dip at small bias voltage, should be connected with disordered two-dimensional surface structure in β-phase.

In conclusion, two new reconstructions on the GaN(0001)-pseudo-1 × 1-Ga surface induced by Au at RT (i.e., the commensurate $c(2 \times 12)$ reconstruction (α-phase) and incommensurate β-phase) have been found. Scanning tunneling spectroscopy measurements revealed the existence of ordered one-dimensional structure with specific features in tunneling conductivity spectra, as well as disordered two-dimensional ringlike structure on the basis of GaN(0001)-pseudo-1 × 1-Ga surface.

This work was partially supported by SAS no. 30/03-MC, project no. 1604.2003.2, the Russian Foundation for Basic Research (project no. 03-02-16807), and "Nanostructures"-7. We gratefully acknowledge T. Sakurai for valuable discussions.

REFERENCES

1. S. Nakamura, T. Mukain, and M. Senoh, Appl. Phys. Lett. **64**, 1687 (1994).
2. F. A. Ponce and D. A. Bour, Nature **386**, 351 (1997).
3. S. Nakamura and G. Fasol, *The Blue Laser Diodes (GaN Based Light Emitters and Lasers)* (Springer, Heidelberg, 1997), p. 175.
4. J. I. Pankove, M. Leksono, S. S. Chang, *et al.*, MRS Internet J. Nitride Semicond. Res. **1**, 39 (1997).
5. A. R. Smith, R. M. Feenstra, D. W. Greve, *et al.*, Surf. Sci. **423**, 70 (1999).
6. A. R. Smith, R. M. Feenstra, D. W. Greve, *et al.*, J. Vac. Sci. Technol. B **16**, 2242 (1998).
7. Q. K. Xue, Q. Z. Xue, R. Z. Bakhtizin, *et al.*, Phys. Rev. Lett. **82**, 3074 (1999).
8. Q. Z. Xue, Q. K. Xue, R. Z. Bakhtizin, *et al.*, Phys. Rev. B **59**, 12604 (1999).
9. G. Mula, C. Adelmann, S. Moehl, *et al.*, Phys. Rev. B **64**, 195406 (2001).
10. L. X. Zheng, M. H. Xie, S. M. Seutter, *et al.*, Phys. Rev. Lett. **85**, 2352 (2000).
11. J. E. Northrup, J. Neugebauer, R. M. Feenstra, and A. R. Smith, Phys. Rev. B **61**, 9932 (2000).
12. M. A. van Hove, R. J. Koestner, P. C. Stair, *et al.*, Surf. Sci. **103**, 189 (1981).
13. U. Harten, A. M. Lahee, J. P. Toennies, and Ch. Woll, Phys. Rev. Lett. **54**, 2619 (1985).
14. A. R. Sandy, S. G. J. Mochrie, D. M. Zehner, *et al.*, Phys. Rev. Lett. **68**, 2192 (1992).
15. T. Sakurai, T. Hashizume, I. Kamiya, *et al.*, Prog. Surf. Sci. **33**, 3 (1990).

JETP Letters, Vol. 78, No. 9, 2003, pp. 583–586. From Pis'ma v Zhurnal Éksperimental'noĭ i Teoreticheskoĭ Fiziki, Vol. 78, No. 9, 2003, pp. 1073–1076.

π-Junction Realization Due to Tunneling through a Thin Ferromagnetic Layer¶

A. Buzdin

Condensed Matter Theory Group, CPMOH, UMR 5798, Université, 33405 Talence, France

Received September 12, 2003; in final form, October 7, 2003

It is demonstrated that in superconductor–ferromagnet–superconductor (S/F/S) systems in the case of low interface transparency the transition into π-phase is not related with the oscillations of the superconducting order parameter in F-layer. Consequently, the π-phase may exist at very thin F-layer thickness. The crossover from π- to 0-phase results in the nonmonotonous temperature dependence of the critical current. © *2003 MAIK "Nauka/Interperiodica".*

PACS numbers: 74.78.Fk; 74.50.+r

1. INTRODUCTION

The strong exchange field acting on the electrons in a ferromagnet provokes damping oscillatory behavior of the superconducting order parameter. This effect is at the origin of the π-junction realization in superconductor–ferromagnet–superconductor (S/F/S) systems [1, 2]. Recently, such π-junctions have been successfully fabricated and experimentally studied [3–5]. It has been demonstrated [6] that in a system composed of alternating superconducting and ferromagnetic atomic thickness layers the so-called π-phase may exist, wherein the superconducting order parameter changes its sign as we go from one superconducting layer to another. The π-phase shift in this case appears due to tunneling through the atomic ferromagnetic layer. Tunneling through a barrier with paramagnetic impurities also may provoke the π-phase shift in Josephson junctions [7, 8]. The possibility of the π-state realization in complex SFIFS Josephson junctions has recently been predicted [9, 10].

The particularity of the three latter cases is the special scenario of the 0–π transition, where the oscillations of the superconducting order parameter in the F-layer are absent.

Here we demonstrate that, astonishingly, this scenario also works in a simple S/F/S Josephson junction with the thin F-layer, when the transition into π-phase becomes possible in the case of very small transparency of the S/F boundary. Such situation becomes physically similar to tunneling through the atomic thickness of the F-layer [6], and the studies of corresponding Josephson junctions could provide an experimental test of this mechanism of the π-phase shift.

¶ This article was submitted by the author in English.

2. GENERAL FORMALISM

Let us consider the case of an S/F/S junction with a thin F-layer of thickness d and large superconducting electrodes. We suppose the dirty limit conditions hold with the thickness of F-layer being smaller than the characteristic length $\xi_f = \sqrt{D_f/h}$ of superconducting correlations decay (with oscillations) in the F-layer, where h is the ferromagnetic exchange field acting on the electron spins in the F-layer and D_f is the electron diffusion constant in the F-layer. As will be demonstrated, the crossover from 0- to π-phase occurs for small S/F interface transparency, i.e. when the induced superconductivity in F-layer is weak and may be described by the linearized Usadel equation for the anomalous function F_f (see for example [2]):

$$[|\omega| + i\,\mathrm{sgn}(\omega)h]F_f - \frac{D_f}{2}\frac{\partial^2 F_f}{\partial x^2} = 0, \qquad (1)$$

where $\omega = 2\pi T(n + 1/2)$ are the Matsubara frequencies and F-layer corresponds to the region $-d/2 < x < d/2$. Moreover, the weak S/F interface transparency permits one to neglect the proximity effect in S electrodes and consider the superconductivity there to be practically unperturbed by the F-layer. The interface transparencies enter through the general boundaries conditions at the S/F interfaces to Usadel equation [11]. Near T_c they can be written in the following form:

$$F_s(d/2) = F_f(d/2) + \xi_n\gamma_{B2}\left(\frac{\partial F_f}{\partial x}\right)_{d/2},$$

$$F_s(-d/2) = F_f(-d/2) - \xi_n\gamma_{B1}\left(\frac{\partial F_f}{\partial x}\right)_{-d/2}, \qquad (2)$$

$$\left(\frac{\partial F_s}{\partial x}\right)_{\pm d/2} = \frac{\sigma_n}{\sigma_s}\left(\frac{\partial F_f}{\partial x}\right)_{\pm d/2},$$

0021-3640/03/7809-0583$24.00 © 2003 MAIK "Nauka/Interperiodica"

where the notation $F_s(F_f)$ is used for the anomalous Green function in a superconductor (ferromagnet) and $\sigma_n(\sigma_s)$ is the conductivity of the F-layer (S-layer above T_c), and $\xi_s = \sqrt{D_s/2\pi T_c}$ is the superconducting coherence length of the S-layer, while $\xi_n = \sqrt{D_f/2\pi T_c}$. The parameter γ_B is related to the S/F boundary resistance per unit area R_b via the simple relation $\gamma_B = R_b\sigma_f/\xi_n$ [11] (note also the relation between γ_B and the transparency of the S/F interface $T = 1/(1 + \gamma_B)$ [11]). Further on, for simplicity we suppose that both interfaces are identical (so $\gamma_{B1} = \gamma_{B2} = \gamma_B$), and we will use the notation $F = F_f$. Also for small interface transparency (if $\sigma_n\xi_s/\sigma_s\xi_n \ll \gamma_B$) we may use the rigid boundary conditions (see for example [12, 13]) $F_s(-d/2) = \Delta e^{-i\varphi/2}/\sqrt{\omega^2 + \Delta^2}$ and $F_s(d/2) = \Delta e^{i\varphi/2}/\sqrt{\omega^2 + \Delta^2}$. This means that to find the anomalous Green function F_f it is in fact enough to use only the two first conditions in (2).

The solution of (1), satisfying the boundary conditions is readily written as:

$$F(x) = \frac{\Delta\cos(\varphi/2)}{\sqrt{\omega^2 + \Delta^2}(\cosh(kd/2) + k\gamma_B\xi_n\sinh(kd/2))}\cosh(kx) + \frac{\Delta i\sin(\varphi/2)}{\sqrt{\omega^2 + \Delta^2}(\sinh(kd/2) + k\gamma_B\xi_n\cosh(kd/2))}\sinh(kx), \quad (3)$$

where the complex wave vector

$$k = \sqrt{2(|\omega| + i\,\mathrm{sgn}(\omega)h)/D_f}.$$

Note that in principle, at arbitrary temperature the boundary conditions are different from those in (2) (see for example [12]). However, in the limit of low S/F interface transparency ($\gamma_B \gg 1$), when the amplitude of the F function in F-layer is small, we may use the linearized Usadel equation (1) at all temperatures. The only modification in the boundary conditions (2) is that F_s must be substituted by $F_s/|G_s|$ and γ_B by $\gamma_B/|G_s|$, where the normal Green function in a superconducting electrode $G_s = \omega/\sqrt{\omega^2 + \Delta^2}$. Taking this renormalization into account in the explicit form (3), we may put it in the formula for the supercurrent

$$J_s(\varphi) = ieN(0)D_f\pi T\sum_{-\infty}^{\infty}\left(F\frac{d}{dx}\tilde{F} - \tilde{F}\frac{d}{dx}F\right),$$

where $\tilde{F}(x, h) = F^*(x, -h)$, and obtain the usual sinusoidal current-phase dependence with the critical current

$$I_c = eN(0)D_f\pi T\sum_{-\infty}^{\infty}\frac{\Delta^2}{\omega^2 + \Delta^2}\frac{1}{G_s^2} \times \frac{2k}{\sinh(kd)(1 + (\gamma_B\xi_n/G_s)^2k^2) + 2k(\gamma_B/|G_s|)\xi_n\cosh(kd)}.$$

In the limit $kd \ll 1$ (i.e., $d < \xi_f$) the oscillations of anomalous function F are absent, but, nevertheless, if the boundary transparency is very low such that $1/\gamma_B \ll \xi_n d/\xi_f^2$, the critical current can change its sign. Indeed, in this limit the expression for the critical current reads

$$I_c = eN(0)D_f\pi T\sum_{-\infty}^{\infty}\frac{2\Delta^2}{\omega^2 + \Delta^2}\frac{1}{\gamma_B^2\xi_n^2 d} \times\left(\frac{1}{k^2} - \frac{d^2}{6} - \frac{2}{\gamma_B\xi_n dk^4}\frac{|\omega|}{\sqrt{\omega^2 + \Delta^2}}\right)$$

$$= 2eN(0)D_f\pi T\sum_{\omega>0}\frac{\Delta^2}{\omega^2 + \Delta^2}\frac{1}{\gamma_B^2\xi_n^2 d} \times\left(\xi_f^2\frac{(\omega/h)}{(\omega/h)^2 + 1} - \frac{d^2}{3} + \frac{\xi_f^4}{\gamma_B\xi_n d}\frac{1 - (\omega/h)^2}{(1 + (\omega/h)^2)^2}\frac{\omega}{\sqrt{\omega^2 + \Delta^2}}\right). \quad (4)$$

Usually, at experiment the Curie temperature Θ of ferromagnet is higher than the superconducting critical temperature T_c. For RKKY mechanism of ferromagnetic transition $\Theta \sim h^2/E_F$, so the exchange field h is much larger than the superconducting critical temperature T_c. Taking into account the condition $h \gg T_c$ and performing a summation over the Matsubara frequencies of the first two terms in the brackets (4), we finally obtain

$$I_c = \frac{eN(0)D_f\Delta\xi_f^2}{2\gamma_B^2 d\xi_n^2} \times\left\{\frac{\Delta}{h}\left[\Psi\left(\frac{1}{2} + i\frac{h}{2\pi T}\right) - \Psi\left(\frac{1}{2} + i\frac{\Delta}{2\pi T}\right) + \text{c.c}\right] - \frac{\pi}{3}\left(\frac{d^2}{\xi_f^2}\right)\tanh\left(\frac{\Delta}{2T}\right) + \frac{4\pi T\Delta\xi_f^2}{\gamma_B\xi_n d}\sum_{\omega>0}\frac{\omega}{(\omega^2 + \Delta^2)^{3/2}}\right\}. \quad (5)$$

Let us start the analysis of I_c over d dependence in the limit of very large γ_B (more precisely, when $\gamma_B \gg$

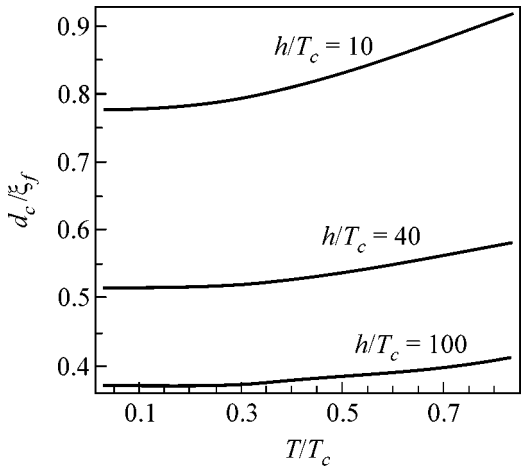

Fig. 1. Temperature dependences of the critical thickness d_c of the F-layer, corresponding to the crossover from 0- to π-phase in the limit of very small boundary transparency for different values of the exchange field.

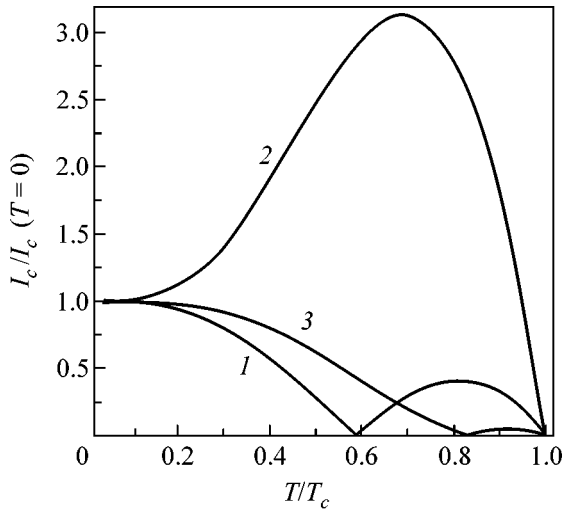

Fig. 2. Nonmonotonous temperature dependencies of the normalized critical current for low boundary transparency limit: curve *1*: $h/T_c = 10$ and $d/\xi_f = 0.84$; curve *2*: $h/T_c = 40$ and $d/\xi_f = 0.5$; curve *3*: $h/T_c = 100$ and $d/\xi = 0.41$.

(h/T_c)). In such a case, we may neglect the term proportional to $1/\gamma_B$ in the bracket of (5), and then obtain that at $T \longrightarrow 0$ the transition into the π-phase occurs (I_c changes its sign) at

$$d_c \approx \xi_f \sqrt{\frac{2\Delta(0)}{h} \ln\left(\frac{h}{\Delta(0)}\right)},$$

and indeed the condition $d < \xi_f$ is satisfied. Note that in the case of very low boundary transparencies the relevant formula obtained in [14] near the critical temperature in the limit $T_c/h \longrightarrow 0$ also reveals the crossover between 0- and π-phase. On the other hand, no transition into π-phase has been obtained in the analysis of S/F/S system [13], which is apparently related with the gradient expansion of the F-function in the ferromagnet when only the first term has been retained.

It is interesting to note that the critical F-layer thickness d_c, when the transition from 0- to π-phase occurs, depends on the temperature. The corresponding temperature dependences are presented in Fig. 1 for different value of T_c/h ratios. We see that $d_c(T)$ decreases when the temperature decreases. So for some range of F-layer thickness the transition from 0- to π-phase is possible when the temperature lowers. This resembles the situation with atomic thickness S/F multilayers [15] and we may therefore expect the nonmonotonous $I_c(T)$ dependences to reveal the crossover between 0- and π-phases for $d_c\,(T = 0) < d < d_c(T_c)$.

For the case of moderately large γ_B, i.e. when $1 \ll \gamma_B \ll h/T_c$, the terms with Ψ functions in (5) can be neglected and at $T = T_c$ the critical thickness d_c is

$$d_c(T = T_c) = \xi_f(3\xi_f/\gamma_B\xi_n)^{1/3},$$

while at $T \longrightarrow 0$ the critical thickness is somewhat smaller $d_c\,(T = 0) = \xi_f(6\xi_f/\pi\gamma_B\xi_n)^{1/3}$. The examples of different nonmonotonous $I_c(T)$ dependences for low barrier transparency limit $\gamma_B \gg (h/T_c)$ are presented in Fig. 2. We may see that the transition into π-phase state occurs starts roughly with the thickness $\xi_f/2$, and that rather unusual $I_c(T)$ dependencies may be expected.

The interface S/F transparency plays an important role in π-phase realization, and finite transparencies soften the conditions of the transition into π-state. An important particularity of the discussed mechanism is the existence of the temperature crossover in the limit $h \gg T_c$, which is relevant to the experimental situation. In the paper [3], the observed temperature crosssover has been explained by a model with a small exchange field $h \sim T_c \sim 8$ K. It is difficult to believe that the exchange field in the Cu_xNi_{1-x} alloy used in [3] was so small, as its Curie temperature was $\Theta \sim 20$–30 K. Such values of Curie temperatures imply an exchange field higher 100 K.

Note that the discussed mechanism of the π-phase appearance in the limit of large γ_B is quite robust toward the F-layer thickness fluctuations, as the π-phase must exist in the quite large interval $d_c < d \lesssim \xi_f$.

The condition of applicability of the Usadel equation is $l \ll d$, but qualitatively our analysis should be valid up to $d \sim l$ and it may provide an alternative explanation of the results of experiments [3].

The considered situation is analogous, in some sense, to the mechanism of π-phase realization due to tunneling through the ferromagnetic layer in the atomic S/F multilayer structure. There are very few layered systems with alternating superconducting and ferromagnetic layers and, up until now, there has been no

experimental evidence of π-phase existence in such systems. On the other hand, the Josephson S/F/S junctions with low interface transparency could be promising candidates for the observation of the discussed effect.

In conclusion, we propose a new mechanism of π-phase state formation in S/F/S junctions with a large interface barrier.

The author is grateful to M. Kuprianov for useful comments and recommendations and to C. Meyers for a critical reading of the manuscript.

REFERENCES

1. A. I. Buzdin, L. N. Bulaevskiĭ, and S. V. Panyukov, Pis'ma Zh. Éksp. Teor. Fiz. **35**, 147 (1982) [JETP Lett. **35**, 178 (1982)].
2. A. I. Buzdin and M. Yu. Kuprianov, Pis'ma Zh. Éksp. Teor. Fiz. **53**, 308 (1991) [JETP Lett. **53**, 321 (1991)].
3. V. V. Ryazanov, V. A. Oboznov, A. Yu. Rusanov, *et al.*, Phys. Rev. Lett. **86**, 2427 (2001).
4. T. Kontos, M. Aprili, J. Lesueur, *et al.*, Phys. Rev. Lett. **89**, 137007 (2002).
5. Y. Blum, A. Tsukernik, M. Karpovski, and A. Palevski, Phys. Rev. Lett. **89**, 187004 (2002).
6. A. V. Andreev, A. I. Buzdin, and R. M. Osgood III, Phys. Rev. B **43**, 10124 (1991).
7. I. O. Kulik, Sov. Phys. JETP **22**, 841 (1962).
8. L. N. Bulaevskii, V. V. Kuzii, and A. A. Sobyanin, JETP Lett. **25**, 290 (1977).
9. V. N. Krivoruchko and E. A. Koshina, Phys. Rev. B **63**, 224515 (2001); Phys. Rev. B **64**, 172511 (2001).
10. A. A. Golubov, M. Yu. Kuprianov, and Ya. V. Fominov, JETP Lett. **75**, 190 (2002).
11. M. Y. Kuprianov and V. F. Lukichev, Zh. Éksp. Teor. Fiz. **94**, 139 (1988) [Sov. Phys. JETP **67**, 1163 (1988)].
12. A. A. Golubov, M. Yu. Kuprianov, and E. Il'ichev, Rev. Mod. Phys. (2003, in press).
13. A. A. Golubov, M. Yu. Kuprianov, and Ya. V. Fominov, JETP Lett. **75**, 588 (2002).
14. A. Buzdin and I. Baladié, Phys. Rev. B **67**, 184519 (2003).
15. M. Houzet, A. Buzdin, and M. L. Kulic, Phys. Rev. B **64**, 184501 (2001).

JETP Letters, Vol. 78, No. 9, 2003, pp. 587–591. Translated from Pis'ma v Zhurnal Éksperimental'noĭ i Teoreticheskoĭ Fiziki, Vol. 78, No. 9, 2003, pp. 1077–1081.

Hopping Photoconduction and Its Long-Time Kinetics in a Heterosystem with Ge Quantum Dots in Si

N. P. Stepina*, A. I. Yakimov, A. V. Nenashev, A. V. Dvurechenskiĭ, and A. I. Nikiforov

Institute of Semiconductor Physics, Siberian Division, Russian Academy of Sciences, pr. Akademika Lavrent'eva 13, Novosibirsk, 630090 Russia

**e-mail: stepina@isp.nsc.ru*

Received October 7, 2003

The effect of interband-transition-inducing illumination on the hole hopping conduction along a two-dimensional array of Ge quantum dots in Si was studied. It is found that the photoconductance has either positive or negative sign depending on the initial filling of quantum dots with holes. In the course of illumination and after switching off the light, long-time photoconduction kinetics was observed (10^2–10^4 s at $T = 4.2$ K). The results are discussed in terms of a model based on the spatial separation of nonequilibrium electrons and holes in a potential relief formed by positively charged dots. The effect of equalization of potential barrier heights as a result of photohole capture by the charged quantum dots during the process of illumination and relaxation is suggested as an additional factor for explaining the phenomenon of persistent conduction. © *2003 MAIK "Nauka/Interperiodica".*

PACS numbers: 73.63.Kv; 72.20.Ee; 73.50.Pz

INTRODUCTION

The specific feature of type-II quantum dots (QDs) in the Ge/Si system is that, because of a large gap (~0.7 eV) between the Ge and Si valence bands, Ge forms a potential well for holes and a potential barrier for electrons. If the QD density is sufficiently high (~2–4×10^{11} cm^{-2}), the hole conduction has hopping character at low (<20 K) temperatures [1], while, at ~10 K, the phonon-assisted hopping conduction changes to the phononless charge transfer dominated by the Coulomb interaction. The authors of [2] argued that the hopping conductivity always increases upon disturbing the equilibrium of a disordered system and that the character of relaxation to equilibrium is determined by a large-scale Coulomb interaction [3]. The QD ensemble is distinguished from other disordered structures in that the hopping conductivity displays oscillatory dependence on the degree of filling dots with charge carriers [1], as a result of which the behavior of the system under nonequilibrium conditions can change dramatically. In particular, one can expect that the signs of interband photoconductance are different for different filling factors of holes in Ge QDs. Moreover, the positively charged QDs create Coulomb potential that is attractive for electrons and repulsive for holes. It is known [4] that the collective macroscopic potential barriers produced by various inhomogeneities in the system cause, in the majority of cases, the nonexponential kinetics of photoelectric excitations and, hence, anomalously long photoresponse relaxation times upon switching on and off the light. In the presence of Coulomb potential, the capture rates of nonequilibrium electrons and holes in the Ge/Si heterostructures with QDs are different at temperatures at which the hopping transport dominates, and this gives grounds to expect that the dynamics of transport processes in such systems are anomalous.

In [5] it is reasoned that the long-time relaxation of hopping conduction is evidence that the system is nonergodic and, hence, the time-averaged physical quantities characterizing the system differ from their statistical means. Although the nonergodic character of hopping-conduction relaxation is actively studied in electron glasses [2, 3, 6, 7] and the experimental data are rather numerous, the microscopic mechanism still remains to be understood. We assume that the carrier mobility changes upon excitation and the return to the initial state proceeds very slowly. The decisive role of interaction in the slow conduction kinetics was confirmed for Anderson's insulators by the calculations in [8]. To explain the long-time relaxation (LTR) of photoconduction in the semiconductor structures of the AlGaAs and AlGaN types, one often invokes the model of so-called DX and AX centers [9, 10]. The position of energy levels in the energy gaps of these centers change upon illumination, and this is accompanied by a considerable lattice relaxation that prevents the reverse transition. The persistent photoconduction (PPC), which practically always accompanies LTR, is also observed in magnetic materials, where it is caused by an increase in the size of ferromagnetic inclusions in a diamagnetic matrix. A change in the size of inclusions increases the degree of their overlap and, correspondingly, the conductance of the system. Finally, attempts are made to explain many experimental data using the so-called barrier model [4], which assumes that the electric fields

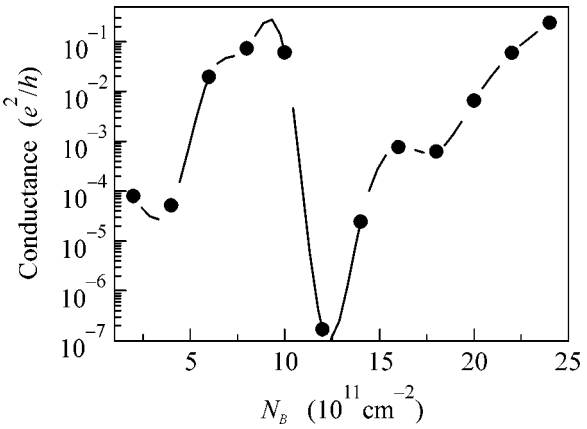

Fig. 1. Conductance at $T = 4$ K (in e^2/h units) as a function of the Si-δ-layer doping level.

of the barriers produced, as a rule, by inhomogeneities in the sample bring about spatial separation of nonequilibrium carriers, thereby hampering their recombination.

In spite of the ample experimental data, the physical nature of LTR remains to be clarified. Moreover, the inhomogeneities governing the long-time processes in the known semiconductor structures have a random character, so that the experimental characteristics change from sample to sample. In the heterostructures with the Ge QDs in Si, the potential barrier can be controlled by varying the QD charge state, allowing the development of a model system with reproducible dynamics.

In this work, to elucidate the LTR mechanism for photoconduction in a two-dimensional array of Ge/Si QDs, the photoconduction kinetics upon the illumination of the system by an interband light will be studied as a function of the degree of filling dots with holes, illumination intensity, and temperature.

EXPERIMENTAL

Structures were grown by molecular beam epitaxy on high-ohmic Si(001) substrates doped with boron to a concentration of ~10^{13} cm^{-3}. A germanium layer eight monolayers thick was introduced into the middle of a 400-nm epitaxial *p*-Si film (boron concentration was on the order of ~10^{16} cm^{-3}). The controlled filling of Ge islands with holes in the structures was accomplished by introducing a boron-δ-doped Si layer at a distance of 5 nm below the QD layer. Since the ionization energy of boron impurities in silicon is only 45 meV, while the energies of the first ten hole levels (measured from the Si valence bond top) in germanium pyramids of this size are 200–400 meV [11], holes at low temperatures leave impurities and occupy the QD levels. The boron concentration in different samples varied from 2×10^{11} to 2.25×10^{12} cm^{-2}, allowing the average number *p* of holes per one Ge QD to be varied from $p = 0.5$ to $p = 6.5$. To prevent the influence of surface effects, ohmic contacts were formed by sputtering Al into preliminarily etched grooves followed by heating at a temperature of 400°C in a nitrogen atmosphere. The etching depth was chosen so that electrical contacts with the concealed Ge layer were formed after heating. To separate effects associated with QDs, test samples without germanium layer were grown in parallel. According to the TEM and STM data, the formed Ge nanoclusters had the average base size of 10 nm in the growth plane, their height was ~1 nm, and their areal density was ~4×10^{11} cm^{-2} (details of the sample preparation can be found in [1]). Current was measured at a voltage of 100 mV, which corresponded to the ohmic region of current–voltage characteristics over the entire temperature range studied. A GaAs light emitting diode with emission maximum at a wavelength of ~0.9 μm was used as a source of interband illumination. All measurements of photoconduction kinetics were performed after the samples had been kept at the measurement temperature for several hours without applying voltage.

EXPERIMENTAL RESULTS

The dependence of conductance (in e^2/h units) on the boron concentration in the δ layer is shown in Fig. 1. One can see that the conductance oscillates upon changing the δ-doping level and, hence, the degree of filling QDs with holes. Since the QD ground state is filled when the number *p* of holes in the dot is two and the excited state is filled if this number is six [12], the minima in conductance should be observed just for these values. Then the first minimum at the boron concentration $N_B \sim 1.2 \times 10^{12}$ cm^{-2} should correspond to two holes in a dot. However, for the real dot density ~4×10^{11} cm^{-2}, this doping should give $p = 3$. This discrepancy may be caused by the errors in determining the doping level in the Si δ layer, because it was calculated indirectly, and in determining the QD density.

After exposure to the interband light, the transient photoconductance of the structures displays an intricate behavior in the course of relaxation to the stationary state upon illumination and after switching off the light. Typical time dependences of photoconductance are shown in Fig. 2a for two samples with different levels of δ doping. Contrary to the test structures without QDs, where the photoconductance is always positive, the photoconductance in the samples with germanium can change sign, depending on the initial number of holes in the dots. For instance, the sample with an integer number of holes in QD has positive photoconductance, whereas the latter becomes negative in the case of fractional level filling with holes. In our opinion, a change in the photoconductance sign upon illumination is a proof of the hopping rather than the band nature of photoconduction. The photoconduction kinetics is anomalously slow both upon switching on and switch-

ing off the light, and the conductance does not regain its equilibrium value and differs by ~10% from it even ~5000 s after switching off the light. Such a behavior is typical of the persistent photoconduction effect observed in Coulomb glasses, magnetic materials, and various semiconductor systems [13–15]. It should be noted that long-time photoconduction kinetics was not observed in the test samples without QDs (Fig. 2b). In Fig. 3, the curves for the time dependence of positive photoconductance correspond to three different light intensities and to the case where the light initially switches on in the thermodynamically equilibrium state of the sample. Inasmuch as the character of the negative photoconductance dynamics, except for a sign, is similar to the dynamics of positive photoconductance, all further experimental data are presented only for the samples with positive photoconductance. One can see that the conductance $G(t)$ rapidly increases immediately after switching on the irradiation, but thereafter the rise is strongly decelerated. It is worth noting that if the light again switches on after relaxation for approximately two hours in the dark, then, for the same initial G values (points A and B in Fig. 2a), the conductance increases much faster than after the initial switching on. The temperature-dependent relaxation of the post-illumination photoconductance G_{PPC} is demonstrated in Fig. 4. All curves are normalized according to $G_{PPC}(t) = (G(t) - G_d)/(G(0) - G_d)$, where $G(0)$ is the photoconductance immediately after switching off the light and G_d is the initial dark conductance. One can see that the persistent photoconduction is noticeably suppressed at elevated temperatures.

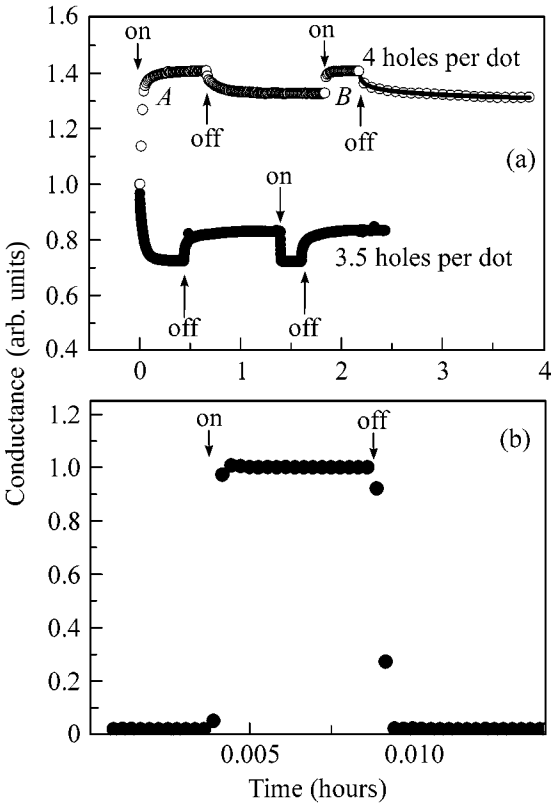

Fig. 2. (a) Photoconduction kinetic curves normalized to the initial dark G values for the samples with different hole concentrations in QDs. The solid line is the approximation of experimental data by the logarithmic function. (b) Photoconductance of the sample without QDs.

DISCUSSION

Illumination by the interband light generates electron–hole pairs in the sample. Electron can easily be captured by the positively charged QDs, whereas hole capture in the repulsive potential is hampered. The recombination of an electron with equilibrium hole in QD reduces the barrier to the capture of nonequilibrium holes. Therefore, hole capture in the course of illumination reduces progressively the potential barrier height. The stationary state is established when the electron and hole flows into dots are equalized. A change in the hole concentration in the dots can be described by the following equation:

$$\frac{dp}{dt} = -J_e - C_{\text{em}} + C_{\text{cap}} \exp\left(\frac{-V}{kT}\right), \qquad (1)$$

where J_e is the electron flow into dots; V is the barrier height; and C_{em} and C_{cap} are the emission and capture rates, respectively. Inasmuch as the equilibrium state with identical capture and emission rates cannot be achieved in the experimental time, the emission term in Eq. (1) can be ignored. At a small concentration Δp of nonequilibrium holes, the barrier height and the con-

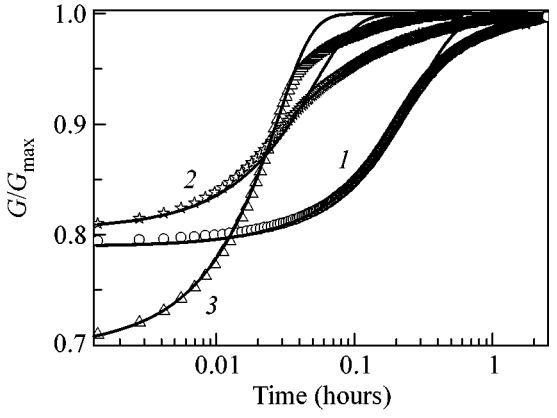

Fig. 3. Plots of photoconduction kinetic curves vs. the intensity of exciting light. Solid lines are the results of fitting experimental data to the numerical solution to Eq. (2). The light intensities for curves *2* and *3* are, respectively, $3I_0$ and $7I_0$, where I_0 is the light intensity for curve *1*.

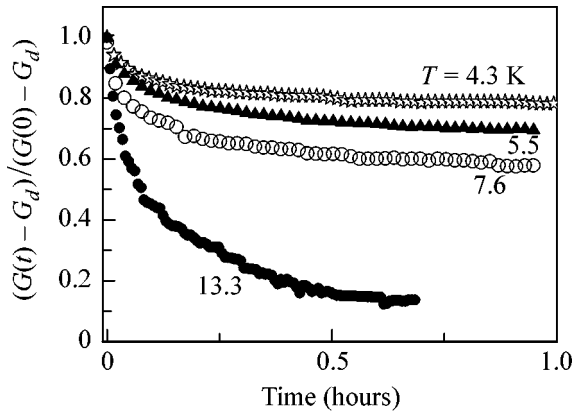

Fig. 4. Photoconduction relaxation curves normalized according to $G_{PPC}(t) = (G(t) - G_d)/(G(0) - G_d)$ at various temperatures.

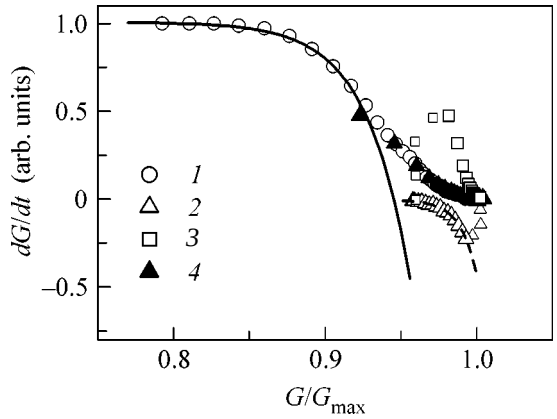

Fig. 5. Derivative of the experimental curve for photoconduction kinetics as a function of photoconductance: (*1*) light switches on for the first time; (*2*) light is switched off; (*3*) light switches on for the second time; (*4*) the same, but the curve is extended toward lower barriers. The solid and dashed lines are for the dependences calculated by Eqs. (2) and (3), respectively.

ductance can be set proportional to Δp. Then the equation for conductance takes the form

$$dG/dt = AI + B\exp(-\gamma C), \qquad (2)$$

where I is the light intensity and A, B, and γ are constants. Since the conductance is the oscillating function of the degree of filling dots with holes, a change in the hole concentration upon illumination can both increase and decrease the conductance. The positive photoconductance should be observed upon a decrease in the number of holes in the dots in the samples with complete filling, whereas the negative photoconductance should be observed for the fractional filling of the quantum level with holes. This situation is observed in our experiment. The solid lines in Fig. 3 are the approximation of experimental data by the numerical solution to Eq. (2). The short-time portions of the curves for the time dependence of photoconductance are rather well described by the calculations, but the further increase in conductance is much slower than is predicted by calculations. Figure 5 shows the derivative of the experimentally measured photoconductance with respect to time as a function of conductance. One can see (solid line) that the exponential character of conductance derivative (Eq. (2)) breaks when the conductance achieves the value $G \approx 0.93G_{max}$. In our opinion, the observed discrepancy between the experimental data and the calculations is caused by the equalization of the potential barrier heights as a result of hole capture by the charged QDs in the course of illumination. Because of the initial scatter in nanocluster sizes and, hence, in the number of holes in them, the barrier heights around the germanium islands are also inhomogeneously spread. The effective barrier height V characterizing hole capture (Eq. (1)) is equal to its minimal value in the inhomogeneous system. Upon illumination, holes are captured by the dots having the smallest positive charge, as a result of which the number of holes is equalized throughout the whole QD array. As a result, the effective barrier becomes higher than in the equilibrium case with the same average degree of filling dots with holes. The rise in the potential barrier height decelerates the increase in conductance with time, which is observed in the experiment. After switching off the light, hole capture by the QDs is continued, so that the barrier height progressively increases. In this case, a change in conductivity obeys the following equation:

$$\frac{dG}{dt} = B\exp(-\gamma G), \qquad (3)$$

which has the analytic solution $G(t) = G_0 - C\ln(t_0 - t)$, where G_0, C, and t_0 are constants. It is seen in Fig. 2a (solid line) that the experimental decrease in conductance is well described by the logarithmic law, while the corresponding dependence of dG/dt on G is well approximated by the exponent (dashed line in Fig. 5). Since the state to which the system relaxes after switching off the light is formed at low temperatures, at which the hole capture by dots is strongly hampered, the conductance in this state differs substantially from its value in the initial equilibrium state. Apart from the difference in the absolute number of holes in dots, the state with PPC is characterized by a more homogeneous hole distribution. For this reason, if the values of conductance at the instants the light switches on for the first and second times are equal (points A and B in Fig. 2a), the effective barrier height in the second case will be lower. If so, the conductance derivatives should coincide for the first and second curves after the second one is extended toward lower barriers. We see that, after this transformation (dark triangles in Fig. 5), the curves indeed coincide with each other. If the model suggested is valid, the hole capture efficiency should increase with temperature and, hence, the PPC effect should be suppressed. We see that, at a temperature of ~13 K, the PPC

differs no more than by 15% from the initial equilibrium value of conductance.

In summary, the long-time nonexponential photoconduction kinetics and the persistent photoconduction effect have been observed in the Ge/Si heterostructures with a two-dimensional QD layer. Two main assumptions underlie the model describing the experimental results: the hole-capture cross section by QDs depends on the degree of QD filling, and the number of holes in the QD ensemble is equalized upon the photoconduction excitation and relaxation. A change in the photoconductance sign with changing the initial number of holes in the QD ensemble was explained by the oscillatory character of hopping conduction.

This work was supported by the Russian Foundation for Basic Research (project no. 01-02-17329), the State program "Surface Atomic Structures" (project no. 40.012.1.1.1153), and the Lavrent'ev Foundation for Youth Projects (grant no. 27).

REFERENCES

1. A. I. Yakimov, A. V. Dvurechenskiĭ, A. I. Nikiforov, and A. A. Bloshkin, Pis'ma Zh. Éksp. Teor. Fiz. **77**, 445 (2003) [JETP Lett. **77**, 376 (2003)].
2. M. Ben-Chorin, Z. Ovadyahu, and M. Pollak, Phys. Rev. B **48**, 15025 (1993).
3. A. Vaknin, Z. Ovadyahu, and M. Pollak, Phys. Rev. Lett. **81**, 669 (1998).
4. M. K. Sheĭnkman and A. Ya. Shik, Fiz. Tekh. Poluprovodn. (Leningrad) **10**, 209 (1976) [Sov. Phys. Semicond. **10**, 128 (1976)].
5. M. Pollak, Philos. Mag. B **50**, 265 (1984).
6. A. Vaknin, Z. Ovadyahu, and M. Pollak, Phys. Status Solidi B **205**, 395 (1998).
7. Z. Ovadyahu and M. Pollak, Phys. Rev. Lett. **79**, 459 (1997).
8. C. C. Yu, Phys. Rev. Lett. **82**, 4074 (1999).
9. T. N. Theis and P. M. Mooney, Mater. Res. Soc. Symp. Proc. **163**, 729 (1990).
10. H. J. Queisser, Phys. Rev. Lett. **54**, 234 (1985).
11. A. V. Dvurechenskii, A. V. Nenashev, and A. I. Yakimov, Nanotechnology **13**, 75 (2002).
12. A. I. Yakimov, A. V. Dvurechenskii, A. I. Nikiforov, and O. P. Pchelyakov, Thin Solid Films **336**, 332 (1998).
13. J. Z. Li, J. Y. Lin, H. X. Jiang, *et al.*, Appl. Phys. Lett. **75**, 1899 (1999).
14. J. C. Fan, J. C. Wang, and Y. F. Chen, Appl. Phys. Lett. **75**, 2978 (1999).
15. Hirotaka Oshima, Masao Nakamura, and Kenjiro Myano, Phys. Rev. B **63**, 075111 (2001).

Translated by V. Sakun

JETP Letters, Vol. 78, No. 9, 2003, pp. 592–596. From Pis'ma v Zhurnal Éksperimental'noĭ i Teoreticheskoĭ Fiziki, Vol. 78, No. 9, 2003, pp. 1082–1086.

Waves in a Superlattice with Anisotropic Inhomogeneities¶

V. A. Ignatchenko[1, *], A. A. Maradudin[2], and A. V. Poszdnyakov[1]

[1] *Kirensky Institute of Physics, Siberian Division, Russian Academy of Sciences, Krasnoyarsk, 660036 Russia*

[2] *Department of Physics and Astronomy, University of California, Irvine, CA 92697, USA*

**e-mail: vignatch@iph.krasn.ru*

Received October 8, 2003

Dependences of the dispersion laws and damping of waves in an initially sinusoidal superlattice on inhomogeneities with anisotropic correlation properties are studied for the first time. The period of the superlattice is modulated by the random function described by the anisotropic correlation function $K_\phi(\mathbf{r})$ that has different correlation radii, $k_\parallel^{-1}$ and $k_\perp^{-1}$, along the axis of the superlattice z and in the plane xy, respectively. The anisotropy of the correlation is characterized by the parameter $\lambda = 1 - k_\perp/k_\parallel$ that can change from $\lambda = 0$ to $\lambda = 1$ when the correlation wave number $k_\perp$ changes from $k_\perp = k_\parallel$ (isotropic 3D inhomogeneities) to $k_\perp = 0$ (1D inhomogeneities). The correlation function of the superlattice $K(\mathbf{r})$ is developed. Its decreasing part goes to the asymptote L that divides the correlation volume into two parts, characterized by finite and infinite correlation radii. The dependences of the width of the gap in the spectrum at the boundary of the Brillouin zone $\Delta\nu$ and the damping of waves ξ on the value of λ are studied. It is shown that decreasing L leads to the decrease of $\Delta\nu$, and increase of ξ, with the increase of λ. © *2003 MAIK "Nauka/Interperiodica".*

PACS numbers: 68.65.Cd; 63.50.+x

1. Theoretical studies of the wave spectrum in disordered superlattices (SLs) have been carried out very intensively in recent years. This is due to the wide use of these materials in various high-tech devices, as well as to the fact that they are convenient models for developing new methods of theoretical physics for studying media without translation symmetry. Several methods exist now for developing a theory of such SLs: the modeling the randomization by altering the order of successive layers of two different materials [1–7]; the numerical modeling the random deviations of the interfaces between layers from their initial periodic arrangement [8–10]; the postulating of the form of the correlation function of an SL with inhomogeneities [11, 12]; the application of the geometrical optics approximation [13]; and the development of the dynamic composite elastic medium theory [14].

One more method for investigating the influence of inhomogeneities on the wave spectrum of an SL was suggested in [15], the method of the random spatial modulation (RSM) of the period of the SL. This method is an extension of the well-known theory of the random frequency (phase) modulation of a radio signal [16, 17] to the case of spatial inhomogeneities in an SL. The advantage of this method is that the form of the correlation function (CF) of the SL is not postulated but is developed from the most general assumptions about the nature of a random spatial modulation of the SL period. The knowledge of the CF corresponding to a particular type and dimensionality of inhomogeneities permitted applying the methods of investigations of averaged Green functions to find the energy spectrum and other characteristics of the waves [15, 18–25]. In all these papers, only isotropic 3D inhomogeneities were considered side by side with 1D inhomogeneities.

In the present paper, effects of 3D inhomogeneities with anisotropic correlation properties on the wave spectrum of SLs are studied for the first time. The continuous transition between isotropic 3D inhomogeneities and 1D inhomogeneities as the anisotropy of the correlations is changed considered.

2. Correlation function. An SL is characterized by the dependence of some material parameter A on the coordinates $\mathbf{x} = \{x, y, z\}$. The physical nature of the parameter $A(\mathbf{x})$ can be different. This parameter can be a density of matter or a force constant for the elastic system of a medium, the magnetization, anisotropy, or exchange for a magnetic system, and so on. We represent $A(\mathbf{x})$ in the form

$$A(\mathbf{x}) = A[1 + \gamma\rho(\mathbf{x})], \quad (1)$$

where A is the average value of the parameter, γ is its relative rms variation, and $\rho(\mathbf{x})$ is a centered ($\langle\rho(\mathbf{x})\rangle = 0$) and normalized ($\langle\rho(\mathbf{x})^2\rangle = 1$) function. The function $\rho(\mathbf{x})$ describes the periodic dependence of the parameter along the SL axis z, as well as the random spatial modulation of this parameter which, in the general case, can be a function of all three coordinates $\mathbf{x} = \{x, y, z\}$.

¶ This article was submitted by the authors in English.

In this paper we will consider an SL that has a sinusoidal dependence of the material parameter on the coordinate z in the initial state when inhomogeneities are absent. According to the RSM method, we represent the function $\rho(\mathbf{x})$ in the form

$$\rho(\mathbf{x}) = \sqrt{2}\cos[q(z-u(\mathbf{x}))+\psi], \quad (2)$$

where $q = 2\pi/l$ is the SL wave number, l is its period, and $u(\mathbf{x})$ is the random spatial modulation. The SL is characterized by the CF $K(\mathbf{r}) = \langle\rho(\mathbf{x})\rho(\mathbf{x}+\mathbf{r})\rangle$, the general form of which was obtained in [15]:

$$K(\mathbf{r}) = \cos qr_z \exp\left[-\frac{1}{2}Q(\mathbf{r})\right]. \quad (3)$$

Here,

$$Q(\mathbf{r}) = \frac{2q^2}{(2\pi)^3}\int\int K_{\varphi}(\mathbf{r}_1)e^{-i\mathbf{k}\mathbf{r}_1} \times (1-\cos\mathbf{k}\mathbf{r})\frac{d\mathbf{k}}{k^2}d\mathbf{r}_1, \quad (4)$$

where $K_{\varphi} = \langle\boldsymbol{\varphi}(\mathbf{x})\boldsymbol{\varphi}(\mathbf{x}+\mathbf{r})\rangle$ is the CF of the function $\boldsymbol{\varphi} = \mathrm{grad}\,u(\mathbf{x})$.

Upon integrating Eq. (4) with respect to $\mathbf{k}$, we obtain $Q(\mathbf{r})$ in the form

$$Q(\mathbf{r}) = \frac{q^2}{4\pi}\int K_{\varphi}(\mathbf{r}_1)\left[\frac{2}{|\mathbf{r}_1|}-\left(\frac{1}{|\mathbf{r}_1-\mathbf{r}|}-\frac{1}{|\mathbf{r}_1+\mathbf{r}|}\right)\right]d\mathbf{r}_1. \quad (5)$$

On the assumption that the correlation properties of the function $u(\mathbf{x})$ are isotropic in the xy plane and anisotropic in the directions between the z axis and the xy plane, we model the CF in the form:

$$K_{\varphi}(\mathbf{r}) = \sigma^2\exp\left\{-\frac{1}{2}[k_{\perp}^2(r_x^2+r_y^2)+k_{\parallel}^2r_z^2]\right\}, \quad (6)$$

where $k_{\perp}$ and $k_{\parallel}$ are the correlation wave numbers in the xy plane and along the z axis, respectively. This function in the 1D ($k_{\perp} = 0$), 2D ($k_{\parallel} = 0$), or isotropic 3D ($k_{\perp} = k_{\parallel}$) limit transforms into the Gaussian function. It was shown in [21] that the coefficient σ in Eq. (6) has the form

$$\sigma = \gamma_u(k_{\parallel}^2+2k_{\perp}^2)^{1/2}/q. \quad (7)$$

Substituting Eq. (6) into Eq. (5), we obtain a complicated expression where only one integration can be performed in the threefold integral. For overcoming this difficulty, we obtain one more representation of the function $Q(\mathbf{r})$. Using the following integral representation [27],

$$\frac{1}{r} = \sqrt{\frac{2}{\pi}}\int_0^{\infty}\exp(-r^2t^2/2)dt, \quad (8)$$

where the integration variable t has the dimensionality of $[\mathbf{r}]^{-1}$, we obtain $Q(\mathbf{r})$ in the form

$$Q(\mathbf{r}) = \frac{q^2}{(2\pi)^{3/2}}\int_{-\infty}^{\infty}d\mathbf{r}_1\int_0^{\infty}dtK_{\varphi}(\mathbf{r}_1) \times (2e^{-t^2r_1^2/2}-e^{-t^2(\mathbf{r}_1-\mathbf{r})^2/2}-e^{-t^2(\mathbf{r}_1+\mathbf{r})^2/2}). \quad (9)$$

The integral with respect to $\mathbf{r}_1$ can be performed exactly in this fourfold integral after substituting K_{φ} in the form of Eq. (6) into it. As a result, we obtain $Q(\mathbf{r})$ in the form of a one-dimensional integral with respect to τ:

$$Q(\mathbf{r}) = 2\gamma_u^2(1+2\kappa^2)\int_0^{\infty}\left(\frac{1}{(\kappa^2+\tau^2)\sqrt{1+\tau^2}} - \frac{\exp\left\{-\frac{(k_{\parallel}r\tau)^2}{2}\left[\frac{\kappa^2\sin^2\theta}{\kappa^2+\tau^2}+\frac{\cos^2\theta}{1+\tau^2}\right]\right\}}{(\kappa^2+\tau^2)\sqrt{1+\tau^2}}\right)d\tau, \quad (10)$$

where $\tau = t/k_{\parallel}$ is a dimensionless variable, and $\cos\theta = r_z/r$, $\kappa = k_{\perp}/k_{\parallel}$.

For the limiting cases of 1D ($\kappa = 0$), 2D ($\kappa \longrightarrow \infty$), and isotropic 3D ($\kappa = 1$) inhomogeneities, this integral can be calculated exactly, and we obtain known formulas [15]. In the general case of an arbitrary value of κ, the approximation of Eq. (10) by a simpler expression must be done for analytical calculations. For the selection of this expression, we calculate $Q(\mathbf{r})$ at $r = 0$ and $r \longrightarrow \infty$. The integral in Eq. (10) is calculated exactly at both of these limits, and we obtain, respectively,

$$Q_0(\mathbf{r}) = \gamma_u^2\frac{1+2\kappa^2}{1-\kappa^2}\{F(\kappa)-\kappa^2 + [2+\kappa^2-3F(\kappa)]\cos^2\theta\}(k_{\parallel}r)^2, \quad (11)$$

$$Q_{\infty} = 2\gamma_u^2\frac{1+2\kappa^2}{\kappa^2}F(\kappa),$$

where

$$F(\kappa) = \frac{\kappa}{\sqrt{1-\kappa^2}}\arctan\frac{\sqrt{1-\kappa^2}}{\kappa}. \quad (12)$$

Using these expressions and extending the idea that has been suggested in [23] for the approximation of the CF of isotropic 3D inhomogeneities, we suggest the

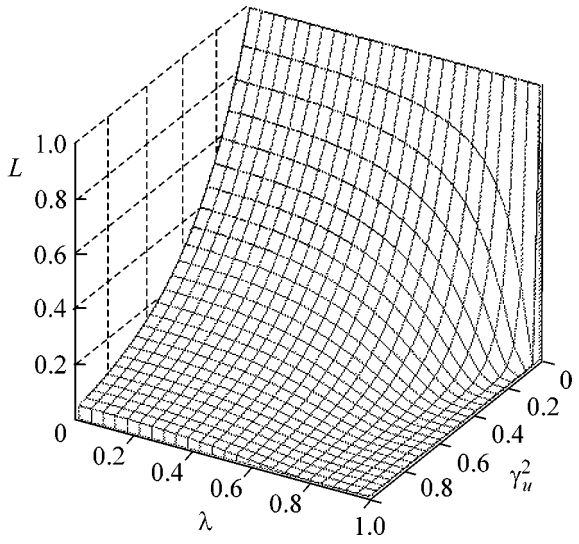

Fig. 1. Dependence of the asymptote L of the CF on the rms fluctuation γ_u and the anisotropy parameter of the correlations λ.

approximation formula for the CF of the anisotropic inhomogeneities in the form

$$K(\mathbf{r}) = \cos qr_z\{L + (1-L)e^{-Pr}\}, \quad (13)$$

where L is the asymptote of the decreasing part of $K(\mathbf{r})$ determined by the equation

$$L = \exp\left(-\frac{1}{2}Q_\infty\right); \quad P = Q_0(r)/k_\parallel r^2. \quad (14)$$

In the present work, we restrict ourselves to the consideration of uniaxial anisotropic inhomogeneities for which the values of κ are between 0 and 1. It is convenient to introduce the parameter of the uniaxial anisotropy $\lambda = 1 - \kappa$, whose values are also between 0 and 1. In this case, $\lambda = 0$ corresponds to the isotropic 3D inhomogeneities and $\lambda = 1$ corresponds to the inhomogeneities with the maximum value of the anisotropy, namely 1D inhomogeneities.

For the isotropic 3D inhomogeneities considered in [23], the value of the asymptote L depended only on the rms fluctuation γ_u. For the anisotropic inhomogeneities, the asymptote L according to Eq. (14) depends on γ_u, as well as on the parameter anisotropy λ (Fig. 1). One can see that L decreases with the increase of γ_u or λ; the value of L goes to zero at the point of the transition of the system from 3D to 1D dimensionality.

3. Dispersion law and damping of waves. We consider the equation for waves in the superlattice in the form

$$\nabla^2\mu + (\nu - \epsilon\rho(\mathbf{x}))\mu = 0, \quad (15)$$

where the expressions for the parameters ϵ and ν and the variable μ are different for waves of different natures. For spin waves, when the parameter of the superlattice $A(\mathbf{x})$ in Eq. (1) is the value of the magnetic anisotropy $\beta(\mathbf{x})$, we have [15] $\nu = (\omega - \omega_0)/\alpha gM$, $\epsilon = \gamma\beta/\alpha$, where ω is the frequency, $\omega_0 = g(H + \beta M)$, g is the gyromagnetic ratio, α is the exchange parameter, H is the magnetic field strength, M is the value of the magnetization, β is the average value of the anisotropy, and γ is its relative rms variation. For elastic waves in the scalar approximation, we have $\nu = (\omega/v)^2$, $\epsilon = \gamma\nu$, where γ is the rms fluctuation of the density of the material and v is the wave velocity. For electromagnetic waves in the same approximation, we have $\nu = \epsilon_e(\omega/c)^2$, $\epsilon = \gamma\nu$, where ϵ_e is the average value of the dielectric permeability, γ is its rms deviation, and c is the speed of light.

Laws of the dispersion and damping of the averaged waves are determined by the equation for the complex frequency $\nu = \nu' + i\xi$, which follows from the vanishing of the denominator of the Green function of Eq. (15). In the Bourret approximation [28], this equation can be represented in the form [21]

$$\nu - k^2 = -\frac{\epsilon^2}{4\pi}\int K(\mathbf{r})\exp[-i(\mathbf{kr} + \sqrt{\nu}r)]\frac{d\mathbf{r}}{r}. \quad (16)$$

Substituting Eq. (13) in Eq. (16), we calculate this integral exactly. As a result, we obtain a complicated equation that we do not give here. When the conditions

$$\gamma_u^2 k_\parallel \ll |\sqrt{\nu}|, \quad \Lambda \ll |\nu| \quad (17)$$

are satisfied, this equation can be reduced to a cubic equation,

$$\nu - k^2 = \frac{\Lambda^2}{4}\left\{\frac{L}{\nu - (k-q)^2} + (1-L)\frac{1 - i\gamma_u^2 k_\parallel f_1\sqrt{\nu}/(k-q)^2}{[\sqrt{\nu} - \gamma_u^2 k_\parallel(f_0 + f_1)]^2 - (k-q)^2}\right\}, \quad (18)$$

where

$$\Lambda = \epsilon/\sqrt{2},$$

$$f_0 = \frac{1+\kappa^2}{2(1-\kappa^2)}[F(\kappa) - \kappa^2], \quad (19)$$

$$f_1 = \frac{1+\kappa^2}{2(1-\kappa^2)}[2 + \kappa^2 - 3F(\kappa)].$$

In the limiting cases $\lambda = 1$ and $\lambda = 0$, Eq. (18) transforms into equations for 1D and isotropic 3D inhomogeneities obtained earlier in [15] and [23], respectively.

Equation (18) has been investigated by numerical methods. The results of these investigations are shown in Fig. 2. Figure 2a shows the behavior of the width of the gap at the Brillouin zone boundary $\Delta\nu = \nu'_+ - \nu'_-$ with the increase of the anisotropy parameter λ for several values of γ_u^2 which are depicted at the correspond-

ing curves. One can see that the maximum values of the width of the gap (which are different for different γ_u^2) correspond to isotropic 3D inhomogeneities ($\lambda = 0$). With the increase of the anisotropy parameter λ, the width of the gap decreases, with this decrease becoming nonmonotonic in the region $\lambda \gtrsim 0.8$. Even some increase of $\Delta\nu$ takes place in this region, which changes again to a decrease when λ goes to unity. For $\gamma_u^2 > 0.25$, the closing of the gap occurs at some critical value of the anisotropy λ_c.

In Fig. 2b, the dependences of the damping $\xi_\pm$ at the Brillouin zone boundary on the parameter of the anisotropy λ are shown for the same values of γ_u^2. The minimum values of the damping correspond to the isotropic 3D inhomogeneities. The damping increases with the increase of the anisotropy and reaches the largest value for 1D inhomogeneities ($\lambda = 1$). For a curve with $\gamma_u^2 = 0.3$ at the critical point $\lambda = \lambda_c$, corresponding to the closing of the gap, the degeneracy of the real parts of the eigenfrequencies takes place ($\nu'_+ = \nu'_-$) and, correspondingly, the removal of the degeneracy of the damping occurs [15]: $\xi_+ \neq \xi_-$ at $\lambda > \lambda_c$.

4. Conclusions. The limiting cases of our general model are the isotropic 3D inhomogeneities ($\lambda = 0$) and 1D inhomogeneities ($\lambda = 1$) that have been investigated in the framework of the RSM method earlier [15, 23]. It was shown in [25] that the main difference between the CFs for isotropic 3D and 1D inhomogeneities was that the decreasing function went to zero when $r \longrightarrow \infty$ in the 1D case while the decreasing function in the isotropic 3D case went to the nonzero asymptote $L = \exp(-3\gamma_u^2)$. Because of this, the 1D inhomogeneities had a finite correlation radius in the entire volume of the superlattice, while for the isotropic 3D case, volumes with a finite correlation radius existed side by side to volumes with an infinite correlation radius. In [25], attention was also given to the important role of the value of the asymptote L in the transition from the disordered SL to an ideal periodic one with the decrease of γ_u. In the 1D case, this transition was carried out by increasing the correlation radius. For the 3D case, another kind of transition took place: the changing of the relationship between the volumes with finite and infinite correlation radii went on in parallel with the increase of the correlation radius.

For the general case of anisotropic inhomogeneities, the asymptote L depends not only on γ_u but also on λ. The changing of λ from 0 to 1 at $\gamma_u = \text{const}$ leads to the changing of L from $L = \exp(-3\gamma_u^2)$ to $L = 0$. Hence, the changing of the anisotropy parameter λ leads to two contributions to the changing of the form of the CF, exerting opposite influences on the characteristics of the wave spectrum. The increase of the correlation radius in the *xy* plane at the unchangeable correlation

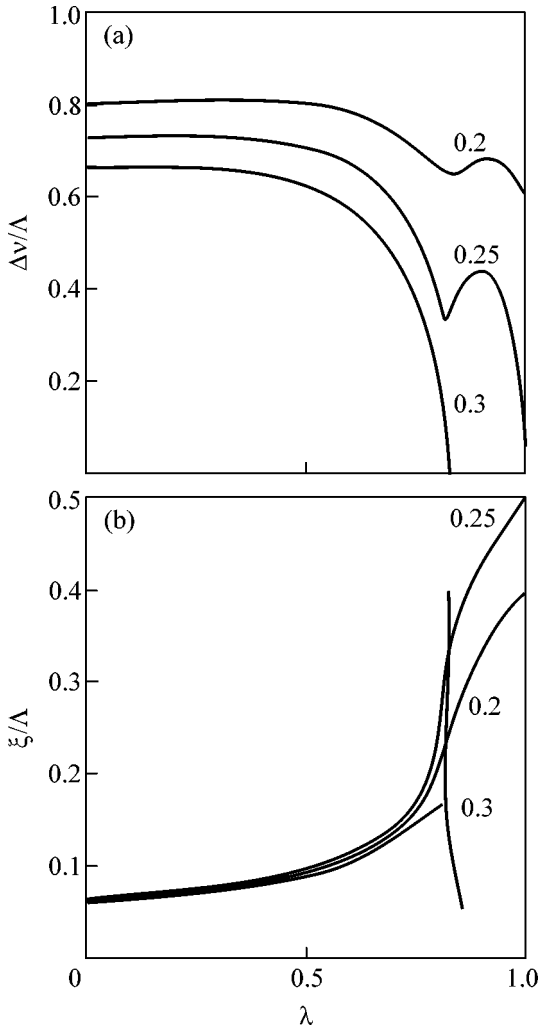

Fig. 2. Dependence of the width of the gap (a) and damping of the waves (b) at the Brillouin zone boundary on the value of the anisotropy of correlations λ for different values of γ_u^2 depicted at the corresponding curves. All graphs correspond to the same normalized correlation number $\eta = k_\parallel q/\Lambda = 4$.

radius along *z* axis means the increase of the mean correlation radius of the system, that is, the decrease of the disorder. This factor in itself could lead to the increase of the width of the gap $\Delta\nu$ at the Brillouin zone boundary and to the decrease of the damping ξ with the increase of λ. However, the increase of λ leads simultaneously to the decrease of L and, consequently, to the decrease of the correlation volume with an infinite correlation radius and to the increase of the volume with finite correlation radii. This factor must lead to the increase of the mean disorder in the system and, consequently, to the decrease of $\Delta\nu$ and increase of ξ. Simultaneous actions of both these factors lead to the dependences of $\Delta\nu$ and ξ on λ depicted in Figs. 2a and 2b. It is seen that the effects of the increase of the disorder prevail, and the decrease of $\Delta\nu$ and increase of ξ occur with the increase of λ. However, the struggle between

the opposite factors leads to the appearance of a nonmonotonic dependence of $\Delta\nu$ on λ: even some increase of $\Delta\nu$ takes place in the region $\lambda > 0.8$ that changes again to a decrease when λ goes to the unit.

This work was supported by the NATO Science Program and Collaborative Linkage grant no. 978090.

REFERENCES

1. J. M. Luck, Phys. Rev. B **39**, 5834 (1989).
2. S. Tamura and F. Nori, Phys. Rev. B **41**, 7941 (1990).
3. N. Nishiguchi, S. Tamura, and F. Nori, Phys. Rev. B **48**, 2515 (1993).
4. G. Pang and F. Pu, Phys. Rev. B **38**, 12649 (1988).
5. J. Yang and G. Pang, J. Magn. Magn. Mater. **87**, 157 (1994).
6. D. H. A. L. Anselmo, M. G. Cottam, and E. L. Albuquerque, J. Appl. Phys. **85**, 5774 (1999).
7. L. I. Deych, D. Zaslavsky, and A. A. Lisyansky, Phys. Rev. E **56**, 4780 (1997).
8. B. A. Van Tiggelen and A. Tip, J. Phys. I **1**, 1145 (1991).
9. A. R. McGurn, K. T. Christensen, F. M. Mueller, and A. A. Maradudin, Phys. Rev. B **47**, 13120 (1993).
10. M. M. Sigalas, C. M. Soukoulis, C.-T. Chan, and D. Turner, Phys. Rev. B **53**, 8340 (1996).
11. V. A. Ignatchenko, R. S. Iskhakov, and Yu. I. Mankov, J. Magn. Magn. Mater. **140–144**, 1947 (1995).
12. A. G. Fokin and T. D. Shermergor, Zh. Éksp. Teor. Fiz. **107**, 111 (1995) [JETP **80**, 58 (1995)].
13. A. V. Belinskiĭ, Usp. Fiz. Nauk **165**, 691 (1995) [Phys. Usp. **38**, 653 (1995)].
14. B. Kaelin and L. R. Johnson, J. Appl. Phys. **84**, 5451 (1998); J. Appl. Phys. **84**, 5458 (1998).
15. V. A. Ignatchenko and Yu. I. Mankov, Phys. Rev. B **56**, 194 (1997).
16. A. N. Malakhov, Zh. Éksp. Teor. Fiz. **30**, 884 (1956) [Sov. Phys. JETP **3**, 701 (1956)].
17. S. M. Rytov, *Introduction to Statistical Radiophysics*, 2nd ed. (Nauka, Moscow, 1976).
18. V. A. Ignatchenko, Yu. I. Mankov, and A. V. Pozdnaykov, Zh. Éksp. Teor. Fiz. **116**, 1335 (1999) [JETP **89**, 717 (1999)].
19. V. A. Ignatchenko, Yu. I. Mankov, and A. A. Maradudin, Phys. Rev. B **59**, 42 (1999).
20. V. A. Ignatchenko, Yu. I. Mankov, and A. A. Maradudin, J. Phys.: Condens. Matter **11**, 2773 (1999).
21. V. A. Ignatchenko, A. A. Maradudin, and A. V. Pozdnaykov, Phys. Met. Metallogr. **91** (Suppl. 1), 69 (2001).
22. V. A. Ignatchenko, Yu. I. Mankov, and A. A. Maradudin, Phys. Rev. B **62**, 2181 (2000).
23. V. A. Ignatchenko, Yu. I. Mankov, and A. A. Maradudin, Phys. Rev. B **65**, 024207 (2002).
24. V. A. Ignatchenko, Yu. I. Mankov, and A. A. Maradudin, Pis'ma Zh. Éksp. Teor. Fiz. **77**, 335 (2003) [JETP Lett. **77**, 285 (2003)].
25. V. A. Ignatchenko, Yu. I. Mankov, and A. A. Maradudin, Phys. Rev. B **68** (2003, in press).
26. A. A. Sveshnikov, *Applied Methods of the Theory of Random Functions*, 2nd ed. (Nauka, Moscow, 1968; Pergamon Press, Oxford, 1966).
27. E. Madelung, *Die Mathematischen Hilfsmittel des Physikers*, 7th ed. (Springer, Berlin, 1964; Nauka, Moscow, 1968).
28. R. C. Bourret, Nuovo Cimento **26**, 1 (1962); Can. J. Phys. **40**, 783 (1962).

JETP Letters, Vol. 78, No. 9, 2003, pp. 597–601. Translated from Pis'ma v Zhurnal Éksperimental'noĭ i Teoreticheskoĭ Fiziki, Vol. 78, No. 9, 2003, pp. 1087–1092.

On Coding of a Quantum Source of States with a Finite Frequency Band: Quantum Analogue of the Kotel'nikov Theorem on Sampling

S. N. Molotkov

Institute of Solid State Physics, Russian Academy of Sciences, Chernogolovka, Moscow region, 142432 Russia
Faculty of Computational Mathematics and Cybernetics, Moscow State University, Vorob'evy gory, Moscow, 119899 Russia
e-mail: molotkov@issp.ac.ru

Received August 27, 2003; in final form, September 30, 2003

An example of coding a source of quantum states with a finite frequency band W and finite exit power not exceeding $\sim(\hbar W)W$ is given. The number of classical information bits that can be coded in the quantum states generated by such a source per unit time is $C = W$. Such a source is minimal in the sense that the filling factor for each of the orthogonal single-particle modes constituting $N = WT$-photon vector in time window $2T$ is equal to 1. This result can be treated as a quantum analogue of the Kotel'nikov theorem on sampling for classical signals [8], when the signal intensity is reduced to the single-photon level. In this case, quantum states at the source exit are fundamentally entangled due to identity of photons. © *2003 MAIK "Nauka/Interperiodica".*

PACS numbers: 03.67.Hk; 89.70.+c; 42.50.-p

The transmission capacity of a communication channel is an important characteristic and determines the upper limiting rate of errorless information transmission in the asymptotic limit of long sequences. For classical communication channels, where information carriers are classical objects (signals), capacities are determined by Shannon coding theorems [1]. In quantum communication channels, carriers are quantum objects, and classical information is coded in the states of quantum systems, which are generally described by density matrix operators. Mathematical investigations of quantum communication channels were pioneered by Holevo as early as in the 1970s [2]. Nowadays, coding in quantum communication channels is a rapidly developing direction of quantum information theory, where fundamental results on transmission capacities were already obtained [2–7]. Transmission capacity per unit time is often the most interesting quantity. If a physical communication channel is perfect, i.e., if the states generated by a source are transmitted without distortion, then capacity is determined by the source entropy. We are interested in the situation where a source of quantum states with finite frequency band W generates quantum states in time and lead them to the entry of a perfect physical communication channel with the same pass band.

We first present intuitive consideration, then briefly describe the classical case, and, finally, turn to the quantum case. The generation of both classical and quantum states proceeds in time. We divide the entire time axis $(-\infty, \infty)$ into individual working windows having size $2T$ and separated by protective time windows with size $\sim T^{1-\delta}$ $(0 < \delta < 1)$. A source with a finite frequency band W generates states in the working time windows $2T$. The source is switched off in the protective time windows. This separation is formally necessary in order to exclude the overlap of states (both classical and quantum) in different working time windows. Since we consider the case where the size $2T$ of the working time window is sufficiently large, the effect of protective time windows vanishes as $T \longrightarrow \infty$ $(T^{1-\delta}/T \longrightarrow 0)$. After that, the problem reduces to the determination of the entropy properties of the source with finite frequency band W in an individual working time window. With this formulation, the problem reduces to a source with discrete time, for which the duration of each package is independent of other state packages in the physical communication channel is equal to $2T$. If the communication channel is perfect, i.e., if all states entering the exit are transmitted without distortion, then the limiting attainable rate of errorless transmission of classical information per unit time (channel capacity) is determined either by the Shannon entropy for the source of classical signals or by the von Neumann entropy for the source of quantum states.[1]

We briefly discuss coding of a source of classical signals with finite frequency band $k \le |W|$. This is necessary for further comparison with the quantum case. A classical signal with a finite frequency band is described by the time function $x(t)$. As was shown by Kotel'nikov [8], the signal $x(t)$ on a finite time interval

[1] More precisely, this rate is given by the Holevo function χ, which transforms in our case to the von Neumann entropy at $T \longrightarrow \infty$.

$(-T, T)$ is determined by $2WT$ degrees of freedom. This means that, in the expansion

$$x(t) = \sum_n x_n \theta_n(t) \quad (1)$$

in a system of orthogonal functions, it suffices to retain $2WT$ terms satisfying the condition

$$\int_{-T}^{T} \theta_n(t)\theta_m(t)dt = \delta_{nm}\lambda_n(WT) \approx 1. \quad (2)$$

In [8], so-called sampling functions ($\theta_n(t) = \sin W[t - n\pi/W]/W[t - n\pi/W]$) were used as basis functions $\theta_n(t)$. A pictorial property of the basis of sampling functions is that the expansion coefficients x_n are equal to the values of signal $x(t)$ at sampling times. Below, it will be more convenient to use other basis functions, whose localization properties in the finite time window $(-T, T)$ are better than those of the sampling functions. In this case, the number of functions most strongly localized in the window $(-T, T)$ remains unchanged. Moreover, these functions also arise in the quantum case, where they serve as single-particle amplitudes (wave functions) for photons that are most strongly localized in the time window $(-T, T)$.

The orthogonality of basis functions with a carrier in the finite frequency band W provides the condition

$$\int_{-T}^{T} \theta_n(t)\theta_m(t)dt$$

$$= \frac{1}{\pi}\int_{k\le|W|}\int_{k'\le|W|} \theta_n(k)\frac{\sin(k-k')T}{k-k'}\theta_m(k')dkdk', \quad (3)$$

$$\theta_n(k) = \frac{1}{2\pi}\int_{-\infty}^{\infty}\theta_n(t)e^{-ikt}dt.$$

The basis functions are orthogonal if they satisfy the integral equation

$$\lambda_n(WT)\theta_n(k) = \frac{1}{\pi}\int_{k\le|W|}\frac{\sin(k-k')T}{k-k'}\theta_n(k')dk'. \quad (4)$$

The eigenvalues depend only on the product WT and form an infinite sequence $1 > \lambda_1(WT) > \lambda_2(WT) > \ldots > 0$. The degree of localization of the squared nth function in the time window $(-T, T)$ is determined by the corresponding eigenvalue

$$\int_{-T}^{T}\theta_n^2(t)dt = \lambda_n(WT). \quad (5)$$

The integral equation determines so-called prolate spheroidal functions [9]. The remarkable property of eigenvalues is that, for large $WT \gg 1$, the are divided into two groups: $\lambda_n(WT) \approx 1$ at $n < 2WT$ and $\lambda_n(WT) \approx 0$ at $n > 2WT$. The size of the transition region of numbers from one behavior to the other is equal to $\approx\ln(4\pi WT)$. More formally, for any $\varepsilon > 0$,

$$\lim_{WT\to\infty}\lambda_{2WT(1-\varepsilon)}(WT) = 1,$$
$$\lim_{WT\to\infty}\lambda_{2WT(1+\varepsilon)}(WT) = 0. \quad (6)$$

This means that, for large WT values, there are no more than $2WT(1-\varepsilon)$ orthogonal (distinguishable) functions whose contribution in the time window $(-T, T)$ tends to unity. If more than $2WT(1+\varepsilon)$ degrees of freedom are used, some of these states will make negligible contribution in this time window $(-T, T)$. For large WT values, the signal $x(t)$ in a finite frequency band and in a finite time interval is described by no more than $2WT$ independent (orthogonal and distinguishable) degrees of freedom and can be specified by $2WT$ independent expansion coefficients x_n.

If a classical source with finite frequency band W generates signals localized in the time window $(-T, T)$ so that the expansion coefficients are specified according to a given probability distribution $p(x_n)$ on the set of these coefficients x_n (signal amplitudes), the source entropy will be determined by the quantity

$$I(WT, p(x_n)) = 2WTH(p(x_n)),$$
$$H(p(x_n)) = -\sum_n p(x_n)\log p(x_n). \quad (7)$$

Further, if these signals are transmitted through a perfect (noiseless) physical communication channel, e.g., with the same pass band W, the entropy of the source given by Eq. (7) will coincide with the mutual information between the entry and exit of such a physical communication channel. Then, the capacity per unit time (source + physical communication channel + receiver) is defined as

$$C = \lim_{T\to\infty}\frac{1}{2T}\max_{\{p(x_n)\}} I(WT, p(x_n))$$
$$= W\max_{\{p(x_n)\}} H(p(x_n)). \quad (8)$$

To compare the classical and quantum cases, the following qualitative considerations are instructive. In classical physics, no formal restrictions occur for changing the expansion coefficients x_n [amplitudes of orthogonal basis functions $\theta_n(t)$] with an arbitrarily small discreteness (continuously). Since the intensity x_n^2 of classical signal, e.g., of an electromagnetic field, in each separate mode $\theta_n(t)$ is equal, to a factor of $\approx\hbar W$, to the photon number in this mode, the signal intensity can change with a finite discreteness. To code information in x_n values, at least two values are necessary ($x_n^2 \propto N_{\max}$, where $N_{\max}$ is the maximum number of

possible x_n^2 values). The total number of different values for all modes is $(\sqrt{N_{\max}})^{2WT}$. If each value is taken with the same probability, source entropy (7) is equal to

$$I(WT, p(x_n)) = 2WT\log(\sqrt{N_{\max}}). \quad (9)$$

Capacity (8) per unit time for the minimum signal level ($N_{\max} = 2$) is

$$C = W. \quad (10)$$

Strictly speaking, formulas for the classical case cannot be used if the mode filling factor is low.

Next we are interested in the capacity in a single-photon regime. These considerations will be used for the qualitative comparison between the classical and quantum cases. Our problem reduces, in fact, to counting the number of possible orthogonal multiphoton states that are generated by a source with a finite frequency band W and localized in the time window $(-T, T)$. We first consider single-photon states at the source exit, which then propagate in one direction ($k > 0$) with a carrier in a finite frequency band W ($k \in [0, W]$). For closer analogue with the classical case, we will consider coding in various shapes of state amplitudes and ignore polarization degrees of freedom. For brevity, we take $c = \hbar = 1$. Thus,

$$|\varphi^e\rangle = \int_0^W \frac{dk}{k}\varphi(k, k_0 = |k|)a^+(k)|0\rangle = \int_{-\infty}^{\infty} d\tau\varphi(\tau)|\tau\rangle, \quad (11)$$

where $\varphi(k, k)$ ($k > 0$) and $\varphi(\tau)$ are the amplitudes of a single-photon package in the momentum and spacetime representations, respectively,

$$\varphi(\tau) = \frac{1}{2\pi}\int_0^W \frac{dk}{\sqrt{k}} e^{-ik\tau}\varphi(k, k),$$
$$|\tau\rangle = \int_0^W \frac{dk}{\sqrt{k}} e^{ik\tau}|k\rangle, \quad |k\rangle = a^+(k)|0\rangle. \quad (12)$$

For a massless field, $\tau = x - t$ depends only on the difference between the coordinate and time. Therefore, if an outcome is obtained near the point x at time t, the same outcome will be obtained at the point x' at time $t' = t + (x' - x)$. For brevity, we will refer to a time window, implying that $(-T, T)$ means $(-(x - t), (x - t))$.

It is necessary to choose the amplitude (wavefunction) of a single-photon package with a carrier in a finite frequency band in such a way that it provides maximum normalization in the spacetime region ($(-T, T)$ window). The degree of localization is formally described by a measurement in this window. Any measurement on the single-photon package in the time window is described by the following decomposition of unity in the single-particle space:

$$I^{(1)} = \int_0^W \frac{dk}{k}|k\rangle\langle k| = I^{(1)}(T) + I^{(1)}(\bar{T})$$
$$= \int_{-T}^{T} \frac{d\tau}{2\pi}|\tau\rangle\langle\tau| + \int_{-(\infty, \infty)/(-T, T)} \frac{d\tau}{2\pi}|\tau\rangle\langle\tau|. \quad (13)$$

Taking Eqs. (12) and (13) into account, we represent the operator associated with the time window $(-T, T)$ in the form

$$I^{(1)}(T) = \sum_{n=1}^{\infty} \lambda_n(WT)|\theta_n\rangle\langle\theta_n|,$$
$$|\theta_n\rangle = \int_0^W \frac{dk}{k}\theta_n(k)|k\rangle. \quad (14)$$

The functions $\theta_n(k)$ are eigenfunctions of integral equation (4), the only difference being that integration is performed over the segment $[0, W]$. The number of functions localized in the time window $(-T, T)$ is equal to WT. The vectors $|\theta_n\rangle$ are, in essence, eigenvectors of the operator $I^{(1)}(T)$, so that it is diagonal in the basis of these vectors. If the outcomes are available only in the time window, any measurement on the initial state is equivalent to measurements on the following effective density matrix

$$\rho(T) = \sum_{n, n'} \lambda_n(WT)\lambda_{n'}(WT)|\theta_n\rangle\langle\theta_n|\varphi\rangle\langle\varphi|\theta_{n'}\rangle$$
$$\times\langle\theta_{n'}| + \mathrm{Tr}\{I^{(1)}(\bar{T})|\varphi\langle\varphi|\}\rangle|?\rangle\langle?|. \quad (15)$$

Here, the formal state $|?\rangle$ is orthogonal to all states and describes outcomes outside the time window. Such outcomes correspond to the case where a measuring instrument is not triggered inside the window. The effective density matrix has unit trace with allowance for the outcomes that must be assigned inconclusive results. For large WT, we can take one of the WT orthogonal (distinguishable) single-photon states that is localized in the window $(-T, T)$ with a probability as close to unity ($\lambda_n(WT) \approx 1$) as is wished and has the effective density matrix

$$\rho_n(T) = \lambda_n(WT)|\theta_n\rangle\langle\theta_n| + (1 - \lambda_n(WT))|?\rangle\langle?|, \quad 1 \le n \le WT \quad (16)$$

in this window.

Let the source generate $N = WT$-photon states

$$|\theta_{n_1}; \ldots \theta_{n_N}\rangle = \int_0^W \ldots \int_0^W \frac{k_1}{k_1} \ldots \frac{dk_N}{k_N} \theta_{n_1}(k_1) \ldots \theta_{n_N}(k_N) |k_1, \ldots, k_N\rangle, \quad (17)$$

$$|k_1, \ldots, k_N\rangle = a^+(k_1) \ldots a^+(k_N)|0\rangle$$

in the working time window. The generalized basis vectors

$$|k_1, \ldots, k_N\rangle = \sqrt{\frac{k_1, k_2 \ldots k_N}{N!}} \sum_{\{j\}} \delta(k_1 - q_{j_1}) \ldots \delta(k_N - q_{j_N}) \quad (18)$$

are totally symmetric about particle permutations, where the symbol $\{j\}$ means summation over all permutations. We now construct $N = WT$-photon density matrices. The filling factor for each single-particle mode is equal to 1. The vectors in Eqs. (17) with various subscripts are eigenvectors of the operator $I^{(N)}(T)$ in the $N = WT$-photon subspace, similarly to the single-photon case. We have

$$I^{(N)} = \int_0^W \ldots \int_0^W \frac{dk_1}{k_1} \ldots \frac{dk_N}{k_N} |k_1, \ldots, k_N\rangle\langle k_1, \ldots, k_N| \quad (19)$$

$$= I^{(N)}(T) + I^{(N)}(\bar{T}),$$

$$I^{(N)}(T) = \int_{-T}^T \ldots \int_{-T}^T \frac{d\tau_1}{2\pi} \ldots \frac{d\tau_N}{2\pi} |\tau_1; \ldots \tau_N\rangle\langle\tau_1; \ldots \tau_N|$$

$$= \sum_{n_1, \ldots, n_N = 1}^{\infty} \lambda_{n_1}(WT) \quad (20)$$

$$\times \lambda_{n_N}(WT) |\theta_{n_1}; \ldots \theta_{n_N}\rangle\langle\theta_{n_1}; \ldots \theta_{n_N}|.$$

Let us tally up the number of orthogonal $N = WT$-photon states.[2] If $N = WT$ photons were distinguishable, the number of orthogonal $N = WT$ photon vectors localized in the window $(-T, T)$ with a near-unity probability would be equal to N^N (without regard for the polarization degrees of freedom). Owing to the identity of bosons (photons), the number of such vectors, which is denoted as $2^{M(WT)}$ for convenience, is equal to the number of ways of distributing $N = WT$ identical particles over $N = WT$ states; we have [10]

$$2^{M(WT)} = \frac{(N + N - 1)!}{(N-1)!N!}, \quad N = WT. \quad (21)$$

[2] I am grateful to the referee who pointed to the error at this point here in the original version of the paper.

Taking the Stirling formula ($N! \approx (N/e)^N \sqrt{2\pi N}$) into account, we obtain for large N values

$$\log 2^{M(WT)} = 2N \log 2 = 2WT. \quad (22)$$

Let the source in each working time window generate one of the $2^{M(WT)}$ orthogonal $N = WT$-photon states with the same probability. If the source works for a sufficiently long time, the statistical ensemble, in which classical information can be coded, is described by the density matrix

$$\rho(M(WT)) = \frac{1}{2^{M(WT)}} \sum_{n_1, \ldots, n_N} |\theta_{n_1}; \ldots \theta_{n_N}\rangle\langle\theta_{n_1}; \ldots \theta_{n_N}|. \quad (23)$$

The von Neumann entropy of the ensemble is maximal for the equiprobable choice of vectors. The information in the finite time window $(-T, T)$ is extracted from the effective density matrix

$$\rho(T) = \frac{1}{2^{M(WT)}} \sum_{n_1, \ldots, n_N} \lambda_{n_1}(WT) \ldots \lambda_{n_N}(WT)$$

$$\times |\theta_{n_1}; \ldots \theta_{n_N}\rangle\langle\theta_{n_1}; \ldots \theta_{n_N}| \quad (24)$$

$$+ \frac{1}{2^{M(WT)}} \sum_{n_1, \ldots, n_N} (1 - \lambda_{n_1}(WT) \ldots \lambda_{n_N}(WT)) |?\rangle\langle?|.$$

For large WT values, one cannot construct statistical ensemble consisting of more than $2^{M(WT)}$ orthogonal $N = WT$-photon states. Classical information coded in the ensemble $\rho(M(WT))$ and extracted from density matrix $\rho(T)$ (24) is given by the quantity $\chi(\rho(T))$ that follows from the Holevo inequality [2]. Since the states $|\theta_{n_1}; \ldots \theta_{n_N}\rangle$ and $|?\rangle$ are pure, $\chi(\rho(T))$ coincides with von Neumann entropy for $\rho(T)$; one has

$$\chi(\rho(T)) = -\mathrm{Tr}\{\rho(T)\log\rho(T)\}$$

$$= -\sum_{n_1, \ldots, n_N} \frac{\lambda_{n_1}(WT) \ldots \lambda_{n_N}(WT)}{2^{M(WT)}}$$

$$\times \log\left(\frac{\lambda_{n_1}(WT) \ldots \lambda_{n_N}(WT)}{2^{M(WT)}}\right) \quad (25)$$

$$- \sum_{n_1, \ldots, n_N} \left(\frac{1 - \lambda_{n_1}(WT) \ldots \lambda_{n_N}(WT)}{2^{M(WT)}}\right)$$

$$\times \log\left(\frac{1 - \lambda_{n_1}(WT) \ldots \lambda_{n_N}(WT)}{2^{M(WT)}}\right).$$

The capacity per unit time is determined by a limit that is analogous to Eq. (8) for the classical case. Taking

into account that the second sum in Eq. (25) tends to zero, we obtain

$$C = \lim_{T\to\infty} C_T,$$
$$C_T = \frac{\log(2^{M(WT)})}{2T} = \frac{M(WT)}{2T} = W. \quad (26)$$

The source generates $N = WT$-photon states in the time window so that the number of photons at the source exit per unit time is $\sim W$ and the energy per one photon is $\sim\hbar W$. Therefore, the number of photons (rather than their mean number, because the states $|\theta_{n_1}; \ldots \theta_{n_N}\rangle$ in Eq. (23) are eigenvectors of the photon-number operator corresponding to the particle-number eigenvalues $N = WT$) in the time window $(-T, T)$ is equal to WT.[3] The power at the source exit is constant and equal to $\sim(\hbar W)W$. The condition for the minimum quantum source means that the number of orthogonal single-particle amplitudes $\theta_n(t)$ constituting $N = WT$-photon amplitude symmetric about particle permutations is equal to WT. The number of photons is also equal to WT; i.e., the filling factor per one single-particle amplitude is equal to 1. If the signal level is brought to the single-photon level, classical capacity (10) symbolically coincides with quantum capacity (26). However, a weak signal cannot be described classically. Coding methods in the classical and quantum cases are also different. In the classical case, information is coded in amplitudes (roughly speaking, in the number of photons) of orthogonal modes. As to the quantum case, information is coded in various orthogonal multiphoton states. Due to the identity of photons, these states are necessarily entangled within each time window $2T$. Such coding of the quantum source can be treated as a quantum analogue of the Kotel'nikov theorem on sampling, if the filling factors of single-particle modes are brought to the single-photon level.

I am grateful to A.S. Holevo, Yu.I. Ozhigov, and S.V. Iordanskiĭ for stimulating discussions and critical remarks that have helped me improve the work. This work was supported by the Russian Foundation for Basic Research (project no. 02-02-16289) and project nos. 40.020.1.1.1170 and 37.029.1.1.0031.

[3] Strictly speaking, WT should be throughout treated as the integer part $[WT]$.

REFERENCES

1. C. E. Shannon, Bell Syst. Tech. J. **27**, 397 (1948); Bell Syst. Tech. J. **27**, 623 (1948).
2. A. S. Kholevo, Probl. Peredachi Inf. **8**, 63 (1972); Probl. Peredachi Inf. **15**, 3 (1979); Usp. Mat. Nauk **53**, 193 (1998).
3. A. S. Kholevo, *Introduction to the Quantum Information Theory* (MTsNMO, Moscow, 2002), Sovrem. Mat. Fiz., No. 5.
4. R. Jozsa and B. Schumacher, J. Mod. Opt. **41**, 2343 (1994).
5. P. Hausladen, R. Jozsa, B. Schumacher, *et al.*, Phys. Rev. A **54**, 1869 (1996).
6. B. Schumacher and M. D. Westmoreland, Phys. Rev. A **56**, 131 (1997).
7. C. H. Bennett, P. W. Shor, J. A. Smolin, and A. V. Thapliyal, Phys. Rev. Lett. **83**, 3081 (1999); quant-ph/9904023.
8. V. A. Kotel'nikov, *Permeability of Ester and Wire in Electric Communication* (Vsesoyuz. Énerg. Komissiya, Moscow, 1933).
9. D. Slepian, J. Math. Phys. **44**, 99 (1965).
10. L. D. Landau and E. M. Lifshitz, *Course of Theoretical Physics*, Vol. 5: *Statistical Physics*, 4th ed. (Nauka, Moscow, 1995; Pergamon Press, Oxford, 1980), Part 1.

Translated by R. Tyapaev

JETP Letters, Vol. 78, No. 9, 2003, pp. 602–605. From Pis'ma v Zhurnal Éksperimental'noĭ i Teoreticheskoĭ Fiziki, Vol. 78, No. 9, 2003, pp. 1093–1096.

Influences of Diffusive Reflection Intensity and Pulse Shaping of Ultrashort Lasers on Turbid Media¶

L. Wang[1, *] and M. Zhao[2]

[1] *Department of Applied Physics, Beijing University of Technology, 100022 Beijing, China*

**e-mail: Lwang.1@bjut.edu.cn*

[2] *Physics Department, Hebei Normal University, 050016 Shijiazhuang, China*

Received September 1, 2003

The influences of the absorption μ_a, the scattering μ_s, and the anisotropy coefficient g on the optical properties of ultrashort pulse in turbid media has been simulated based on the diffusive approximation theory. The laser pulse intensity will be attenuated and the diffusive scattering pulse shape will be widened in the turbid media. Various medium parameters have different influences on the reflection of the laser pulse. The intensity loss of the diffusive reflection light is obtained when μ_a and μ_s are increased in turbid media. The pulse width of the diffusive reflection pulse is rapidly increased far away from the incident point and at the same time the pulse times that are delayed have been numerical simulated in the boundary conditions of semi-infinite homogenous media. © *2003 MAIK "Nauka/Interperiodica".*

PACS numbers: 78.35.+c; 42.25.Fx

1. INTRODUCTION

In a turbid medium, the picosecond (ps) laser is scattered and absorbed due to the nonhomogenous and absorption characteristics of the medium. The diffusive scattering mainly exists when the red and infrared radiation are incident to the turbid material [1]. The statistics reaction of the interaction between the ps laser and absorption medium are the parameters of a scattering intensity and pulsewidth by the properties of a tissue optics and scattering of the pulse laser in diffusive reflectance and transmittance [2]. The widely increasing application of ultrashort pulse lasers in diagnostic and therapeutic medicine has determined the need to obtain noninvasive optical parameters of turbid media by interaction of the medium and radiation light [3, 4]. These properties have been devoted to the measurement of the optical properties of turbid tissue specimens, and the detection of diffusion-reflected and transmitted light have been studied by the authors [5]. Recently, the relationship has been researched between the absorption and scattering coefficient of tissue and the spatial dependence of diffusive reflecting near a finite light resource [6, 7]. Theoretical studies of light pulse propagation in multiple scattering media based on the diffusion approximation theory have been researched by Shimmer [8] and Furutsu [9]. The time resolved reflectance of a plane wave has been measured by Shimizu *et al.* [10] from the suspension of microspheres, leading to the suggestion that this technique might be used to determine the optical properties of the tissue. The studies of time resolved reflectance and transmittance for the noninvasive measurement of tissue optical properties have produced by Patterson *et al.* [4]. The in vivo technique is for a small source. In this paper, the laser pulse energy will be attenuated in the turbid media and the pulse shape will be changed by scattering and absorption. In addition, the diffusive scattering widens the ultrashort pulse. The various medium parameters have different influence on the reflection of the laser pulse. Based on the diffusion approximation theory, the boundary condition of semi-infinite homogeneous media by small narrow linewidth laser beams, the influence of the absorption μ_a, the scattering μ_s, and the anisotropy coefficient g on the ultrashort pulse in the condition have been obtained.

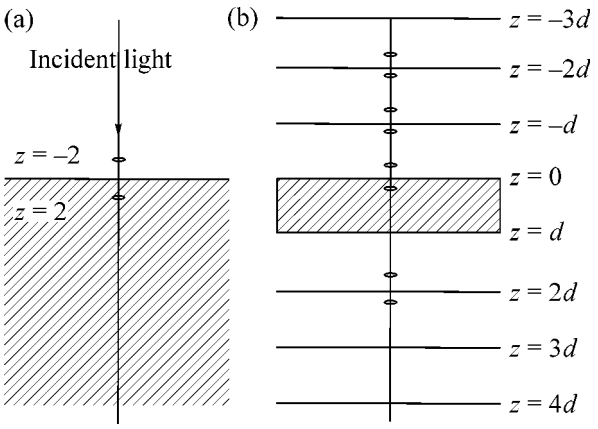

Fig. 1. Diagram of ultrashort pulse incident on semi-infinite and infinite homogeneous tissue (a) and (b).

¶ This article was submitted by the authors in English.

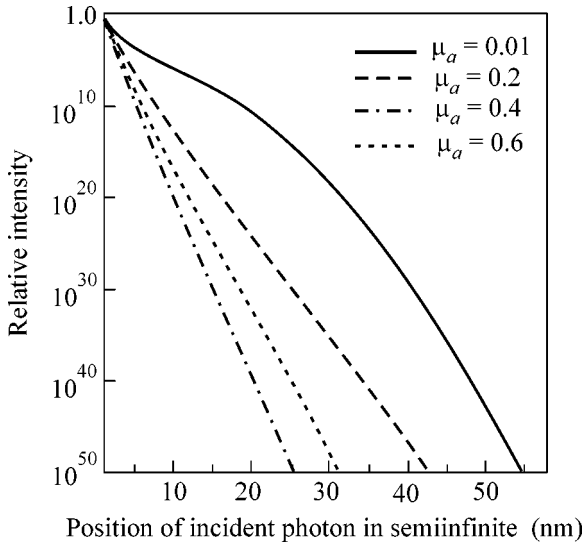

Fig. 2. Intensity of backscattered light versus position of incident photon medium.

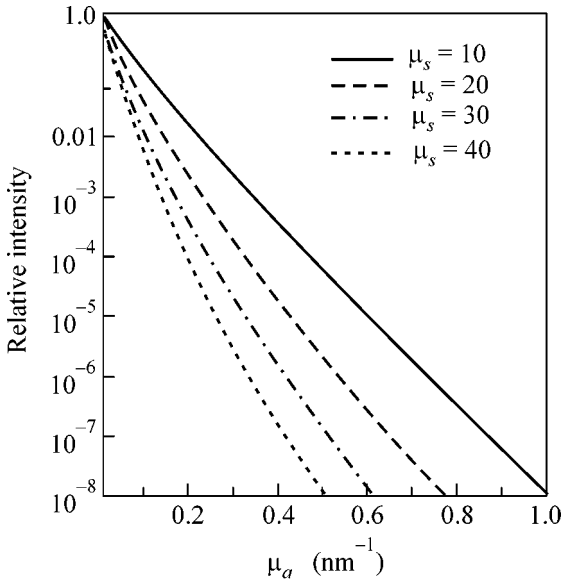

Fig. 3. Curves of diffusion reflection intensity.

2. THEORETICAL ANALYSIS AND NUMERICAL SIMULATION

The biological tissue is made of cells of different size and composition that is called turbid media [3]. The spectral ranges from about 600 to 1300 nm are particularly interesting wavelengths, since at these wavelengths the absorption of light by most soft tissues is at a minimum [11]. Relatively low absorption occurs in this so-called "therapeutic window." The optical properties information of the turbid medium is shown in the diffusive reflection and transmittance light. The geometry of narrow linewidth ultrashort pulse beams is normally incident on the surface of a semi-infinite homogeneous tissue slab, as is shown in Fig. 1a. We simulated a practical Monte Carlo method in which a ps was produced on turbid tissue surface of semi-infinite medium by a small narrow linewidth pulse beams. The diffusion equation of the diffusive photon fluency intensity $\phi(\mathbf{r}, t)$ can be written [4]

$$\frac{1}{\nu}\frac{\partial}{\partial t}\phi(r,t) - D\nabla^2\phi(r,t) + \mu_\alpha\phi(r,t) = \delta(0,0), \quad (1)$$

where $D = [3(\mu_a + (1-g)\mu_s]^{-1}$ is the diffusion coefficient, μ_a is the linear absorption coefficient, μ_s is the linear scattering coefficient, g is the mean cosine of scattering angle, v is the speed of the light in the tissue, and $\delta(0, 0)$ is an isotropic point photon source. It can be shown that in a semi-infinite turbid medium the solution of Eq. (1) is

$$\Phi(\mathbf{r}, t) = \nu(4\pi D\nu t)^{-3/2}\exp\left(-\frac{r^2}{4D\nu t} - \mu_a\nu t\right). \quad (2)$$

All the incident photons are initially scatted at a depth $z_0 = [(1-g)\mu_s]^{-1}$ so that the actual source becomes the simple delta function described above. Patterson [4] *et al.* have shown that a useful assumption is that $\phi(\mathbf{r}, t) = 0$ on the physical boundary $z = 0$. The fluency rate per incident photon can then be written in cylindrical coordinates as the sum of contributions as follow

$$\Phi(\rho, z, t) = \nu(4\pi D\nu t)^{-3/2}\exp(-\mu_a\nu t) \times\left\{\exp\left[-\frac{(z-z_0)^2+\rho^2}{4D\nu t}\right] - \exp\left[-\frac{(z+z_0)^2+\rho^2}{4D\nu t}\right]\right\}. \quad (3)$$

The number of photons reaching the surface per unit area per unit time is $|J(\rho, 0, t)|^2$, which can be calculated from Fick's law [12]: $J(\rho, 0, t) = -D\nabla\Phi(\rho, z, t)|_{z=0}$, which leads to a final expression for the reflectance (ρ, t) that is ultrashort pulse incident to the semi-infinite homogeneous tissue medium

$$R(\rho, t) = |J(\rho, 0, t)| = (4\pi D\nu)^{-3/2} z_0 t^{-5/2}\exp(-\mu_a\nu t)\exp\left(-\frac{\rho^2 - z_0^2}{4D\nu t}\right). \quad (4)$$

Where $\rho^2 \gg z_0^2$, it is noted that the observation

$$\lim\frac{d}{dt}\log_e R(\rho, t) = -\mu_a\nu \quad (5)$$

is known. From Eq. (5), the absorption coefficient of the tissue can be determined from the asymptotic slope of the curve of the $\log_e R(\rho, t)$ versus time t. The speed of light depends on the index of refraction $n = 1.4$ of the tissue which is known to a few percent, $v = 0.214$ mm/per second [13].

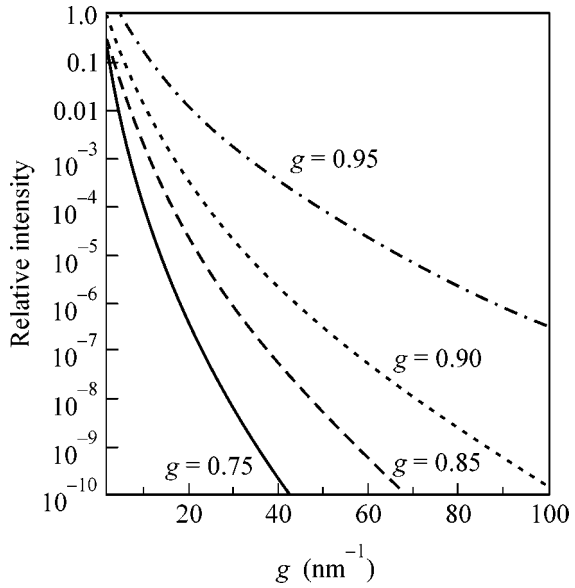

Fig. 4. Curves of backscattered light intensity versus μ_s.

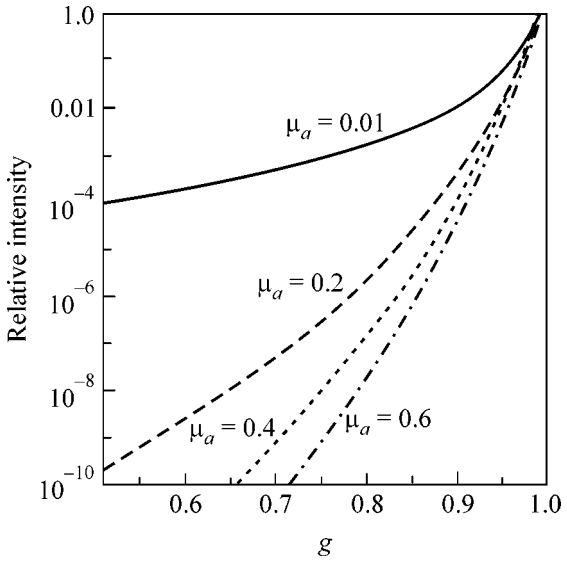

Fig. 5. Curves of intensity and scattering g.

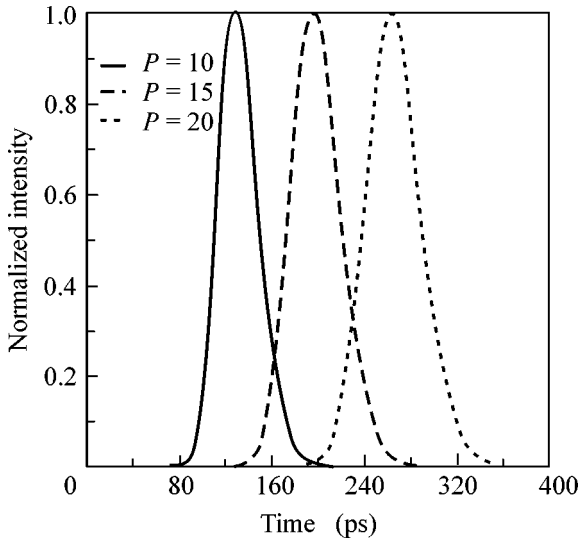

Fig. 6. Curves of pulse shaping with incident position into medium.

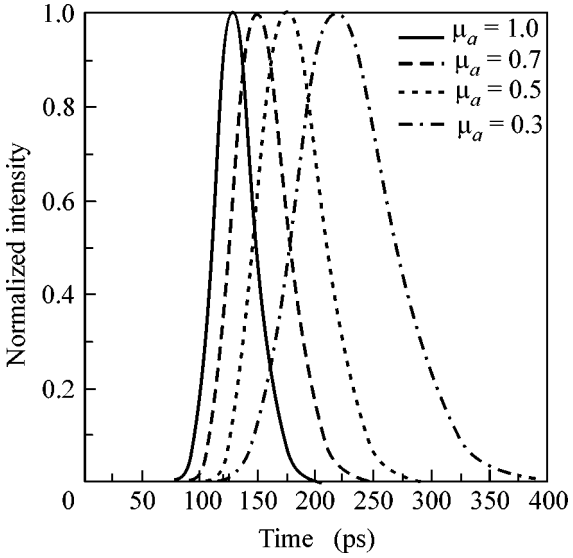

Fig. 7. Diffusion scattering pulse shaping and intensity versus μ_a.

The propagation-scattering coefficient μ_s can also be calculated using the $\log_e R(\rho, t)$ versus t if the slope is zero and the $t_{\max}$. After solving Eq. (4), we can write the expression

$$(1-g)\mu_s = \frac{1}{3\rho^2}(4\mu_a \nu^2 t_{\max}^2 + 10\nu t_{\max}) - \mu_a. \quad (6)$$

The optical properties of a semi-infinite slab of tissue from Eq. (5) and Eq. (6) could in principle be obtained by simulated the diffusive reflected light some distance from the source as a function of time. The total diffusive reflection rate $R(\rho, t)$ can be obtained from the spatial integral of $R(\rho, t)$

$$R(t) = \int_0^\infty R 2\pi\rho(\rho, t)d\rho = (4\pi D\nu)^{-1/2} z_0 t^{-3/2} \exp(-\mu_a \nu t) \exp\left(-\frac{z_0^2}{4D\nu t}\right). \quad (7)$$

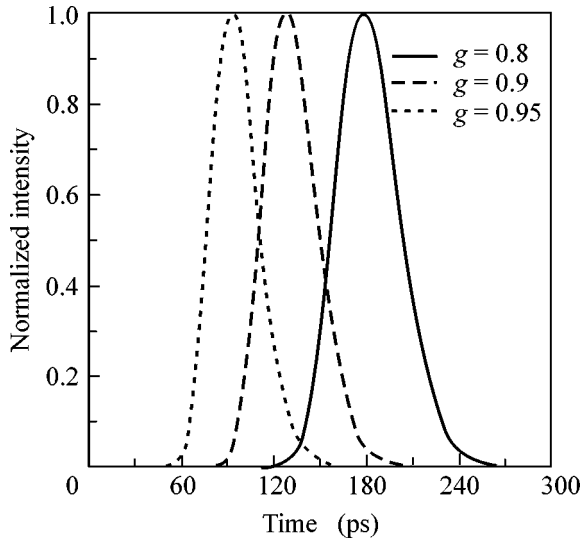

Fig. 8. Curves of pulse shaping versus μ_s.

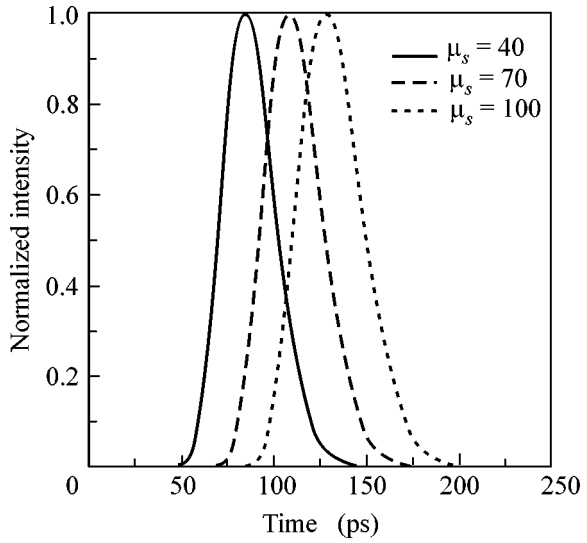

Fig. 9. Curves of pulse shaping versus g.

This expression agrees with the results of Patterson *et al.* [4], such that for a nonabsorption medium the total diffusive reflectance depends on $t^{-3/2}$.

An important question is how simulations of the diffusive reflection are affected by μ_a, μ_s and g in a semi-infinite tissue material. According to the theoretical analysis and computer simulation from Eq. (4), we have obtained the theoretical curves of the backscattering intensity of diffusive reflectance light caused at the different transport simulation P, μ_a, μ_s and g, as shown in Fig. 2, Fig. 3, Fig. 4, and Fig. 5. The effect of the absorption coefficient versus the intensity loss of the diffusive reflection light, which is decreased when the μ_a, μ_s, can clearly be seen from Fig. 2 and Fig. 3. The backscattered intensity is increased when g is increased and μ_a is small, as is shown in Fig. 4 and Fig. 5. From Fig. 2 to Fig. 5, it is shown that the intensity of diffusive reflection is very useful to obtain the physical parameters of the optical properties in the internal turbid medium. The pulse width of the diffusive reflection pulse is affected by the optical parameters of the turbid medium, such that it rapidly increases from the diffusion reflection pulse laser far away from the incident point and, at the same time, the pulse time is delayed as shown in Fig. 6. The pulse width of the reflected light is narrowed in Fig. 7. The time delay of the diffusive reflection light caused by μ_s is increased as shown in Fig. 8. The pulse width of the diffusion reflection light rapidly narrows and the time delay of the reflection pulse at g increases as is shown in Fig. 9. From Fig. 2 to Fig. 9, it is shown that the interaction of the ultrashort pulse and the turbid tissue is very useful when researching the optical parameters of the turbid medium.

3. CONCLUSIONS

The purpose of this work was to research the relations of the diffusive reflection rate $R(\rho, t)$ and optical properties in turbid media. The results of the principle simulation were made coherent with experiments [14] by computer numerical analysis. It was calculated that the parameters μ_a, μ_s, and g in the tissues use an indirect and lossless method according to the foundation theory. This is useful for the development of laser biology and medicine measurement.

REFERENCES

1. V. G. Peters, D. R. Wyman, M. S. Patters, *et al.*, Phys. Med. Biol. **35**, 1317 (1990).
2. A. Ishimaru, Appl. Opt. **28**, 2210 (1989).
3. B. C. Wilson and S. L. Jacques, IEEE J. Quantum Electron. **26**, 2186 (1990).
4. M. S. Patterson, B. Chance, and B. C. Wilson, Appl. Opt. **28**, 2331 (1989).
5. Y. Kuga, A. Ishimaru, and A. P. Bruckner, J. Opt. Soc. Am. **73**, 1812 (1983).
6. R. Hemenger, Appl. Opt. **16**, 2007 (1977).
7. S. L. Jacques, Appl. Opt. **28**, 2223 (1989).
8. A. Ishimaru, J. Opt. Soc. Am. **68**, 1045 (1978).
9. K. Furutsu, J. Opt. Soc. Am. **70**, 360 (1980).
10. K. Shimizu, A. Ishimaru, L. Reynolds, *et al.*, Appl. Opt. **18**, 3484 (1979).
11. J. L. Bulnois, Lasers Med. Sci. **1**, 47 (1986).
12. J. J. Duderstadt and L. J. Hamiton, *Nuclear Reactor Analysis* (Wiley, New York, 1976), p. 140.
13. D. T. Delpy, M. Cope, P. Vanderzee, *et al.*, Phys. Med. Biol. **33**, 1433 (1988).
14. X. L. Wang, B. H. Li, and S. S. Xie, J. Optoelectron. Laser **12**, 418 (2001) (in Chinese).